

Novel materials and algorithms for quantum technologies

Présentée le 9 septembre 2022

Faculté des sciences et techniques de l'ingénieur
Laboratoire de théorie et simulation des matériaux
Programme doctoral en science et génie des matériaux

pour l'obtention du grade de Docteur ès Sciences

par

Francesco LIBBI

Acceptée sur proposition du jury

Dr A. Hessler-Wyser, présidente du jury
Prof. N. Marzari, directeur de thèse
Prof. F. Giustino, rapporteur
Dr D. Prezzi, rapporteuse
Prof. G. Carleo, rapporteur

To those who, despite their sufferings, never stopped supporting me and caring for me

Acknowledgments

Firstly, I thank my supervisor Prof. Nicola Marzari for believing in my capabilities and giving me the opportunity to carry out a PhD in condensed matter despite my mechanical engineering background. I am grateful for his support and guidance throughout these 5 years, as well as for the trust and freedom he always granted me to follow my own ideas, and for empowering my research with all the resources necessary to maximize its outcome. I thank also all the collaborators and the colleagues which supported my research with useful discussions.

A sincere thanks to all my friends, in Switzerland and Italy, with which I shared many adventures and occasions for personal growth, and made these years so nice and memorable. I thank my family members who, despite troubles and the storms they went through, never stopped being a warm nest for me.

But, most importantly...

I thank with all my heart those people who, despite their problems and sufferings, never stopped supporting me and caring for me.

Abstract

The enormous advancements in the ability to detect and manipulate single quantum states have lead to the emerging field of *quantum technologies*. Among these, quantum computation is the most far-reaching and challenging, aiming to solve problems that the classic computers could never address because of the exponential scaling, while quantum sensing exploits the ability to address single quantum states to realize ultra-sensitive and precise detectors.

Defect centers in semiconductors play a primary role in these fields. The possibility to store information in the spin of their ground state, manipulate it through microwaves, and read it optically allows to use them as qubits. In addition, the very sharp dependence of their properties on temperature, strain and magnetic fields makes them very promising quantum sensors.

In this Thesis we aim at contributing to the progress of quantum technologies both at the hardware and software level.

From a hardware point of view, we study a key property of defect centers in semiconductors, the phonon-assisted luminescence, which can be measured to perform the readout of the information stored in a quantum bit, or to detect temperature variations. We predict the luminescence and study the exciton-phonon couplings within a rigorous many-body perturbation theory framework, an analysis that has never been performed for defect centers. In particular, we study the optical emission of the negatively-charged boron vacancy in 2D hexagonal boron nitride, which currently stands out among defect centers in 2D materials thanks to its promise for applications in quantum information and quantum sensing. We show that phonons are responsible for the observed luminescence, which otherwise would be dark due to symmetry. We also show that the symmetry breaking induced by the static Jahn-Teller effect is not able to describe the presence of the experimentally observed peak at 1.5 eV.

The knowledge of the coupling between electrons and phonons is fundamental for the accurate prediction of all the features of the photoluminescence spectrum. However, the large number of atoms in a defect supercell hinders the possibility use density functional perturbation theory to study this coupling. In this work we present a finite-differences technique to calculate the electron-phonon matrix elements, which exploits the symmetries of the defect in such a way to use the very same set of displacement needed for the calculation of phonons.

Abstract

The computation of electron-phonon coupling thus becomes a simple post-processing of the finite-differences phonons calculation.

On the quantum software side, we propose an improved quantum algorithm to calculate the Green's function through real-time propagation, and use it to compute the retarded Green's function for the 2-, 3- and 4-site Hubbard models. This novel protocol significantly reduces the number of controlled operations when compared to those previously suggested in literature. Such reduction is quite remarkable when considering the 2-site Hubbard model, for which we show that it is possible to obtain the exact time propagation of the $|N \pm 1\rangle$ states by exponentiating one single Pauli component of the Hamiltonian, allowing us to perform the calculations on an actual superconducting quantum processor.

Résumé

Les énormes progrès réalisés dans la capacité de détecter et de manipuler des états quantiques uniques ont conduit au domaine émergent des *technologies quantiques*. Le calcul quantique est l'un des plus ambitieux et des plus difficiles d'entre eux, visant à résoudre des problèmes que les ordinateurs classiques ne pourraient jamais résoudre en raison de la mise à l'échelle exponentielle, tandis que la détection quantique exploite la capacité d'adresser des états quantiques uniques pour réaliser des détecteurs ultra-sensibles et précis.

Les centres de défaut dans les semi-conducteurs jouent un rôle primordial dans ces domaines: la possibilité de stocker des informations dans le spin de leur état fondamental, de les manipuler par micro-ondes et de les lire optiquement permet de les utiliser comme des qubits, et la très forte dépendance de leurs propriétés à la température, les contraintes et les champs magnétiques en font des capteurs quantiques très prometteurs.

Dans cette Thèse, nous visons à contribuer au progrès des technologies quantiques tant au niveau matériel que logiciel.

D'un point de vue matériel, nous étudions une propriété essentielle des centres de défaut dans les semi-conducteurs, la luminescence assistée par phonons, qui peut être mesurée pour effectuer la lecture de l'information stockée dans un bit quantique, ou pour détecter des variations de température. Nous prédisons la luminescence et étudions les couplages exciton-phonon dans un cadre rigoureux de théorie des perturbations à plusieurs corps, une analyse qui n'a jamais été effectuée pour les centres de défaut. En particulier, nous étudions l'émission optique de la lacune de bore chargée négativement dans le nitrure de bore hexagonal 2D, qui se distingue actuellement parmi les centres de défauts dans les matériaux 2D grâce à sa promesse d'applications en information quantique et détection quantique. Nous montrons que les phonons sont responsables de la luminescence observée, qui autrement serait sombre en raison de la symétrie. Nous montrons également que la brisure de symétrie induite par l'effet Jahn-Teller statique n'est pas en mesure de décrire la présence du pic observé expérimentalement à 1,5 eV.

La connaissance du couplage entre électrons et phonons est fondamentale pour la prédiction précise de toutes les caractéristiques du spectre de photoluminescence. Cependant, le grand nombre d'atomes dans une supercellule défectueuse limite la possibilité d'utiliser la théorie

Résumé

des perturbations fonctionnelles de densité pour calculer les éléments de la matrice électron-phonon. Dans ce travail, nous présentons une technique de différences finies pour calculer le couplage électron-phonon, qui exploite les symétries du défaut de manière à utiliser le même jeu de déplacement nécessaire pour le calcul des phonons. Le couplage électron-phonon devient ainsi un simple post-traitement du calcul des phonons aux différences finies.

Du côté du logiciel quantique, nous proposons un algorithme quantique amélioré pour calculer la fonction de Green par propagation en temps réel, et l'utiliser pour calculer la fonction de Green retardée pour les modèles Hubbard à 2, 3 et 4 sites. Ce nouveau protocole réduit considérablement le nombre d'opérations contrôlées par rapport à celles précédemment suggérées dans la littérature. Une telle réduction est tout à fait remarquable si l'on considère le modèle de Hubbard à 2 sites, pour lequel nous montrons qu'il est possible d'obtenir la propagation temporelle exacte des états $|N \pm 1\rangle$ par exponentiation d'une seule composante de Pauli de l'Hamiltonien, nous permettant d'effectuer les calculs sur un véritable processeur quantique supraconducteur.

Contents

Acknowledgments	i
Abstract	iii
Résumé	v
List of Figures	xi
List of Tables	xvii
List of Acronyms	xix
1 Introduction	1
2 Theoretical background	5
2.1 Density functional theory	5
2.1.1 The many-body problem	5
2.1.2 Kohn-Sham equations	6
2.1.3 Successes and failures of DFT	9
2.2 Many Body perturbation theory	9
2.2.1 The many-body problem in second quantization	10
2.2.2 Interaction picture	11
2.2.3 Gell-Mann and Low theorem	13
2.2.4 Single particle Green's function	13
2.2.5 Perturbation theory for the Green's functions	15
2.2.6 Dyson equation	17
2.2.7 Optical properties of crystals	20
2.2.8 Two particles Green's function	24
2.3 Photoluminescence	27
2.3.1 Nonequilibrium Green's functions	27
2.3.2 A NEGF theory of the photoluminescence	29
2.4 Phonons	31
2.4.1 Diagonalization of the harmonic Hamiltonian	31
2.4.2 Electron-phonon coupling	33

3	Quantum computing	35
3.1	Quantum software	35
3.1.1	Quantum circuits	37
3.1.2	Measurement	40
3.1.3	Errors	42
3.1.4	Quantum annealing	42
3.2	Quantum hardware	43
3.2.1	Superconducting qubits	44
3.2.2	Defect centers in semiconductors	48
4	Phonon-assisted luminescence in V_B^-	53
4.1	Electronic structure and excitons in pristine hBN	54
4.2	Electronic structure of V_B^-	55
4.3	Optical absorption and excitons	58
4.4	Photoluminescence of V_B^-	60
4.4.1	<i>Purely-electronic</i> luminescence	60
4.5	Jahn-Teller distortion	61
4.6	Phonon-assisted luminescence	63
4.7	Analysis of the phonon modes	67
4.8	Luminescence spectra via the Van Roosbroeck–Shockley relation	69
4.9	Single-phonon spectrum	70
4.10	Limitations and future perspectives	74
5	Electron-phonon coupling through finite differences	75
5.1	Finite differences	76
5.1.1	Non-local part of the KS potential	76
5.1.2	Local part of the KS potential	77
5.2	Second derivatives	80
5.3	Workflow	80
5.4	Comparison with DFPT	81
5.5	Future perspectives	83
6	Green’s function on a current quantum processor	85
6.1	Introduction	85
6.2	Green’s function through real-time evolution	87
6.3	Choice of the variational form for the VQS	87
6.4	Optimized algorithm	91
6.5	2-site Hubbard model	94
6.6	Scaling to larger problem sizes	97
6.7	Hardware results	100
6.8	Details about the calculation of the Green’s function	104
	Conclusions	107

A	Appendix	109
A.1	Functional derivatives	109
A.2	Character tables and product rules	111
B		113
B.1	Geometry of McLachlan principle	113
B.2	Exact limit of the VAH ansatz	113
B.3	Algebraic properties of Pauli matrices	114
B.4	Pauli weight of Hubbard models	115
	Bibliography	129
	Curriculum vitae	131

List of Figures

- 2.1 Panel (a) shows the only topologically inequivalent first order ($v=1$) diagrams, while panel (b) shows some examples of second order ($v=2$) diagrams. 18
- 2.2 This figure shows that the improper self-energy (represented with a double-striped texture) can be expanded in a series of the proper self-energy (represented with a striped texture) and the non-interacting Green's function. This relation stems from the definition of Σ and Σ^* and the topological properties of the Feynman diagrams. By performing a partial summation of the diagrams in the r.h.s we obtain Eq. 2.65. 19
- 2.3 Panel (a) and (b) represent the only two topologically inequivalent diagrams for the calculation of the improper self-energy at the first order in perturbation theory. The first diagram corresponds to the Fock exchange term, while the second diagram to the Hartree repulsion between electrons. The bold oriented line represents the interacting Green's function G , and the double wiggled line corresponds to the screened interaction W . Note that in panel (b) only the interaction in the exchange term is screened, in order to avoid double counting in the sum of diagrams for the Hartree term. 21
- 2.4 First order diagrams for Ξ . The one at left has the meaning of a screened Fock exchange, while that at the right of an unscreened Hartree interaction. The diagram at the right is unscreened to avoid double counting. 25
- 2.5 This figure shows the contour introduced in the main text. The red arrows indicate its direction. Although the branches $\Gamma_{+/-}$ are pictorially represented as shifted with respect to the real t axis, they actually do coincide with the latter. 28
- 3.1 The figure shows the Bloch sphere. Any point on its surface corresponds to one possible qubit state. Particularly, the north and south pole correspond to the pure states $|0\rangle$ and $|1\rangle$ respectively. 36
- 3.2 Circuit corresponding to the Hadamard test. The slash appearing in the bottom line indicates that it refers to multiple qubits, whose initial state is $|\psi\rangle$ 41

3.3	As it can be easily seen in panel (b), the energetic levels of the linear LC circuit (a) are equally spaced, making it impossible to address the transition $ 0\rangle \rightarrow 1\rangle$ individually. The insertion of a non-linear induction in the circuit (c) adds a small anharmonicity, as a consequence of which the energy levels are not equally spaced anymore, as shown in panel (d). This allows to address the transition $ 0\rangle \rightarrow 1\rangle$ without affecting the others.	45
3.4	Example of IBM Quantum processor making use of 4 superconducting qubits.	48
3.5	Energy diagram for the lowest states of the negatively charged nitrogen vacancy center in diamond. The 0 and ± 1 levels of the ground state triplet are split of 2.88 GHz. These levels correspond to the qubit states $ 0\rangle$ ($m_s = 0$) and $ 1\rangle$ ($m_s = \pm 1$). The spin conserving excitation (green arrow) can link only levels with the same spin 0 or ± 1 . The IC from 3E to A is much more likely if the spin is ± 1 , as symbolized by the thicker arrow.	49
3.6	The red line marked with $n_{ 0\rangle}$ shows the average count of phonons emitted when the state is initially $ 0\rangle$, and is more intense than the grey line marked with $n_{ 1\rangle}$, corresponding to the initial state $ 1\rangle$. The difference between these two curves, reported in the lower part of the graph, is proportional to the fidelity of the measurement, i.e. how precisely the two states can be distinguished.	50
4.1	Structure of the 2D hBN.	54
4.2	the band structure of pristine 2D hBN, calculated at the DFT (black) and GW (red) level of theory.	55
4.3	This figure shows the absorption spectrum of the pristine hBN.	56
4.4	Ground state geometry of V_B^- in 2D hBN.	57
4.5	Wavefunction of a spin down defect level of symmetry a_1' . We can see that it is very localised around the vacancy, and possesses all the symmetries of the D_{3h} group.	57
4.6	This figure shows the defect levels inside the band-gap in V_B^- . The blue lines on the left correspond to the spin up levels, while the red lines on the right to the spin down ones.	58
4.7	Absorption spectrum for V_B^- center in 2D hBN (purple line) and for the pristine 2D hBN (light blue line). The blue circles represent the strength of the excitons of the defected system as a function of their energy.	59
4.8	Panel (a) shows the defect levels inside the band-gap for V_B^- center in 2D hBN, determined through G_0W_0 calculations. The blue and red lines represent spin up and spin down levels respectively. The yellow and grey circles represent pictorially the non-equilibrium occupations of the levels. Panel (b) shows the non-equilibrium occupations of the defect levels as a function of their non-renormalized energies. The black arrows mark the only possible recombinations which can give rise to photoluminescence.	60

4.9	The phonon-independent photoluminescence spectrum of the original symmetric system (purple solid line) is compared to that of the Jahn-Teller distorted system (light blue solid line). The roman numbers indicate which of the recombinations reported in Fig. 4.8b is associated to the peak. The activation of the transition $a_1 \rightarrow b_2$ caused by the symmetry breaking due to the Jahn-Teller effect leads to an enhancement of the peak at 1.5 eV, which, however, is still weaker than the other two peaks and therefore not observable by experiments.	62
4.10	This figure shows the two possible geometries in which the structure is distorted by the static Jahn-Teller effect.	63
4.11	Energy levels in one of the Jahn-Teller distorted systems.	64
4.12	Theoretically predicted phonon-assisted luminescence (Eq. 4.1), normalized and compared to experiments, at T=300K. The insets shows the theoretical and experimental curves after aligning the ZPLs.	65
4.13	Panel (a) shows the exciton backbone, as defined in Eq. 4.2 and normalized. It is clearly dominated by a main excitonic peak at 1.50 eV (λ_1), which is assumed to coincide with the ZPL of the system, while a smaller detached peak appears at 1.39 eV (λ_2). Panel (b) represents instead the exciton phonon coupling function, as defined in Eq. 4.3 . The phonon modes that couple most strongly with excitons are enlightened with coloured lines and reported in the legend in decreasing order of contribution, while the other phonon modes are represented with grey lines. Mode $\nu = 24$ is not among those coupling most strongly with excitons; however, its contribution to the PL will become one of the highest when including the Bose-Einstein terms, as shown in the SI.	66
4.14	Contribution of each phonon to the luminescent emission at T=0K (panel a) and T=300K (panel b). The phonon modes which couple most strongly with excitons are enlightened with coloured lines while the other phonon modes are represented with grey lines.	67
4.15	Temperature dependence of the phonon-assisted luminescence spectrum. The pair of dots which are plotted for each spectrum show the points where it has a value which is half its maximum (full width at half maximum - FWHM). The inset shows the behaviour of this FWHM (in meV) as a function of temperature. Note that the increase of the curves along the vertical axis is not quantitative, as Eq. 4.1 does not fix the amplitude of the PL spectrum: only the shape and width are relevant.	68
4.16	Theoretically predicted phonon-assisted luminescence (Eq. 4.1), at T=0K, is compared to the experiments, at 77K. The inset shows the theoretical and experimental curves after aligning the ZPLs.	69
4.17	Phonon density of states	70
4.18	The upper panel shows the radial density of displacement $d_\nu(r)$ as defined in Eq. 4.5 for the phonons with the highest localisation factor f^ν . The black dashed line indicates the radial number density. The lower panel represents the average displacement as defined in Eq. 4.7.	71

List of Figures

4.19	Representation of the eigenvector of the phonon mode $\nu = 120$	72
4.20	Panel (a) shows the phonon-assisted PL spectrum via the Van Roosbroeck-Shockley relation, obtained considering the contribution of all the phonon modes. Panel (b) instead shows the PL spectrum obtained when considering uniquely the contribution of the phonon mode $\nu=120$. In the latter case, the linewidth of the phonon mode has been broadened in order to match that of the experimental peak.	72
4.21	The violet dashed line is obtained from the MBPT approach of the main text when excluding the contribution of the phonon modes of symmetry A_1'' , A_2'' and E'' . This curve is compared to the result from the HR method, represented in green solid line. The solid violet line represents the PL calculated through the MBPT approach when including the contribution of all the phonons, while the solid blue curve represents the experimental PL.	74
5.1	The knowledge of the first derivative of the potential in the direction marked with red arrow in panel (a) allows to determine the first derivatives of the potentials along the directions marked with blue arrows. Equivalently, the knowledge of the curvature on the direction marked by the pair of red arrows in panel (b) allows to determine the curvature along the directions marked by the pairs of blue arrows.	79
5.2	Workflow for the calculation of EP matrix elements through finite differences. .	81
5.3	EP elements calculated through DFPT (x axis) are compared to those determined through finite differences (y axis). In both cases, the elements have been symmetrized, in order to remove the gauge-dependence.	82
6.1	Example of quantum circuit which is equal to the identity when $\bar{\theta} = 0$	90
6.2	Panel (a) shows the circuit for the calculation of correlation functions previously suggested in literature. It is important to stress that such approach works only if $U(\bar{\theta})$ approximates accurately the time evolution of the states $ \psi\rangle$ and $P_j \psi\rangle$; otherwise it becomes necessary to adopt the quantum circuit shown in panel (b), which requires a controlled $U(\bar{\theta})$	92
6.3	Panel (a) shows an example of the circuit corresponding to the exponential of the four-qubit Pauli gate ZXZY (namely $e^{-i\theta ZXZY}$). Panel (b) shows its controlled form. Notice that the controlled form is realized by simply controlling the central Rz gate alone. As a result, the controlled VHA simply requires the addition of a control operation for each appearing Pauli term, which is minimal considering that the exponential of a n -qubit Pauli gates requires at most $2(n - 1)$ CNOTS. .	93
6.4	Panel (a) shows the circuit to calculate the bracket of Eq. 6.20. When $\phi = 0$, the Z-measurement of the first qubit gives the real part of the bracket, while the imaginary part can be obtained by setting $\phi = -\frac{\pi}{2}$. The controlled operations on the Pauli gates P_i and P_j can be further removed if $P_i = P_j$, as shown in panel (b).	94

6.5	Real and imaginary part of the retarded Green's function G^R calculated at $k = \pi \uparrow$. The black line corresponds to the exact Green's function, the green squares to the Green's function obtained through the OS algorithm, and the light blue circles and the violet diamonds to those calculated through the CF algorithm with depth equal to 1 and 2 respectively.	98
6.6	Panel (a) shows the real and imaginary time retarded Green's function calculated at $c_k = c_{1\uparrow} - c_{2\uparrow}$ for the 3-site Hubbard model with the different algorithms analysed up to now. Since the ground state is degenerate, we consider the first diagonal component, which is obtained by sandwiching the operator $U^\dagger c_k U c_k^\dagger$ with one of the ground states $ \psi_1\rangle$. Panel (b) shows the real and imaginary time retarded Green's function calculated at $c_k = c_{1\uparrow} - c_{2\uparrow}$ for the 4-site Hubbard model.	100
6.7	Circuit required to calculate the bracket in Eq. 6.20 when $P_i = P_j = \text{XIII}$ at $t = 0$. The part of the circuit which is enclosed in the red rectangle corresponds to the variational form adopted for the VQE.	101
6.8	Panel (a) shows the retarded Green's function in time domain. The grey and green solid lines correspond to the exact real and imaginary parts respectively. The grey and green squares correspond to the results from the hardware. The dotted lines are obtained by interpolating the hardware result with splines. Panel (b) shows the imaginary part of the retarded Green's function in frequency domain. The blue and the red solid lines correspond respectively to the exact result and the quantum calculation. Panels (c) and (d) show the same quantities as Panels (a) and (b), with the only difference that now the Green's function is calculated using the exact energy $E_0 = -4$ in the phase factor $e^{iE_0 t}$ of Eq. 6.20.	103
6.9	VQE algorithm for the ground state on <i>ibmq_manila</i> . The blue dashed line corresponds to the exact value, while the red line to the quantum calculation. .	104
6.10	Layout of <i>ibmq_montreal</i> . The qubits used in the calculation of the Green's function are those circled in red.	105

List of Tables

6.1	Sign of the prefactor multiplying $\tilde{P} \chi\rangle$. The Pauli matrices in the left column are components of the qubit Hamiltonian, with coefficient reported in the last column, while the Pauli matrices in the top row correspond to the fermion creation/annihilation operator in the qubit Hilbert space.	96
6.2	Number of 1-qubit and 2-qubit gates in the ansätze adopted to calculate the Green's function for the Hubbard model. The number reported for the OS algorithm corresponds to the controlled form of the ansatz, which is the one adopted to calculate the Green's function.	99
A.1	Product table for the D_{3h} group.	112
A.2	Product table for the C_{2v} group.	112

List of Acronyms

BSE	Bethe-Salpeter equation
CF	control free
DFT	density-functional theory
EP	electron-phonon
HK	Hohenberg-Kohn
HR	Huang-Rhys
IC	intersystem crossing
KS	Kohn-Sham
MBPT	many-body perturbation theory
NEGF	nonequilibrium Green's functions
OS	one state
PES	potential energy surface
PL	photoluminescence
scf	self-consistent field
VHA	variational Hamiltonian ansatz
xc	exchange-correlation
ZPL	zero-phonon line

1 Introduction

In the last decades, the human society has met an unprecedented growth, which has led to the globalized and interconnected world in which we live. This exceptional growth, which was made possible by the incredible development of the technology, has caused the continuous demand for more and more performing *materials*. A striking example is provided by the role of the semiconductors in the miniaturization of the transistors, which allowed an exponential increase with years of the computers power, known as *Moore law*. The need for novel materials is not limited to the field of electronics, but interests all the technological fields, from drugs design to the energy production, thus it should not surprise if the European Union instituted recently the one billion euros Graphene flagship, aimed at exploiting the exceptional characteristics of this 2D material [1, 2, 3].

The materials properties could be predicted with perfect accuracy by solving the fundamental equations of quantum mechanics. It is paradoxical and fascinating at the same time that, although we know these equations since the beginning of 20th century, we are still not able to solve them *exactly*, given the astonishing complexity of the mathematics. For this reason, it is necessary to simplify these problems through *approximations* and solve them *numerically*. Here is where the computational Material Science enters. Its great advantage with respect to experiments is that it allows to predict the properties of materials with a cost, in term of money and time, which is orders of magnitudes lower, and an accuracy which gets better and better as soon as the solution to the equations gets closer to the exact one. Unfortunately, due to the complexity of the equations of quantum mechanics, computational physics is currently able to study relatively simple models compared to the elaborated experimental setups. The need to investigate phenomena which are more and more complicated, with an increasing level of accuracy, requires always more computational resources. For decades the exponential growth in computers power has provided the capabilities to push further and further the research in materials science. However, the imminent end of Moore's law, due to the impossibility to further miniaturize the transistors (that have already reached an atomic scale), poses the question of how further increase the computational capabilities. It may thus become necessary to look for novel paradigms of calculation.

In the eighties, the Nobel Prize Richard Feynman suggested that a computer made up of *quantum* bits, i.e. two levels system obeying the laws of quantum mechanics, had the potential to solve physical problems that classic computer could not. This was motivated by the fact that the system of qubits obeys the physical laws described by very same equations that we want to solve, thus allowing to map the mathematical problems into their quantum state. Starting from this suggestion (and from those of other scientists which contributed in the same fundamental way), the idea of *quantum computer* took place. The fundamental results obtained few years later led to establish quantum computers as potential tools for future development. The most famous among these results is probably the Shor's algorithm [4], which proved that the integer factorization could be efficiently solved on a quantum computer, with astonishing consequences in the word of cryptography. The enthusiasm generated by these theoretical results further motivated the research in hardware for quantum computing. Industrial giants such as Google, IBM, Microsoft, Intel, invested billions of dollars in the development of quantum processors [5], betting on different technologies. Google and IBM have focused their research on superconducting qubits, micrometer-size circuits behaving as quantum anharmonic oscillators, but many other promising technologies have been developed such as trapped ions, quantum dots in silicon, Rydberg atom arrays and photonic chips.

Quantum computing is one of the recently emerged *quantum technologies*. These technologies are based on the individual control of a *single quantum state*, which, due to the extreme complexity, has become possible only recently, allowing unprecedented applications thanks to the possibility to exploit the extraordinary properties of the quantum world. One example is represented by *quantum communication*, which exploits quantum mechanical principles such as *superposition*, *entanglement* and the *no cloning theorem* to guarantee a theoretically secure transmission of data, with applications in cryptography problems such as that of the key exchange. Another example is represented by *quantum sensing*, which exploits the very sharp sensitivity of a quantum state on the surrounding environment to realize ultra-accurate and precise detectors.

Defect centers in semiconductors play a primary role in this context, due to their application in quantum computing [6], quantum communication [7, 8] and quantum sensing [9, 10, 11, 12, 13]. Quantum information is stored in the spin of their ground state, and is addressed optically: it is initialized in the logical $|0\rangle$ thanks to optical pumping cycles, and manipulated through the irradiation with microwaves; the readout exploits the dependence of photoluminescence emission from the spin to discriminate the $|0\rangle$ and the $|1\rangle$ states. The optical properties not only play a very important role in quantum computing/communication protocols: the photoluminescence spectrum is also used for the characterization of the defects and for quantum sensing, as its features depend sharply on external factors such as temperature and strain.

Very recently, the search for novel defect centers, aimed at overcoming the limitations of the existing ones in term of coherence, resolution and interfaciability with cavities and resonators, has lead to the exploration of the world of 2D materials. In 2019, the negatively charged boron vacancy in 2D hexagonal boron nitride (V_B^-) was predicted to be responsive to optically

detected magnetic resonance [14], and thus being able to store quantum information in its ground state, representing a potential qubit candidate. Despite the great interest that this material has attracted, its optical properties are still not understood. An accurate first-principles prediction of the luminescence is thus necessary for the progress in this research field and is one of the goals of this Thesis.

In this Thesis, we address both aspects of the quantum technology, i.e. quantum hardware and software. On the hardware side, we study the photoluminescence of the V_B^- qubit using many-body perturbation theory. This formulation provides a natural and accurate framework to predict the optical properties of materials, and has never been applied before to study the photoluminescence in defect centers due to the challenges posed by their big supercells and the consequent computational cost. An additional complexity is due to the fact that luminescence in defect centers is phonon-assisted, thus requiring the simulation of the interaction between excitons and phonons. We face these challenges and calculate the exciton-phonon coupling for V_B^- in 2D hBN, and predict a luminescence spectrum which is in very good agreement with experiments.

The central object of the many-body perturbation theory used for the calculation described above is the Green's function, whose knowledge provides fundamental information, such as the energy spectrum of the Hamiltonian, the expectation values of operators and the response to perturbations. The computation of the exact Green's function on a classical computer is known to become exponentially hard when increasing the size of the problem, as it requires the knowledge of the exact ground state. In many body perturbation theory the Green's function is expanded in a perturbation series, but, due to the computational cost, only the very first order diagrams are retained in practical calculations. This approximation provides good results in some cases, e.g. the calculation of optical properties, but fails dramatically in others, for example when studying strongly correlated materials. It becomes thus very attractive to exploit the potentiality of a quantum computer and devise a quantum algorithm for the calculation of the exact Green's function. This is done in the second part of the Thesis, dedicated to the quantum software. We design a novel quantum algorithm for the calculation of the single particle Green's function which exploits the time evolution of the quantum states. This algorithm allows to reduce remarkably the depth of the circuits compared to those previously presented in literature, thus allowing to perform calculation on the current noisy intermediate scale quantum processors (NISQ) for the two-site Hubbard model, with very good agreement between the experiments and the exact solution. The scaling of the proposed algorithm with the size of the system is assessed and compared to that of the algorithms already existing in literature.

This Thesis is organized as follows.

In Chapter 2, we illustrate the theoretical framework behind the first principles calculations of the optical properties. We first introduce density functional theory, which is by far the most used technique for the calculation of the ground state properties of materials, and then move to the more complicated many-body perturbation theory, which allows a better prediction

of the excited state properties. Finally we solve the problem of the motion of nuclei in an harmonic potential and introduce the concept of phonons and electron-phonon coupling. In Chapter 3, we present the basics of quantum computing. We start from the concept of *qubit*, quantum circuits, and measurement and show how a quantum algorithm works. We then introduce two possible technologies for the realization of quantum hardware, the superconducting qubits, which are implemented in the IBM Quantum processors used in this work, and the defect centers in semiconductors, which are the object of our first-principles calculation of the optical properties.

These optical properties are studied in Chapter 4 for the negatively charged boron vacancy in 2D hBN (V_B^-). We first determine its electronic structure and optical absorption, and compare them with those of the pristine 2D hBN. We then introduce the theory of the luminescence and use it to calculate the spectrum of V_B^- . We assess the contribution to the emission of the Jahn-Teller distortion, and show that it is negligible with respect to that of the phonons. We also discuss the comparison with the Huang-Rhys method, which is widely used to determine the photoluminescence in defect centers.

In Chapter 5, we present a technique for the computation of the electron-phonon coupling matrix elements in defects. This technique, based on the finite differences method, exploits the symmetries of the system in order to use the very same set of displacement necessary to calculate phonons, thus allowing to determine the electron-phonon matrix elements as a simple postprocessing operation.

Finally, in Chapter 6 we present an efficient algorithm for the calculation of the Green's function on a current quantum processor, through the time evolution technique. We first review the technique of the *variational quantum simulation*, and illustrate the requisites which should be satisfied in order to guarantee a correct time evolution of a quantum state. We then show how the suggested algorithm satisfies all these requisites, and prove that it requires circuits which are considerably shallower with respect to other algorithms already presented in literature. We finally use this algorithm for the calculation of the Green's function on a current IBM Quantum processor, obtaining results in very good agreement with the exact solution.

2 Theoretical background

In this Chapter we introduce density functional theory (DFT)[15, 16] and many-body perturbation theory (MBPT) [17, 18, 19], and illustrate their application for the calculation of the optical properties of defects. Unless explicitly stated, we will make use of the Hartree natural units.

2.1 Density functional theory

2.1.1 The many-body problem

The general matter Hamiltonian for a crystal is

$$\hat{H} = \hat{T}_{el}(\mathbf{r}) + \hat{T}_{ion}(\mathbf{R}) + \hat{V}_{el-el}(\mathbf{r}) + \hat{V}_{el-ion}(\mathbf{r}, \mathbf{R}) + \hat{V}_{ion-ion}(\mathbf{R}) . \quad (2.1)$$

Here \mathbf{r} and \mathbf{R} indicate respectively the set of all the electronic and nuclei coordinates. \hat{T}_{el} and \hat{T}_{ion} are the kinetic energy operators for electrons and nuclei, while \hat{V}_{el-el} , $\hat{V}_{ion-ion}$ and \hat{V}_{el-ion} represent the electron-electron, ion-ion and electron-ion Coulombic interactions. The number of variables appearing in Eq.2.1 grows linearly with the number of electrons and ions, leading to a Hilbert space whose size scales exponentially with the number of particles. The eigenvalue problem

$$\hat{H}|\Phi\rangle = E|\Phi\rangle , \quad (2.2)$$

necessary to calculate the eigenstates of the Hamiltonian, and determine consequently the properties of the materials, is thus intractable. Fortunately, we can significantly simplify the Hamiltonian in Eq. 2.1 by making the following observation: since the mass of the nuclei is at least three orders of magnitudes larger than that of the electrons, their kinetic energy \hat{T}_{ion} is much smaller than \hat{T}_{el} . Therefore \hat{T}_{ion} can be treated as a perturbation to the total Hamiltonian \hat{H} and thus be neglected at the lowest order of theory. This approximation, which was initially proposed by Max Born and Robert Oppenheimer, allows to decompose the coupled electron-nuclei problem into two simpler problems. In fact, without the ions kinetic energy operator \hat{T}_{ion} , the total wave function Φ can be separated into a nuclear part $\chi(\mathbf{R})$ and

electronic part $\Psi(\mathbf{r}, \mathbf{R})$.

$$\Phi(\mathbf{r}, \mathbf{R}) = \chi(\mathbf{R})\Psi(\mathbf{r}, \mathbf{R}) \quad (2.3)$$

First, the purely electronic eigenvalue problems must be solved,

$$[\hat{T}_{el}(\mathbf{R}) + \hat{V}_{el-ion}(\mathbf{r}, \mathbf{R}) + \hat{V}_{el-el}(\mathbf{r})]\Psi_n(\mathbf{r}, \mathbf{R}) = E_n(\mathbf{R})\Psi_n(\mathbf{r}, \mathbf{R}), \quad (2.4)$$

where the nuclei coordinates can be treated as parameters given the absence of the derivatives with respect to \mathbf{R} contained inside the nuclei kinetic energy. Once the electronic energies $E_n(\mathbf{R})$ are computed, the nuclear energies can be calculated:

$$[\hat{T}_{ion-ion} + \hat{V}_{ion-ion}(\mathbf{R}) + E_n(\mathbf{R})]\chi_m(\mathbf{R}) = W_{nm}\chi_m(\mathbf{R}). \quad (2.5)$$

Despite the simplification brought by the Born-Oppenheimer approximation, the solution of Eq. 2.4 remains a formidable task, which can be accomplished analytically only in few simple cases, and numerically for small molecules with few electrons. In the following, we will briefly illustrate some of the attempts to find an approximate solution to this problem, which led to the formulation of the very successful DFT [20, 21], that is currently the most adopted framework to study the properties of materials.

2.1.2 Kohn-Sham equations

The attempts to find an approximate strategy to solve Eq. 2.4 are numerous and their review goes beyond the purpose of this work. In this section we consider only those which paved the road to DFT, as they help understanding the main concepts and ideas behind this theory. We shall start from the idea of Douglass Hartree, who, in 1927, thought to exploit the *variational principle* to find the ground state energy of the electronic Hamiltonian:

$$\min_{\langle \Phi |} \langle \Phi | \hat{H}_{el} | \Phi \rangle = \langle \Psi_0 | \hat{H}_{el} | \Psi_0 \rangle = E_0. \quad (2.6)$$

Here $|\Psi_0\rangle$ and E_0 are the ground state of the electronic problem and its energy. Thanks to Eq. 2.6, an approximate form of the ground state can be obtained by minimizing the energy of a tentative wavefunction, also called *ansatz*. The ansatz chosen by Hartree consisted in the product of single particle wavefunctions,

$$\Psi(\mathbf{x}_1, \mathbf{x}_2, \dots, \mathbf{x}_N) = \phi_1(\mathbf{x}_1)\phi_2(\mathbf{x}_2)\dots\phi_N(\mathbf{x}_N). \quad (2.7)$$

By imposing the minimization condition expressed in Eq. 2.6, Hartree derived the following set of differential equations:

$$\left[-\frac{\nabla^2}{2} + v_{ext}(\mathbf{x}) + \sum_{j \neq i} \int d^3\mathbf{x}' \frac{\phi_j^*(\mathbf{x}')\phi_j(\mathbf{x}')}{|\mathbf{x} - \mathbf{x}'|} \right] \phi_i(\mathbf{x}) = E_i \phi_i(\mathbf{x}), \quad (2.8)$$

where the index i runs from 1 to the number of particles N . The fundamental result achieved by Hartree was to map an entangled N -body problem into N *single-particle problems*, where the electrons interact through an effective potential. This overall potential is made up of two terms. The external potential

$$v_{ext}(\mathbf{x}) = \sum_I \frac{-Z_I}{|\mathbf{x} - \mathbf{R}_I|} \quad (2.9)$$

is the attractive Coulombic potential generated by the nuclei on the electrons, while the Hartree potential

$$v_H(\mathbf{x}) = \sum_{j \neq i} \int d^3\mathbf{x}' \frac{\phi_j^*(\mathbf{x}')\phi_j(\mathbf{x}')}{|\mathbf{x} - \mathbf{x}'|} \quad (2.10)$$

expresses the repulsive Coulombic potential generated by the surrounding electrons. Although very important from a conceptual point of view, Hartree equations give a poor description of the properties of the materials. The main reason lies in the wrong choice of the ansatz. In fact, Eq. 2.7 does not respect the Pauli exclusion principle, which forces the wavefunction to be antisymmetric with respect to the exchange of electrons. In order to overcome this limitation, Vladimir Fock replaced the ansatz proposed by Hartree with its anti-symmetric form:

$$\Psi(\mathbf{x}_1, \mathbf{x}_2, \dots, \mathbf{x}_N) = \sum_P (-1)^{\text{sgn}P} \phi_{P_1}(\mathbf{x}_1) \phi_{P_2}(\mathbf{x}_2) \dots \phi_{P_N}(\mathbf{x}_N) \quad (2.11)$$

where the sum is carried over all the possible permutations of particles P and the sign of the permutation is negative when the number of particles swap is odd. The minimization of the energy functional with the new ansatz leads to a set of differential equations that are equal to Hartree equations but for an additional term,

$$\langle \mathbf{x} | v_x | \phi_i \rangle = \sum_{i \neq j} \int d^3\mathbf{x}' \frac{\phi_j^*(\mathbf{x}')\phi_j(\mathbf{x}')}{|\mathbf{x} - \mathbf{x}'|} \phi_i(\mathbf{x}'), \quad (2.12)$$

representing the action of the so-called *exchange potential* on the i -th electron. The Hartree-Fock method takes correctly into account the electronic correlations due to the Pauli exclusion principle, but not those due to the Coulombic interaction. Therefore we need to perform a further step and include these correlations in the theory. Now, both Hartree and exchange potential arise from the minimization of the energy, therefore it is reasonable to expect that also the missing term comes from the minimization of a functional. The first fundamental result obtained by Hohenberg and Kohn [20] was to provide a rigorous foundation for this intuition. In fact, they showed that the exact ground state energy is a functional $E[\rho]$ of the electronic density of the system:

$$\rho(\mathbf{x}) = \int d^3\mathbf{x}_2 \dots d^3\mathbf{x}_N |\Psi(\mathbf{x}_1, \mathbf{x}_2, \dots, \mathbf{x}_N)|^2. \quad (2.13)$$

Chapter 2. Theoretical background

This result allows again to map the interacting N -electrons system into an auxiliary system of independent-particle having the same density [21]

$$\rho(\mathbf{x}) \equiv \rho_s(\mathbf{x}) = \sum_i^{N_{el}} |\phi_i(\mathbf{x})|^2, \quad (2.14)$$

as they share the same ground state energy. If we knew the exact expression of the functional $E[\rho]$, we could minimize it and obtain the exact ground state density and energy. Unfortunately, this expression is unknown and we need to find an approximate form for this functional by considering all the known contributions and guessing a good approximation for the remaining unknown ones. We start from the kinetic energy functional, which, for a system of independent particles, reads

$$\hat{T}[\rho] = \sum_i^{N_{el}} \int d^3\mathbf{x} \phi_i^*(\mathbf{x}) \frac{-\nabla^2}{2} \phi_i(\mathbf{x}). \quad (2.15)$$

The contribution of the external potential is instead

$$\hat{V}_{ext}[\rho] = \int d^3\mathbf{x} v_{ext}(\mathbf{x}) \rho(\mathbf{x}), \quad (2.16)$$

while that of the Coulomb interaction between electron is

$$\hat{V}_H[\rho] = \int d^3\mathbf{x} d^3\mathbf{x}' \frac{\rho(\mathbf{x})\rho(\mathbf{x}')}{|\mathbf{x} - \mathbf{x}'|}. \quad (2.17)$$

It is now necessary to find a good expression for the remaining functional, expressing the exchange and correlations effects. Kohn and Sham [21] suggested to approximate this term with the exchange correlation functional for the homogeneous electron gas:

$$\hat{V}_{xc}[\rho] = \int d^3\mathbf{x} \rho(\mathbf{x}) \varepsilon_{HEG}[\rho(\mathbf{x})]. \quad (2.18)$$

The minimization of the functional given by the sum of the contribution expressed above leads to the well known Kohn-Sham (KS) equations:

$$\left[-\frac{\nabla^2}{2} + v_{ext}(\mathbf{x}) + v_H(\mathbf{x}) + v_{xc}(\mathbf{x}) \right] \phi_{n\mathbf{k}}(\mathbf{x}) = \varepsilon_{n\mathbf{k}} \phi_{n\mathbf{k}}(\mathbf{x}), \quad (2.19)$$

with

$$v_{xc}(\mathbf{x}) = \frac{d\varepsilon_{HEG}}{d\rho}[\rho(\mathbf{x})]. \quad (2.20)$$

The indexes of the wavefunctions are labeled with $\{n\mathbf{k}\}$ as the Bloch theorem holds.

2.1.3 Successes and failures of DFT

As anticipated above, DFT is the most adopted technique to predict the properties of materials. DFT allows to determine with good accuracy the ground state properties of a broad category of materials while being reasonably cheap. However, the drawbacks related to the approximate form of the exchange-correlation functional may lead to failures in the description of ground state and spectral properties.

1. First of all, DFT suffers of the error due to the *self-interaction* of an electron with the field that it generates [22]. The effect of this self-interaction is to delocalize the electronic charge density, leading to a wrong description of systems with very localized states. For this reason, DFT produces poor results for materials containing transition metals, as they usually contain very localised atomic-like states typically originating from *d* and *f* orbitals.
2. Furthermore, the effective potential, which should decade as $\frac{1}{r}$ far from the system, decays instead exponentially. This unphysical behaviour does not allow to describe, for example, Wan der Waals forces, and a modification of the exchange-correlation functional is thus needed in order to simulate them [23].
3. Another important limitation, which affects dramatically the prediction of optical properties is the band-gap underestimation [24], which can be attributed to the fact that wavefunctions corresponding to the band edges are usually localised. DFT tends once again to delocalize these states, thus reducing their energy.

The band-gap underestimation makes DFT not suitable for the study the photoluminescence of defect centers in semiconductor, therefore higher level theories must be adopted. In the next section, we will see how the MBPT formalism can be used to obtain a very accurate prediction of the optical properties.

2.2 Many Body perturbation theory

As illustrated in Sec. 2.1.1, except for some extremely simple cases, it is impossible to find an analytic solution to the many-body Schrödinger equation. Nevertheless, MBPT which is presented in this chapter provides a *formal solution* to the many-body problem, in terms of a *perturbative expansion* of the *Green's functions*. The extremely hard task of finding a solution to Eq. 2.4 is turned into a much simpler calculation of the integrals appearing in this perturbation series. If we were able to evaluate the integrals appearing at all order perturbations, we would obtain the exact solution to the many-body problem. Unfortunately, for problems of practical interests, it is possible to calculate only the very first orders of the perturbation series. Nevertheless, this approximation yields very good results when used to calculate optical properties. It is possible to derive the equations of MBPT following two equivalent approaches. The first makes use of the functional derivatives of the Green's functions and leads to the

well-known Hedin equations [25]. The second, instead, starts from the perturbative expansion of the propagator to determine a series for the Green's function. In this work we follow the latter approach [17], and, unless explicitly specified, we adopt the Einstein convention for sums.

2.2.1 The many-body problem in second quantization

The typical Hamiltonian of a Many-Body problem expressed in the second quantization formalism [19] reads

$$H = \int d^3\mathbf{x} \frac{-\nabla^2}{2} \hat{\psi}_\alpha^\dagger(\mathbf{x}) \hat{\psi}_\alpha(\mathbf{x}) + \int d^3\mathbf{x} V_{\alpha\beta}(\mathbf{x}) \hat{\psi}_\alpha^\dagger(\mathbf{x}) \hat{\psi}_\beta(\mathbf{x}) + \frac{1}{2} \int d^3\mathbf{x} d^3\mathbf{x}' \hat{\psi}_\alpha^\dagger(\mathbf{x}) \hat{\psi}_\beta^\dagger(\mathbf{x}') v_{\alpha\alpha',\beta\beta'}(\mathbf{x} - \mathbf{x}') \hat{\psi}_{\beta'}(\mathbf{x}') \hat{\psi}_{\alpha'}(\mathbf{x}) . \quad (2.21)$$

Here $\hat{\psi}_\alpha(\mathbf{x})$ is the field operator, whose action consists in destroying an electron at the position \mathbf{x} with spin α . The fields are the fundamental building blocks of the second quantization formalism, as any operator can be written as a combination of them. For example, the electron density operator can be expressed as

$$\hat{n}(\mathbf{x}) = \hat{\psi}_\alpha^\dagger(\mathbf{x}) \hat{\psi}_\alpha(\mathbf{x}) . \quad (2.22)$$

Fermion fields satisfy the following anti-commutation relation

$$\{\hat{\psi}_\alpha(\mathbf{x}), \hat{\psi}_\beta^\dagger(\mathbf{x}')\} = \delta_{\alpha,\beta} \delta(\mathbf{x} - \mathbf{x}') , \quad (2.23)$$

which completely defines their algebra. The first term in the r.h.s. of Eq. 2.21 corresponds to the kinetic energy operator, while the second and third terms describe respectively the action of the local and spin-dependent *external potential* $V_{\alpha\beta}$ and the spin-dependent interactions between fermions. In many cases of interest for condensed matter, the Hamiltonian of above can be simplified. If the spin-orbit coupling is negligible, then the external potential is diagonal in spin:

$$V_{\alpha\beta}(\mathbf{x}) = \delta_{\alpha\beta} V_\alpha(\mathbf{x}) . \quad (2.24)$$

Furthermore, if the coupling between electron spins is neglected, and electrons are assumed to interact only through Coulomb interaction, then the two-particle potential becomes:

$$v_{\alpha\alpha',\beta\beta'} = \frac{4\pi}{|\mathbf{x} - \mathbf{x}'|} \delta_{\alpha\alpha'} \delta_{\beta\beta'} . \quad (2.25)$$

These approximations hold for all the systems studied in this Thesis. The lack of spin-orbit coupling is justified by the fact that these systems are made up of light elements, while the spin-spin interaction between electrons is usually much weaker than the Coulomb interaction and represents a relativistic correction.

2.2.2 Interaction picture

Let us assume that the Hamiltonian of Eq. 2.21 can be divided into two components,

$$\hat{H} = \hat{H}_0 + \hat{H}_1 , \quad (2.26)$$

where H_1 is a perturbation. The time evolution of a state $|\Psi\rangle$ is described by the Schrödinger equation:

$$i \frac{\partial}{\partial t} |\Psi(t)\rangle = \hat{H} |\Psi(t)\rangle . \quad (2.27)$$

If \hat{H} is time independent, then the solution of Eq. 2.27 is

$$|\Psi(t)\rangle = e^{-i\hat{H}(t-t_0)} |\Psi(t_0)\rangle . \quad (2.28)$$

Let us define the interaction picture of the state $|\Psi\rangle$ as

$$|\Psi_I(t)\rangle = e^{i\hat{H}_0 t} |\Psi(t)\rangle , \quad (2.29)$$

while the interaction picture of an operator \hat{O} is

$$\hat{O}_I(t) = e^{i\hat{H}_0 t} \hat{O} e^{-i\hat{H}_0 t} . \quad (2.30)$$

The time derivative of $|\Psi_I(t)\rangle$ can be easily calculated:

$$\begin{aligned} i \frac{\partial}{\partial t} |\Psi_I(t)\rangle &= -\hat{H}_0 e^{i\hat{H}_0 t} |\Psi(t)\rangle + e^{i\hat{H}_0 t} i \frac{\partial}{\partial t} |\Psi(t)\rangle \\ &= e^{i\hat{H}_0 t} [-\hat{H}_0 + \hat{H}_0 + \hat{H}_1] e^{-i\hat{H}_0 t} |\Psi_I(t)\rangle , \end{aligned}$$

so

$$i \frac{\partial}{\partial t} |\Psi_I(t)\rangle = \hat{H}_{1,I} |\Psi_I(t)\rangle . \quad (2.31)$$

Eq. 2.31 is the Schrödinger equation in the interaction picture. At variance with Eq. 2.27, the Hamiltonian $\hat{H}_{1,I}$ is time dependent, and thus the solution of Eq. 2.31 is not as simple as for Eq. 2.28. Nevertheless, the great advantage of Eq. 2.31 is that it contains only the perturbing Hamiltonian \hat{H}_1 , paving the way for a perturbative expansion. Let us write the formal solution to Eq. 2.31 as

$$|\Psi_I(t)\rangle = \hat{U}(t, t_0) |\Psi_I(t_0)\rangle , \quad (2.32)$$

where evidently the propagator \hat{U} must satisfy the relation

$$\hat{U}(t_0, t_0) = I . \quad (2.33)$$

Chapter 2. Theoretical background

Using Eqs. 2.29 and 2.28,

$$\begin{aligned} |\Psi_I(t)\rangle &= e^{i\hat{H}_0 t} |\Psi(t)\rangle = e^{i\hat{H}_0 t} e^{-i\hat{H}(t-t_0)} |\Psi(t_0)\rangle \\ &= e^{i\hat{H}_0 t} e^{-i\hat{H}(t-t_0)} e^{-i\hat{H}_0 t_0} |\Psi_I(t_0)\rangle, \end{aligned}$$

which gives the *exact* expression for \hat{U} :

$$\hat{U}(t, t_0) = e^{i\hat{H}_0 t} e^{-i\hat{H}(t-t_0)} e^{-i\hat{H}_0 t_0}. \quad (2.34)$$

For the sake of MBPT, is much more convenient to find a perturbative expression for \hat{U} . Integrating Eq. 2.31 from t_0 to t , we obtain

$$\hat{U}(t, t_0) = I - i \int_{t_0}^t dt' \hat{H}_{1,I}(t') \hat{U}(t', t_0). \quad (2.35)$$

We can see that the propagator \hat{U} appears both at the r.h.s. and l.h.s. of Eq. 2.35, leading to an iterative solution:

$$\hat{U}(t, t_0) = I - i \int_{t_0}^t dt' \hat{H}_{1,I}(t') + (-i^2) \int_{t_0}^t dt' \int_{t_0}^{t'} dt'' \hat{H}_{1,I}(t') \hat{H}_{1,I}(t'') + \dots \quad (2.36)$$

It is straightforward to check that the second integral appearing at the r.h.s. of Eq. 2.36 can be written as:

$$\begin{aligned} \int_{t_0}^t dt' \int_{t_0}^{t'} dt'' \hat{H}_{1,I}(t') \hat{H}_{1,I}(t'') &= \frac{1}{2} \int_{t_0}^t dt' \int_{t_0}^t dt'' \hat{H}_{1,I}(t') \hat{H}_{1,I}(t'') \theta(t' - t'') \\ &\quad + \frac{1}{2} \int_{t_0}^t dt' \int_{t_0}^t dt'' \hat{H}_{1,I}(t'') \hat{H}_{1,I}(t') \theta(t'' - t'). \end{aligned}$$

Defining the *time ordering operator* T as

$$T[\hat{O}_1(t_1), \hat{O}_2(t_2) \dots \hat{O}_N(t_N)] = \sum_P \hat{O}_{P_1}(t_{P_1}) \hat{O}_{P_2}(t_{P_2}) \dots \hat{O}_{P_N}(t_{P_N}) \theta(t_{P_1}, t_{P_2}, \dots, t_{P_N}), \quad (2.37)$$

where the sum in Eq. 2.37 is over all the possible permutations P and the generalized Heaviside function $\Theta(t_1, t_2, \dots, t_N)$ is non-vanishing only if $t_1 > t_2 > \dots > t_N$, then it is possible to write the propagator as

$$\hat{U}(t - t_0) = \sum_{n=0}^{\infty} \frac{(-i)^n}{n!} \int_{t_0}^t dt_1 \dots dt_n T[\hat{H}_{1,I}(t_1), \dots, \hat{H}_{1,I}(t_n)]. \quad (2.38)$$

Eq.2.38 represents the fundamental result of this section. In fact, it allows us first to prove the Gell-Mann and Low theorem, and subsequently to write the perturbative expansion for the Green's function.

2.2.3 Gell-Mann and Low theorem

Be $|\Phi_0\rangle$ the ground state of the Hamiltonian \hat{H}_0 . Suppose to switch on at $t = -\infty$ the perturbation $e^{-\epsilon|t|} H_1$. Using Eq. 2.38, the propagator can be written as

$$\hat{U}_\epsilon(t, -\infty) = \sum_{n=0}^{\infty} \frac{(-i)^n}{n!} \int_{-\infty}^t dt_1, \dots, dt_n e^{-\epsilon(|t_1|+|t_2|+\dots+|t_n|)} T[\hat{H}_{1,I}(t_1), \dots, \hat{H}_{1,I}(t_n)] . \quad (2.39)$$

The Gell-Mann and Low theorem states that the ground state $|\Psi_0\rangle$ of the full Hamiltonian $H_0 + H_1$ can be obtained as

$$|\Psi_0\rangle = \lim_{\epsilon \rightarrow 0} \frac{\hat{U}_\epsilon(0, \pm\infty) |\Phi_0\rangle}{\langle \Phi_0 | \hat{U}_\epsilon(0, \pm\infty) | \Phi_0 \rangle} . \quad (2.40)$$

The physical meaning of this theorem is transparent: by turning on very slowly the perturbing Hamiltonian H_1 which acts on the non-interacting ground state $|\Phi_0\rangle$, this state will eventually become the ground state of the full Hamiltonian $\hat{H}_0 + \hat{H}_1$.

This has very important implications for quantum computing, lying at the core of the quantum annealing technique [26]. This technique is used to find the global minimum of an optimization problem: the cost function is first mapped on a qubit Hamiltonian. The qubits are initialized in a trivial state, then the Hamiltonian is turned on very slowly, until the state of the qubits evolves into the total Hamiltonian ground state, which minimizes the cost function (the topic is discussed in more detail in Sec. 3.1.4).

We will now combine the results in Eqs. 2.38 and 2.40 to write the perturbative expansion for the Greens' function.

2.2.4 Single particle Green's function

The central object of the MBPT is the Green's function. The single particle Green's function is defined as

$$G_{\alpha\beta}(\mathbf{x}t, \mathbf{x}'t') = -i \frac{\langle \Psi_0 | T[\hat{\psi}_{H\alpha}(\mathbf{x}, t) \hat{\psi}_{H\beta}^\dagger(\mathbf{x}'t')] | \Psi_0 \rangle}{\langle \Psi_0 | \Psi_0 \rangle} . \quad (2.41)$$

Here $|\Psi\rangle$ is the ground state of the many-body Hamiltonian, while $\hat{\psi}_{H\alpha}(\mathbf{x}, t)$ is the fermion field expressed in Heisenberg picture:

$$\hat{\psi}_{H\alpha}(\mathbf{x}, t) = e^{i\hat{H}t} \hat{\psi}_\alpha(\mathbf{x}) e^{-i\hat{H}t} . \quad (2.42)$$

The *time ordering operator* T appearing in Eq. 2.41 is generalized for fermions:

$$T[\hat{O}_1(t_1), \hat{O}_2(t_2) \dots \hat{O}_N(t_N)] = \sum_P (-1)^{\text{sgn}(P)} \hat{O}_{P_1}(t_{P_1}) \hat{O}_{P_2}(t_{P_2}) \dots \hat{O}_{P_N}(t_{P_N}) \theta(t_{P_1}, t_{P_2}, \dots, t_{P_N}) . \quad (2.43)$$

At variance with that expressed in Eq. 2.37, this operator sets the sign of the product of operators accordingly to the sign of the permutation. The two definitions are equivalent when acting on products of Hamiltonian, as each component of the Hamiltonians contains the

Chapter 2. Theoretical background

product of an even number of fields (see for example Eq. 2.22). The single Green's function possesses many important properties. First of all, it can be used to calculate the expectation values of all single particle operators. The electron density of the system can be written as

$$\rho(\mathbf{x}, t) = -i G_{\alpha\alpha}(\mathbf{x}t, \mathbf{x}t^+) , \quad (2.44)$$

where the repetition of α implies a sum as prescribed by Einstein convention, while the expression t^+ refers to $\lim_{\eta \rightarrow 0^+} (t + \eta)$. The kinetic energy of the electrons can be written instead as

$$T(t) = -i \int d^3\mathbf{x} \lim_{\mathbf{x}' \rightarrow \mathbf{x}} -\frac{\nabla^2}{2} G_{\alpha\alpha}(\mathbf{x}t, \mathbf{x}'t^+) . \quad (2.45)$$

Finally, although the total energy of an interacting many-body system is a two-particle operator, it is still possible to express it in term of the single-particle Green's function, since the Schrödinger equation links the two-particles interaction potential with the time derivative, which is a one-particle operator:

$$E = -\frac{i}{2} \int d^3\mathbf{x} \lim_{t' \rightarrow t} \lim_{\mathbf{x}' \rightarrow \mathbf{x}} \left[i \frac{\partial}{\partial t} - \frac{\nabla^2}{2} \right] G_{\alpha\alpha}(\mathbf{x}t, \mathbf{x}'t') . \quad (2.46)$$

Eq. 2.46 is the Galitskii-Migdal formula, and can be used to correct the total energy from DFT once the Green's function is calculated. It is useful and instructive to calculate the single particle Green's function for a system of non-interacting fermions, as this quantity will be at the basis of the perturbation theory introduced in the next sections. The Hamiltonian of a system of non-interacting fermions can be always written as

$$\hat{H}_0 = \sum_i \varepsilon_i \hat{c}_i^\dagger \hat{c}_i , \quad (2.47)$$

where i labels the eigenstates of the Hamiltonian. In periodic systems with spin collinear magnetism, the eigenstates are labelled by their momentum \mathbf{k} , band index n , and spin α , therefore

$$\hat{H}_0 = \sum_{n\mathbf{k}\alpha} \varepsilon_{n\mathbf{k}\alpha} \hat{c}_{n\mathbf{k}\alpha}^\dagger \hat{c}_{n\mathbf{k}\alpha} , \quad (2.48)$$

with

$$\hat{c}_{n\mathbf{k}\alpha} = \int d^3\mathbf{x} \phi_{n\mathbf{k}\alpha}(\mathbf{x}) \hat{\psi}_\alpha(\mathbf{x}) , \quad (2.49)$$

where $\phi_{n\mathbf{k}\alpha}(\mathbf{x})$ is an eigenstate of the non-interacting Hamiltonian. In this non-interacting problem, the Heisenberg picture expression of $\hat{c}_{n\mathbf{k}\alpha}$ is analytic and coincides with the interaction picture

$$\hat{c}_{n\mathbf{k}\alpha, H}(t) = \hat{c}_{n\mathbf{k}\alpha, I}(t) = e^{-i\varepsilon_{n\mathbf{k}\alpha} t} \hat{c}_{n\mathbf{k}\alpha} . \quad (2.50)$$

Substituting Eqs. 2.49 and 2.50 in 2.41 and using the definition 2.43, we obtain

$$iG_{\alpha\beta}(\mathbf{x}t, \mathbf{x}'t') = \sum_{n\mathbf{k}\alpha} \sum_{m\mathbf{q}\beta} \phi_{n\mathbf{k}\alpha}(\mathbf{x}) \phi_{m\mathbf{q}\beta}^*(\mathbf{x}') e^{-i\varepsilon_{n\mathbf{k}\alpha}t} e^{i\varepsilon_{m\mathbf{q}\beta}t'} \quad (2.51)$$

$$\left[\theta(t-t') \langle \hat{c}_{n\mathbf{k}\alpha} \hat{c}_{m\mathbf{q}\beta}^\dagger \rangle - \theta(t'-t) \langle \hat{c}_{m\mathbf{q}\beta}^\dagger \hat{c}_{n\mathbf{k}\alpha} \rangle \right], \quad (2.52)$$

where the shorthand $\langle \dots \rangle$ indicates the bracket with the ground state. Since

$$\langle \hat{c}_{n\mathbf{k}\alpha} \hat{c}_{m\mathbf{q}\beta}^\dagger \rangle = \delta_{\alpha\beta} \delta_{nm} \delta(\mathbf{k}-\mathbf{q}) \theta(\varepsilon_{n\mathbf{k}\alpha} - \varepsilon_F), \quad (2.53)$$

$$\langle \hat{c}_{m\mathbf{q}\beta}^\dagger \hat{c}_{n\mathbf{k}\alpha} \rangle = \delta_{\alpha\beta} \delta_{nm} \delta(\mathbf{k}-\mathbf{q}) \theta(\varepsilon_F - \varepsilon_{n\mathbf{k}\alpha}), \quad (2.54)$$

which come from the fact that creating (destroying) a fermion in an already filled (empty) orbital annihilates the state, the expression for the Green's function can be further simplified, leading to

$$iG_{\alpha\beta}(\mathbf{x}t, \mathbf{x}'t') = \sum_{n\mathbf{k}\alpha} \delta_{\alpha\beta} \phi_{n\mathbf{k}\alpha}(\mathbf{x}) \phi_{n\mathbf{k}\alpha}^*(\mathbf{x}') e^{-i\varepsilon_{n\mathbf{k}\alpha}(t-t')} \quad (2.55)$$

$$\left[\theta(t-t') \theta(\varepsilon_{n\mathbf{k}\alpha} - \varepsilon_F) - \theta(t'-t) \theta(\varepsilon_F - \varepsilon_{n\mathbf{k}\alpha}) \right]. \quad (2.56)$$

Using the definition

$$iG_{\alpha\beta}(\mathbf{x}t, \mathbf{x}'t') = \sum_{n\mathbf{k}\alpha} \phi_{n\mathbf{k}\alpha}(\mathbf{x}) \phi_{n\mathbf{k}\alpha}^*(\mathbf{x}') G_{n\mathbf{k},\alpha\beta}(t-t'), \quad (2.57)$$

and Fourier-transforming, we finally arrive to the result

$$G_{n\mathbf{k},\alpha\beta}(\omega) = \delta_{\alpha\beta} \left[\frac{\theta(\varepsilon_{n\mathbf{k}\alpha} - \varepsilon_F)}{\omega - \varepsilon_{n\mathbf{k}\alpha} + i\eta} + \frac{\theta(\varepsilon_F - \varepsilon_{n\mathbf{k}\alpha})}{\omega - \varepsilon_{n\mathbf{k}\alpha} - i\eta} \right]. \quad (2.58)$$

2.2.5 Perturbation theory for the Green's functions

The results highlighted in the previous sections allow us to write a perturbative expansion for the *interacting* Green's function. The idea behind is very simple: we are able to solve the non-interacting problems, for which we even know the analytic expression for the Green's function (Eq. 2.58), while the addition of the interaction is the source of all the troubles. It is thus convenient to treat the interaction term of the Hamiltonian as a perturbation. The perturbative expansion for the Green's function can be obtained starting from the definition of the Green's function in Eq. 2.41 and following these steps:

1. The Gell-Mann and Low theorem connects the *interacting* ground state $|\Psi_0\rangle$ to the *non-interacting* ground-state $|\Phi_0\rangle$, which can be calculated e.g. using DFT.
2. The perturbative expansion of the propagator \hat{U} in Eq. 2.38 expresses the Green's function itself as a series.

Chapter 2. Theoretical background

3. The combinatorial properties of the time-ordering operator allow simplifying the final expression (for a detailed treatment see [17]).

The final result is

$$iG(\mathbf{x}t, \mathbf{x}'t') = \sum_{v=0}^{\infty} \frac{(-1)^v}{v!} \int_{-\infty}^{\infty} dt_1 \dots \int_{-\infty}^{\infty} dt_v \frac{\langle \Phi_0 | T[\hat{H}_{1,I}(t_1) \dots \hat{H}_{1,I}(t_v) \hat{\psi}_{I,\alpha}(\mathbf{x}t) \hat{\psi}_{I,\beta}^{\dagger}(\mathbf{x}'t')] | \Phi_0 \rangle}{\langle \Phi_0 | \hat{S} | \Phi_0 \rangle}, \quad (2.59)$$

with

$$\hat{S} = \sum_{v=0}^{\infty} \frac{(-1)^v}{v!} \int_{-\infty}^{\infty} dt_1 \dots \int_{-\infty}^{\infty} dt_v T[\hat{H}_{1,I}(t_1) \dots \hat{H}_{1,I}(t_v)]. \quad (2.60)$$

These expressions are still very cumbersome. Fortunately, further simplifications turn them into a very useful tool for computational physics.

We start making three important observations. First, all the operators appearing in its r.h.s. are expressed in the interaction picture, therefore they can be easily computed by solving the non-interacting problem. Second, Eq. 2.59 is valid for any perturbing Hamiltonian \hat{H}_1 , therefore it can be used e.g. when treating electron-phonon coupling. Finally, each $\hat{H}_{1,I}(t)$ appearing in Eq. 2.59 hides an integral, since

$$\hat{H}_1 = \frac{1}{2} \int d^3\mathbf{x} d^3\mathbf{x}' \hat{\psi}_{\alpha}^{\dagger}(\mathbf{x}) \hat{\psi}_{\beta}^{\dagger}(\mathbf{x}') \nu_{\alpha\alpha'\beta\beta'}(\mathbf{x}, \mathbf{x}') \hat{\psi}_{\beta'}(\mathbf{x}') \hat{\psi}_{\alpha'}(\mathbf{x}) \quad (2.61)$$

and the time-ordering operator implies a sum over permutations, which scales factorially with the number of operators on which it acts. Therefore the number of integrals to calculate is huge since the very first perturbative orders. Luckily this number can be reduce drastically:

- by exploiting the combinatorial properties of the time ordering operators and the fact that the destruction operators annihilate the ground state, we can show that many integrals vanish. This result is known as *Wick theorem*.
- Some integrals can be mapped into others by simply switching the name of the dummy integration variables. This allows us to exploit the topological properties of the graphs, and associate each integral to a diagram. As discussed in more detail in Ref. [17], only few integrals associated to diagrams with particular topological properties need to be computed, while all the others are either vanishing or equal to the former. These *Feynman diagrams* were originally introduced by Richard Feynman to study the relativistic quantum field theory problems.

The theory illustrated until now is very general, and does not depend on the expression of the perturbing Hamiltonian. Different expressions of the perturbing Hamiltonian, however,

will lead to different *Feynman rules*, i.e. list of prescriptions to draw the Feynman diagrams and consequently write the integrals which must be solved. Here we list the rules for the ν -th term of the expansion of the single particles Green's function for an interaction with the shape expressed in Eq. 2.61:

1. Draw all the *topologically distinct* connected diagrams with ν interaction (wiggled) lines and $2\nu + 1$ oriented particle lines. For each vertex of the interaction lines there must be only one particle line incoming and one outgoing.
2. Label each vertex with a space-time point $\mathbf{x}t$.
3. Each solid line running from $\mathbf{x}'t'$ to $\mathbf{x}t$ represents a non-interacting Green's function $G_{\alpha\beta}^0(\mathbf{x}t, \mathbf{x}'t')$.
4. Each wiggled line represent an interaction $v_{\alpha\alpha'\beta\beta'}(\mathbf{x}, \mathbf{x}')\delta(t - t')$.
5. integrate over all the time-space internal variables and sum over the internal spin indices.
6. Multiply by the prefactor $(-1)^F \left(\frac{i}{\hbar}\right)^\nu$, where F is the number of fermion loops.
7. Green's functions with the same time variables ($t = t'$) must be interpreted as $G_{\alpha\beta}^0(\mathbf{x}t, \mathbf{x}'t^+)$.

This discussion can be specialized to the Coulomb potential, by taking

$$v_{\alpha\alpha'\beta\beta'}(\mathbf{x}, \mathbf{x}') = \frac{1}{|\mathbf{x} - \mathbf{x}'|} \delta_{\alpha\alpha'} \delta_{\beta\beta'} . \quad (2.62)$$

Examples of diagrams for $\nu = 1$ and $\nu = 2$ can be found in Fig. 2.1.

2.2.6 Dyson equation

In this section we exploit the topological properties of the diagrams to perform infinite sums of them. As it can be easily noted from Fig. 2.1, each diagram is characterized by two free Green's functions connecting the points $\mathbf{x}t$ and $\mathbf{x}'t'$ to the rest of the graph. This topological property allows to write the exact single particle Green's function as

$$G_{\alpha\beta}(\mathbf{x}t, \mathbf{x}'t') = G_{\alpha\beta}^0(\mathbf{x}t, \mathbf{x}'t') + \int d^3\mathbf{y} d^3\mathbf{y}' \int d\tau d\tau' G_{\alpha\mu}^0(\mathbf{x}t, \mathbf{y}\tau) \Sigma_{\mu\nu}(\mathbf{y}\tau, \mathbf{y}'\tau') G_{\nu\beta}^0(\mathbf{y}'\tau', \mathbf{x}'t') , \quad (2.63)$$

where the *improper self-energy* Σ is implicitly defined. In order to simplify the notation, we use arabic numbers to label space-time and spin indexes, e.g. $1 \equiv \{\mathbf{x}t, \alpha\}$. Furthermore, the bar sign over a number implies an integral over the space-time variable and sum over spin. With this convention Eq. 2.63 becomes

$$G^0(1, 2) = G^0(1, 2) + G^0(1, \bar{3}) \Sigma(\bar{3}, \bar{3}') G^0(\bar{3}', 2) . \quad (2.64)$$

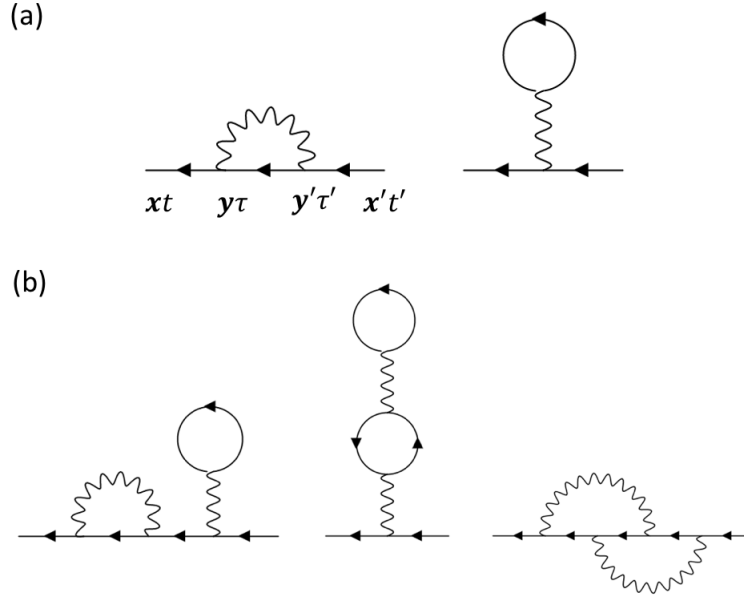


Figure 2.1: Panel (a) shows the only topologically inequivalent first order ($\nu=1$) diagrams, while panel (b) shows some examples of second order ($\nu=2$) diagrams.

The improper self-energy Σ is made up of *proper self-energy insertions* linked to each other by single particle lines. A proper self-energy insertion is a part of diagram which can not be separated into two pieces by cutting a single particle line. For example, the first diagram of Fig. 2.1b is not a proper self-energy insertion, as it can be separated into the diagrams of Fig. 2.1a by cutting the Green's function linking the two interaction lines. By definition, the proper self-energy Σ^* is the sum of all the topologically-inequivalent proper self-energy insertions, and satisfies the relation

$$\Sigma(1, \vec{3}) G_0(\vec{3}, 2) = \Sigma^*(1, \vec{3}) G(\vec{3}, 2), \quad (2.65)$$

which comes from the diagrammatic relation between Σ and Σ^* represented in Fig. 2.2, after performing a partial summation of the infinite-many diagrams in the r.h.s.

Substituting Eq. 2.65 into 2.64 we obtain the following *Dyson equation*:

$$G(1, 2) = G^0(1, 2) + G^0(1, \vec{3}) \Sigma^*(\vec{3}, \vec{3}') G(\vec{3}', 2). \quad (2.66)$$

We can thus see that the sum of infinite-many diagrams carried in Eq. 2.65 turns Eq. 2.64 into a *self-consistent equation*, where the interacting Green's function appears both at the l.h.s. and at the r.h.s..

In order to solve Eq. 2.66. we only need the knowledge of the proper self-energy Σ^* . This represents the largest reduction in term of diagrams that we can achieve. At the first order, there are only two self-energy insertions, which coincide with the diagrams shown in Fig. 2.3a. They correspond, respectively, to the Fock exchange and the Hartree repulsion between electrons. This approximation to the self-energy is equivalent to the well known Hartree-Fock method, which, however, overestimates the band-gap in semiconductors. The reason is that

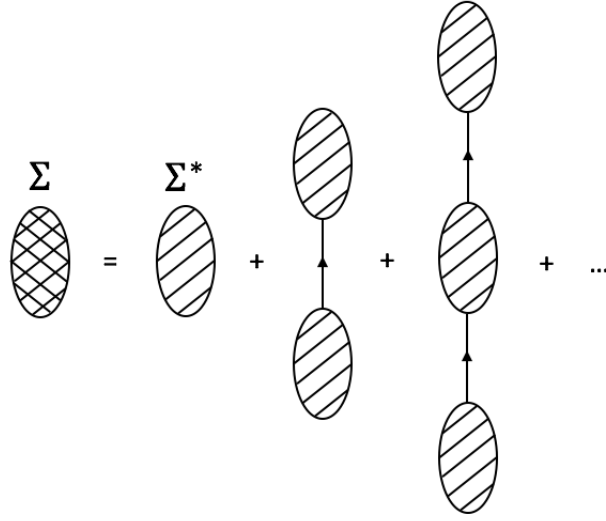


Figure 2.2: This figure shows that the improper self-energy (represented with a double-striped texture) can be expanded in a series of the proper self-energy (represented with a striped texture) and the non-interacting Green's function. This relation stems from the definition of Σ and Σ^* and the topological properties of the Feynman diagrams. By performing a partial summation of the diagrams in the r.h.s we obtain Eq. 2.65.

the Hartree-Fock method does not take into account the screening of the Coulomb interaction by the surrounding electrons.

This lack of screening is caused by the fact that we are not including enough diagrams in our expansion. In order to show this, let us first introduce the concept of *proper polarization insertion*, which is defined as a diagram that can not be separated into two pieces by cutting a single interaction line. The proper polarization P^* is defined as the sum of all the inequivalent proper polarization insertions. Following the same arguments as for the Green's function, it is possible to show that the effective interaction potential between electrons (i.e. the potential that is obtained after summing up all the polarization diagrams) is given by

$$W(1,2) = v(1,2) + v(1,\bar{3})P^*(\bar{3},\bar{3}')W(\bar{3}',2) . \quad (2.67)$$

The formal solution to this equation, reads

$$W = (I - vP^*)^{-1}v , \quad (2.68)$$

showing that the effective potential felt by the electrons is given by the ratio between the Coulomb potential v and a reducing factor represented by $I - vP^*$. This factor has thus the meaning of a generalized dielectric function, which correctly takes into account the effect of screening:

$$\varepsilon(1,2) = \delta(1,2) - v(1,\bar{3})P^*(\bar{3},2) . \quad (2.69)$$

Chapter 2. Theoretical background

Equivalently, we can write

$$\varepsilon(1, 2) = \delta(1, 2) + P(1, \bar{3}) \nu(\bar{3}, 2), \quad (2.70)$$

where P is the reducible polarization, satisfying the equation

$$P(1, 2) = P^*(1, 2) + P^*(1, \bar{3}) \nu(\bar{3}, \bar{3}') P(\bar{3}', 2). \quad (2.71)$$

When adding up all the polarization diagrams, the self-energy of Fig. 2.3a turns in that of Fig. 2.3b. This approximation to the self-energy leads to the well-known GW method, which has been very successful in describing the band-gaps of semiconductors. The DFT band-gap is corrected through the GW method in the following way. The inversion of the Dyson equation 2.66 in momentum space gives

$$G_{n\mathbf{k}\alpha}^{-1}(\omega) = G_{n\mathbf{k}\alpha}^{0-1}(\omega) + \Sigma_{n\mathbf{k}\alpha}^*(\omega). \quad (2.72)$$

Since

$$G_{n\mathbf{k}\alpha}^{0-1}(\omega) = \omega - \varepsilon_{n\mathbf{k}\alpha} \quad (2.73)$$

(the regularizing factor η can be safely put equal to zero), then

$$G_{n\mathbf{k}\alpha}^{-1}(\omega) = \omega - \varepsilon_{n\mathbf{k}\alpha} + \Sigma_{n\mathbf{k}\alpha}^*(\omega). \quad (2.74)$$

From the Lehman representation [17] we know that the poles of the Green's function correspond to the charged excitation energies. These excitation energies can be thus calculated by evaluating the zeros of the r.h.s. of Eq. 2.74:

$$\varepsilon_{n\mathbf{k}\alpha}^{GW} = \varepsilon_{n\mathbf{k}\alpha} - \Sigma_{n\mathbf{k}\alpha}^*(\varepsilon_{n\mathbf{k}\alpha}^{GW}). \quad (2.75)$$

Eq. 2.75 must be clearly solved self-consistently. The self-consistency does not only interest the eigenvalues $\varepsilon_{n\mathbf{k}\alpha}^{GW}$, but also the eigenfunctions, since the self-energy Σ^* depends itself on G . A fully self-consistent solution of Eq. 2.75 can be unaffordable for materials with a large number of atoms per cell. A commonly adopted approximation consists in neglecting the self-consistency both for the eigenfunctions and for the eigenvalues, leading to a one-shot correction of the energies. This method, called G_0W_0 has been shown to predict the band-gap of a broad category of semiconductors with very good accuracy [27].

2.2.7 Optical properties of crystals

The optical properties of materials are a consequence of the interaction of electrons and nuclei with electro-magnetic waves. In a wide range of experiments the light shined on a sample weakly perturbs the system, therefore MBPT provides the correct mathematical framework necessary to predict the optical properties.

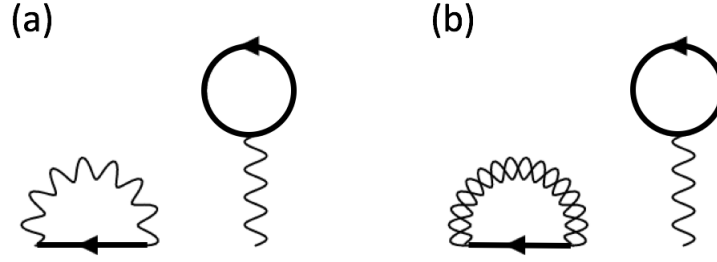


Figure 2.3: Panel (a) and (b) represent the only two topologically inequivalent diagrams for the calculation of the improper self-energy at the first order in perturbation theory. The first diagram corresponds to the Fock exchange term, while the second diagram to the Hartree repulsion between electrons. The bold oriented line represents the interacting Green's function G , and the double wiggled line corresponds to the screened interaction W . Note that in panel (b) only the interaction in the exchange term is screened, in order to avoid double counting in the sum of diagrams for the Hartree term.

The dielectric function defined in Eq. 2.69 satisfies the functional equation [25]

$$\epsilon^{-1}(1,2) = \frac{\delta V(1)}{\delta U(2)}, \quad (2.76)$$

where V is the total potential felt by the electrons inside the crystal when the perturbing potential U is applied. The total potential V is given by the sum of the perturbing potential U and the electronic screening

$$V(1) = U(1) + \langle \rho(3) \rangle v(3,1), \quad (2.77)$$

where ρ is the charge density in the material, which is related to the one-particle Green's function as expressed in Eq. 2.44. Combining this with 2.76, we obtain:

$$\epsilon^{-1}(1,2) = \frac{\delta U(1)}{\delta U(2)} - i \frac{\delta G(3,3^+)}{\delta U(2)} v(3,1). \quad (2.78)$$

Comparing Eq. 2.78 with 2.70, it is straightforward to identify

$$P(1,2) = \frac{-i \delta G(1,1^+)}{\delta U(2)}. \quad (2.79)$$

The functional derivative appearing in Eq. 2.79 can be calculated explicitly as shown in Appendix A.1, leading to

$$P(1,2) = -i[G(1,1^+)G(2,2^+) - G^{(2)}(1,2,1^+,2^+)] = -iL(1,2,1^+,2^+), \quad (2.80)$$

where the two-particle correlation functions $G^{(2)}$ and L are defined and examined in detail in the next chapter. It is now important to stress the following points:

1. Since the dielectric function ϵ expresses the response of the system to external perturba-

Chapter 2. Theoretical background

tion (Eq. 2.76), it contains all the information to determine the optical properties of the material.

2. Eqs. 2.78-2.80 provide the way to compute the dielectric function, starting from the two-particles correlation function L which admits diagrammatic expansion.

In the following, we use the theory presented above to determine the optical absorption spectrum, which is strictly related to the *macroscopic* dielectric tensor. This is defined as the response of the material to a macroscopic perturbation. In materials with cubic symmetry, in the optical limit $\mathbf{q} \rightarrow \mathbf{0}$, the macroscopic dielectric tensor is isotropic [28], therefore the whole tensor is described by one longitudinal component $\varepsilon_M(\omega)$. We can easily derive an analytic relation between $\varepsilon_M(\omega)$ and the microscopic dielectric function. A macroscopic perturbation is represented by a field varying very slowly in space, so that it can be regarded as constant over the material unit cell. Its Fourier transform can thus be approximated as

$$g_{\mathbf{G}}(\mathbf{q}, \omega) = \frac{1}{\Omega} \int d^3\mathbf{x} e^{-i(\mathbf{q}+\mathbf{G})\cdot\mathbf{x}} g(\mathbf{x}, \omega) \simeq g_0(\mathbf{q}, \omega) . \quad (2.81)$$

Therefore, we can determine $\varepsilon_M(\omega)$ by studying the response of the system to a macroscopic longitudinal potential

$$U_{\mathbf{G}}(\mathbf{q}, \omega) = U_{\mathbf{G}}(\mathbf{q}, \omega) \delta_{\mathbf{G}\mathbf{0}} \quad (2.82)$$

From Eq. 2.76, we have

$$V(1) = \varepsilon^{-1}(1, 2) U(2) , \quad (2.83)$$

which can be written in reciprocal space as

$$V_{\mathbf{G}}(\mathbf{q}, \omega) = \varepsilon_{\mathbf{G}\mathbf{G}''}^{-1}(\mathbf{q}, \omega) U_{\mathbf{G}''}(\mathbf{q}, \omega) . \quad (2.84)$$

The macroscopic components are thus

$$V_0(\mathbf{q}, \omega) = \varepsilon_{00}^{-1}(\mathbf{q}, \omega) U_0(\mathbf{q}, \omega) \equiv (\varepsilon_M(\mathbf{q}, \omega))^{-1} U_0(\mathbf{q}, \omega) \quad (2.85)$$

so that we can identify

$$\varepsilon_M(\omega) = \lim_{\mathbf{q} \rightarrow \mathbf{0}} \frac{1}{\varepsilon_{00}^{-1}(\mathbf{q}, \omega)} , \quad (2.86)$$

where the optical limit $\mathbf{q} \rightarrow \mathbf{0}$ is carried. In non-cubic materials, such as the hexagonal boron nitride which has been extensively studied in this Thesis, we can always choose a reference frame for which the macroscopic dielectric tensor is diagonal by aligning the axis along the principal directions of the tensor. Eq. 2.86 still holds for the longitudinal component $\varepsilon_{M\alpha}(\omega)$, provided that the electric field is parallel to the corresponding principal direction α .

The connection between the macroscopic dielectric tensor and the absorption coefficient can be drawn by studying the propagation of an electromagnetic wave

$$\mathbf{A}(\mathbf{r}, \omega) = \mathbf{A}_0(\omega) e^{i\mathbf{k}\cdot\mathbf{r}} \quad (2.87)$$

in a cubic crystal. The transverse induced current [28]

$$\mathbf{J}_T^{ind}(\mathbf{r}, \omega) = \frac{\omega^2}{4\pi c} (\epsilon_m(\omega) - 1) \mathbf{A}(\mathbf{r}, \omega) \quad (2.88)$$

can be directly inserted into the Maxwell equations

$$\mathbf{J}_T^{ind}(\mathbf{r}, \omega) = \left(\nabla^2 + \frac{\omega^2}{c^2} \right) \mathbf{A}(\mathbf{r}, \omega) \quad (2.89)$$

leading to the following dispersion relation

$$k^2 = \frac{\omega^2}{c^2} \epsilon_M(\omega) . \quad (2.90)$$

Conventionally, the propagation vector k is expressed in terms of the refractive index (n) and the extinction coefficient (χ),

$$\mathbf{k} = \mathbf{s} \frac{\omega}{c} (n + i\chi), \quad (2.91)$$

where \mathbf{s} is the unit vector indicating the direction of the propagation of the electromagnetic wave. We can easily note that the real part of k will cause the oscillations of \mathbf{A} , while the imaginary part will be associated to its decay in space. Such an imaginary part, called *absorption coefficient* $\alpha(\omega)$, can be easily expressed in terms of the imaginary part of $\epsilon_M(\omega)$, by combining Eq. 2.90 with Eq. 2.91:

$$\alpha(\omega) = \frac{\omega}{c} \chi = \frac{\omega}{c} \frac{\Im \epsilon_M(\omega)}{2n} . \quad (2.92)$$

Eq. 2.92 is the central result of this section, which allows us to connect the macroscopic optical properties of the materials to the microscopic mechanisms studied by MBPT.

In order to close the chain of equations 2.76-2.92, it is necessary to find an approximation for P , which usually comes from the diagrammatic expansion of Eq. 2.80. The simplest approximation for P is that of independent quasi-particles, for which

$$P(1, 2) = -i G^0(1, 2) G^0(2, 1) , \quad (2.93)$$

corresponding to the simple bubble polarization diagram. Using Eqs. 2.70 and 2.86, we finally obtain

$$\Im \epsilon_M(\omega) = \sum_K |\Pi_K|^2 \delta(\omega - \epsilon_K) , \quad (2.94)$$

where the short-hand $K = \{\mathbf{k} \nu c \alpha\}$ to label the optical transitions $\{\mathbf{k} \nu \alpha\} \rightarrow \{\mathbf{k} c \alpha\}$ has been used, and $\epsilon_K = \epsilon_{\mathbf{k} c \alpha} - \epsilon_{\mathbf{k} \nu \alpha}$. The meaning of 2.94 is straightforward: the absorption spectrum is made up of many peaks, each corresponding to the energy of the optical transition between the valence state ν and the conduction state c at the kpoint \mathbf{k} . The weight of each peak is given by the optical dipole moment Π_K , which is defined as

$$\Pi_K = \mathbf{n} \cdot \langle \psi_{\mathbf{k} c} | \mathbf{r} | \psi_{\mathbf{k} \nu} \rangle , \quad (2.95)$$

where \mathbf{n} is the polarization vector of the incoming light. Eq. 2.94 thus describes an independent-

particles picture for the optical absorption, stemming from the approximation 2.93. This picture works well only for materials with very high dielectric constants in which the excitonic effects are heavily screened, while fails dramatically for materials where the screening is weaker. The reason for this failure is related to the fact that this approximation neglects the interacting nature of the particles, thus excluding all the excitonic effects. In order to include these effects, it is necessary to enhance the level of the theory, calculating the polarizability from the two-particles correlation function L . In the next section, we introduce a diagrammatic expansion for L which gives a suitable approximation to determine the optical properties of several semiconductors.

2.2.8 Two particles Green's function

Similarly to what was done in the previous chapter, we can define a two-particle Green's function

$$G^{(2)}(\mathbf{x}_1 t_1, \mathbf{x}_2 t_2, \mathbf{x}_3 t_3, \mathbf{x}_4 t_4) = (-i)^2 \frac{\langle \Psi_0 | T[\hat{\psi}_H(\mathbf{x}_1 t_1) \hat{\psi}_H(\mathbf{x}_2 t_2) \hat{\psi}_H^\dagger(\mathbf{x}_4 t_4) \hat{\psi}_H^\dagger(\mathbf{x}_3 t_3)] | \Psi_0 \rangle}{\langle \Psi_0 | \Psi_0 \rangle}, \quad (2.96)$$

which allows to calculate the expectation values of *two-particles operators*, which is crucial in the study of the electron-hole pairs and optical properties. In particular we consider the two-particles correlation function,

$$L(1, 2, 3, 4) = G(1, 3)G(2, 4) - G^{(2)}(1, 2, 3, 4) \quad (2.97)$$

which is related to the polarizability by Eq. 2.80. Analogously to the one-particle Green's function, also the two-particles correlation function admits a diagrammatic expansion. The topology of the diagrams for L allows to write the following Dyson equation, which is known as Bethe-Salpeter equation (BSE)

$$L(1, 2, 3, 4) = L_0(1, 2, 3, 4) + L_0(1, b, 3, a) \Xi(a, b, c, d) L(d, 2, c, 4), \quad (2.98)$$

where $L_0(1, 2, 3, 4) = G_0(1, 4)G_0(2, 3)$. Here, the kernel Ξ plays the same role as the self-energy for the single particle Green's function. The perturbative expansion of Ξ at the first-order is made up of two diagrams, represented in Fig. 2.4. The one on the left corresponds to a screened Fock exchange and reads

$$\Xi^F(1, 2, 3, 4) = i\delta(1, 4)\delta(2, 3)W(1, 2), \quad (2.99)$$

while that on the right corresponds to an unscreened (to avoid double counting) Hartree interaction:

$$\Xi^H(1, 2, 3, 4) = -i\delta(1, 3)\delta(2, 4)v(1, 2). \quad (2.100)$$

The complex time structure of the BSE can be simplified by assuming that the screened

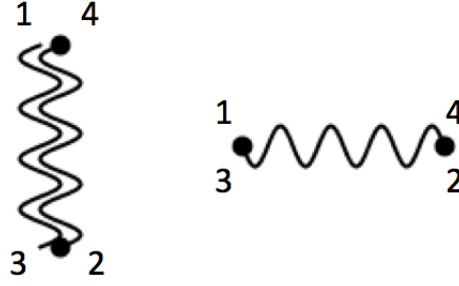


Figure 2.4: First order diagrams for Ξ . The one at left has the meaning of a screened Fock exchange, while that at the right of an unscreened Hartree interaction. The diagram at the right is unscreened to avoid double counting.

interaction of Eq. 2.99 is static:

$$W(t_1, t_2) = \delta(t_1, t_2) W. \quad (2.101)$$

Furthermore, since the final goal is to determine P from Eq. 2.80, we can set $3 = 1^+$ and $4 = 2^+$. Defining the Fourier transform of the two-times L as

$$L(1, 2, 1^+, 2^+) = \int \frac{d\omega}{2\pi} L(\omega) e^{-i\omega(t_1 - t_2)}, \quad (2.102)$$

the static BSE in the frequency domain can be written as

$$L(\mathbf{x}_{1,2,3,4}, \omega) = L_0(\mathbf{x}_{1,2,3,4}, \omega) + L_0(\mathbf{x}_{1,b,3,a}, \omega) \Xi(\mathbf{x}_{a,b,c,d}) L(\mathbf{x}_{d,2,c,4}, \omega), \quad (2.103)$$

where the short-hand $\mathbf{x}_{1,2,3,4} = \{\mathbf{x}_1, \mathbf{x}_2, \mathbf{x}_3, \mathbf{x}_4\}$ is adopted. The integrals over time variables are now replaced by products, leading to a considerable simplification of the solution of the BSE. At this point, it is convenient to express L in the transition basis:

$$L(\mathbf{x}_1, \mathbf{x}_2, \mathbf{x}_3, \mathbf{x}_4) = \sum_{n_1, \dots, n_4} L_{n_1 n_3}^{n_4 n_2} \phi_{n_1}(\mathbf{x}_1) \phi_{n_2}(\mathbf{x}_2) \phi_{n_3}^*(\mathbf{x}_3) \phi_{n_4}^*(\mathbf{x}_4), \quad (2.104)$$

where n_i labels the Kohn-Sham states. The coefficients $L_{0 n_1 n_3}^{n_4 n_2}$ can be determined analytically:

$$L_{0 n_1 n_3}^{n_4 n_2}(z) = i \frac{(f_{n_2} - f_{n_1})}{z - (\epsilon_{n_1} - \epsilon_{n_2})} \delta_{n_1, n_4} \delta_{n_2, n_3}, \quad (2.105)$$

where $z = \omega + i\eta \text{sign}(f_{n_2} - f_{n_1})$. The BSE in the transition basis reads

$$L_{n_1 n_3}^{n_4 n_2} = L_{0 n_1 n_3}^{n_4 n_2} + L_{0 n_1 n_3}^{ab} \Xi_{ab}^{cd} L_{cd}^{n_4 n_2}, \quad (2.106)$$

Chapter 2. Theoretical background

where the explicit dependence on the frequencies has been omitted. We can write the formal solution to Eq. 2.106 as:

$$L_{n_1 n_3}^{n_4 n_2} = i[H^{2p} - Iz]_{n_1 n_3}^{-1} L_{n_1 n_3}^{n_4 n_2} (f_{n_2} - f_{n_4}) . \quad (2.107)$$

In order to calculate it explicitly, it is necessary to diagonalize the two-particles effective Hamiltonian

$$H_{n_1 n_3}^{2p n_4 n_2} = (\epsilon_{n_1} - \epsilon_{n_3}) \delta_{n_1 n_4} \delta_{n_2 n_3} - i(f_{n_3} - f_{n_1}) \Xi_{n_1 n_3}^{n_4 n_2} . \quad (2.108)$$

This matrix is not Hermitian. However, if the well known Tamm-Dancoff approximation is adopted [29], then the matrix becomes Hermitian, and its eigenvalues E_λ and eigenvectors A_λ satisfy the following secular problem:

$$H_{n_1 n_3}^{2p ab} A_{ab}^\lambda = E_\lambda A_{n_1 n_3}^\lambda \quad (2.109)$$

We can finally use Eq. 2.109 to write the solution to the BSE:

$$L_{n_1 n_3}^{n_4 n_2} = i \sum_\lambda \frac{A_{n_1 n_3}^\lambda A_{n_2 n_4}^{\lambda*}}{\omega - E_\lambda + i\eta \operatorname{sgn}(f_{n_3} - f_{n_1})} (f_{n_2} - f_{n_4}) . \quad (2.110)$$

Each exciton eigenvector is associated to two momenta, bands, and spins indexes, $n_1 = \{\mathbf{k}_1 i_1 \alpha\}$ and $n_3 = \{\mathbf{k}_3 i_3 \beta\}$. However, in the optical limit, corresponding to the case in which the momentum of the incoming light is much smaller than the primitive vectors of the reciprocal space, $\mathbf{k}_1 = \mathbf{k}_2$. Furthermore, if we consider only the excitons related to spin conserving transitions (which are optically allowed), then also the spin variables are equal. We can thus express the exciton eigenvector as $A_{\mathbf{k} \nu c \alpha}^\lambda = A_K^\lambda$ (where ν and c refer to a conduction and a valence state respectively).

The resonant component of the polarizability can be calculated by combining Eq. 2.110 with Eq. 2.80, and reads

$$P_K^{K'} = \sum_\lambda \frac{A_K^\lambda A_{K'}^{\lambda*}}{\omega - E_\lambda + i\eta} . \quad (2.111)$$

Using Eqs. 2.70 and 2.86 we finally obtain

$$\Im \mathcal{E}_M(\omega) \propto \sum_\lambda |\Pi_\lambda|^2 \delta(\omega - E_\lambda) . \quad (2.112)$$

Here Π_λ is the exciton dipole moment, which is defined as

$$\Pi^\lambda = \sum_K A_K^\lambda \Pi_K . \quad (2.113)$$

Eq. 2.112 has a very similar structure to that of Eq. 2.94. The absorption spectrum is made up many of peaks, each corresponding to an exciton energy E_λ , with an intensity equal to the exciton dipole moment. The difference with Eq. 2.94 is that each exciton now corresponds to a superposition of optical transitions, reflecting the intrinsic many-body nature of the excited state.

2.3 Photoluminescence

In this chapter, we illustrate the theory of photoluminescence presented in the work of Hannewald et al. [30]. To begin with, it is very important to stress that, while absorption is an *equilibrium property* of the system, photoluminescence comes at the end of a *non-equilibrium process* (i. e. the laser excitation and the excitons dynamics), and it can be affected on the way in which the experiment is carried. The formalism required to study photoluminescence is thus that of the *nonequilibrium Green's functions* [19, 31]. In the following sections, we will briefly recap the definition of nonequilibrium Green's function and their diagrammatic expansion, and we use this formalism to derive an equation for the photoluminescence.

2.3.1 Nonequilibrium Green's functions

The nonequilibrium Green's function (NEGF) theory represents the generalization of the theory illustrated in Section 2.2, and is aimed to describe the dynamics of a system which is initially at equilibrium with the environment and is later perturbed by a time dependent potential. Being the Hamiltonian time-dependent, the evolution operator can not be expressed as $e^{-i\hat{H}t}$, but takes a shape similar to that of Eq. 2.38:

$$\hat{W}(t, t_0) = \sum_{n=0}^{\infty} \frac{(-i)^n}{n!} \int_{t_0}^t dt_1 dt_2 \dots dt_n T[\hat{H}(t_1), \dots, \hat{H}(t_n)], \quad (2.114)$$

with

$$\hat{W}(t, t_0)^\dagger = \hat{W}(t_0, t) \quad (2.115)$$

The average of an operator at the time t is thus

$$\langle \hat{O}(t) \rangle = \sum_m \frac{e^{-\beta(E_m - \mu N_m)}}{Z} \langle \Psi_m | \hat{W}(t, t_0)^\dagger \hat{O}(t) \hat{W}(t, t_0) | \Psi_m \rangle, \quad (2.116)$$

where the thermodynamic average can be expressed with the short-and:

$$\text{Tr}\{\hat{\rho} \dots\} = \sum_m \frac{e^{-\beta K_m}}{Z} \langle \Psi_m | \dots | \Psi_m \rangle, \quad (2.117)$$

with

$$\hat{K} = \hat{H} - \mu \hat{N}. \quad (2.118)$$

This leads naturally to the definition of the non-equilibrium Green's function as

$$\mathcal{G}_{\alpha\beta}(\mathbf{x}_1 t_1, \mathbf{x}_2 t_2) = -i \text{Tr} \left\{ \hat{\rho} \hat{W}(t_0, t_1) \hat{\psi}_\alpha(\mathbf{x}_1 t_1) \hat{W}(t_1, t_2) \hat{\psi}_\beta^\dagger(\mathbf{x}_2 t_2) \hat{W}(t_2, t_0) \right\}. \quad (2.119)$$

The perturbative expansion of this object is more complex than that illustrated in Sec. 2.2. However, it can be written in a similar compact form by introducing the idea of *contour*, which corresponds to the curve in the complex plane illustrated in Fig. 2.5. The vertical branch of

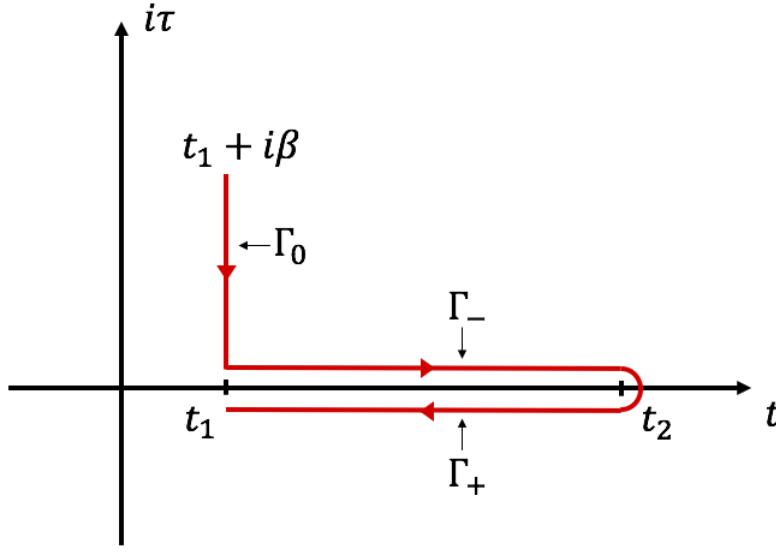


Figure 2.5: This figure shows the contour introduced in the main text. The red arrows indicate its direction. Although the branches $\Gamma_{+/-}$ are pictorially represented as shifted with respect to the real t axis, they actually do coincide with the latter.

the contour stems from the identity

$$e^{-\beta \hat{K}} = e^{-i \int_{t_0+i\beta}^{t_0} dz \hat{K}}. \quad (2.120)$$

The two horizontal branches, labeled with $(-)$ and $(+)$ stem from the fact that the perturbative expansion of the Green's function includes the integration in both the time directions. If we label z the coordinate on the contour and we define a generalized *contour-ordering operator* \mathcal{T} which arranges the operators in decreasing order of z , then the generalized Green's function on the contour

$$\mathcal{G}_{\alpha\beta}(\mathbf{x}_1 z_1, \mathbf{x}_2 z_2) = -i \text{Tr} \left\{ \hat{\rho} \hat{W}(z_0, z_1) \hat{\psi}_\alpha(\mathbf{x}_1 z_1) \hat{W}(z_1, z_2) \hat{\psi}_\beta^\dagger(\mathbf{x}_2 z_2) \hat{W}(z_2, z_0) \right\} \quad (2.121)$$

admits the following expansion

$$i \mathcal{G}_{\alpha\beta}(\mathbf{x} z, \mathbf{x}' z') = \sum_{v=0}^{\infty} \left(\frac{-i}{\hbar} \right)^v \frac{1}{v!} \int_C dz_1 \dots dz_v \langle \mathcal{T} [\hat{K}_{1,I}(z_1) \dots \hat{K}_{1,I}(z_v) \hat{\psi}_{I,\alpha}(\mathbf{x} z) \hat{\psi}_{I,\beta}^\dagger(\mathbf{x}' z')] \rangle_0 \Big|_{\text{connected}}, \quad (2.122)$$

where again only connected diagrams are considered. We can distinguish different component of the Greens' function, depending on the position on the contour its argument. Here we list

some of them:

$$\mathcal{G}(z_1, z_2) = \begin{cases} \mathcal{G}^M(z_1, z_2), & z_1, z_2 \in \Gamma_0 \\ \mathcal{G}^{>(<)}(z_1, z_2), & z_1 \in \Gamma_{+(-)}, z_2 \in \Gamma_{- (+)} \\ \mathcal{G}^T(z_1, z_2), & z_1, z_2 \in \Gamma_- \\ \mathcal{G}^{\bar{T}}(z_1, z_2), & z_1, z_2 \in \Gamma_+ \end{cases}. \quad (2.123)$$

\mathcal{G}^M is the Matsubara component, and coincides with the finite-temperature equilibrium Green's function, therefore contains information about equilibrium thermodynamic averages. $\mathcal{G}^{>(<)}$ is the greater (lesser) Green's function, while \mathcal{G}^T and $\mathcal{G}^{\bar{T}}$ are the time ordered Green's functions, and contain information about the time evolution of the system. The presence of many Green's function components, together with the need to operate on the contour, make the evaluation of the integrals in Eq. 2.123 particularly complicated. Fortunately, this task is facilitated by the Langreth rules [32], a set of identities relating the integrals of the various component of the Green's functions.

2.3.2 A NEGF theory of the photoluminescence

According to Poynting's theorem, the emitted light power per frequency and sample volume is [30]

$$I_0(\omega) = -\frac{1}{2\pi\Omega} \int d^3\mathbf{x} \langle \Delta \hat{\mathbf{j}}^\dagger(\mathbf{x}, \omega) \cdot \Delta \hat{\mathbf{E}}(\mathbf{x}, \omega) + \text{H.c.} \rangle. \quad (2.124)$$

Relating the electric field to the transverse current and playing with the Fourier transforms, Eq. 2.124 becomes

$$I_0(\omega) = \frac{\omega^2 \mu_0}{4\pi^2 c_0} \frac{1}{\Omega} \int d^3\mathbf{x}_1 d^3\mathbf{x}_2 \int dt_1 dt_2 e^{i\omega(t_1 - t_2)} \langle \Delta \hat{\mathbf{j}}^T(\mathbf{x}_2 t_2) \cdot \Delta \hat{\mathbf{j}}^T(\mathbf{x}_1 t_1) \rangle, \quad (2.125)$$

Since,

$$\hat{\mathbf{j}}(\mathbf{x}t) = \lim_{\mathbf{x}' \rightarrow \mathbf{x}} \frac{\nabla_{\mathbf{x}} - \nabla_{\mathbf{x}'}}{2i} \hat{\psi}^\dagger(\mathbf{x}' t') \hat{\psi}(\mathbf{x}t) \equiv \mathbf{\Pi} \hat{\psi}^\dagger(\mathbf{x}' t') \hat{\psi}(\mathbf{x}t) \quad (2.126)$$

then

$$\begin{aligned} \langle \Delta \hat{\mathbf{j}}^T(\mathbf{x}_2 t_2) \cdot \Delta \hat{\mathbf{j}}^T(\mathbf{x}_1 t_1) \rangle &= \mathbf{\Pi}_1^T \cdot \mathbf{\Pi}_2^T \left(\langle \mathcal{T} [\hat{\psi}(\mathbf{x}_1 z_{1-}) \hat{\psi}(\mathbf{x}_2 z_{2+}) \hat{\psi}^\dagger(\mathbf{x}'_2 z_{2+}^+) \hat{\psi}^\dagger(\mathbf{x}'_1 z_{1-}^+)] \rangle - \right. \\ &\quad \left. \langle \mathcal{T} [\hat{\psi}(\mathbf{x}_1 z_{1-}) \hat{\psi}^\dagger(\mathbf{x}'_1 z_{1-}^+)] \rangle \langle \mathcal{T} [\hat{\psi}(\mathbf{x}_2 z_{2+}) \hat{\psi}^\dagger(\mathbf{x}'_2 z_{2+}^+)] \rangle \right). \end{aligned} \quad (2.127)$$

We clarify this cumbersome notation: the sign at the subscript indicates the branch where z lies, while the sign at the superscript implies to sum/subtract to the time variable the vanishing quantity η . Therefore

- $z_{1-} = t_1$ and lies on the upper branch of the contour;
- $z_{1-}^+ = t_1 + \eta$ and lies on the upper branch of the contour;
- $z_{2+} = t_2$ and lies on the lower branch of the contour;

- $z_{2+}^+ = t_2 - \eta$ and lies on the lower branch of the contour;

therefore

$$\langle \Delta \hat{\mathbf{j}}^T(\mathbf{x}_2 t_2) \cdot \Delta \hat{\mathbf{j}}^T(\mathbf{x}_1 t_1) \rangle = \mathbf{\Pi}_1^T \cdot \mathbf{\Pi}_2^T L(\mathbf{x}_1 z_{1-}, \mathbf{x}_2 z_{2+}, \mathbf{x}'_1 z_{1-}^+, \mathbf{x}'_2 z_{2+}^+), \quad (2.128)$$

or equivalently

$$\langle \Delta \hat{\mathbf{j}}^T(\mathbf{x}_2 t_2) \cdot \Delta \hat{\mathbf{j}}^T(\mathbf{x}_1 t_1) \rangle = \mathbf{\Pi}_1^T \cdot \mathbf{\Pi}_2^T L^<(\mathbf{x}_1, \mathbf{x}_2, \mathbf{x}'_1, \mathbf{x}'_2; z_1, z_2). \quad (2.129)$$

We have thus related once again the optical properties to the (nonequilibrium) two-particles correlation function L . Unfortunately, contrary to the equilibrium case, the nonequilibrium one poses the following challenges. First of all the non-interacting Green's function is time-dependent, since the noninteracting Hamiltonian contains a perturbing one-body potential. Therefore, there is not an analytic and unique expression for \mathcal{G}_0 , but its value should be calculated case by case using numeric techniques. Furthermore, the time invariance does not hold anymore, therefore $\mathcal{G}(z_1, z_2) \neq \mathcal{G}(z_1 - z_2)$, requiring evolution in the two times variables. This approach is very expensive, and therefore only feasible for very simple systems. Another impressive challenge is represented by the fact that nonequilibrium dynamics behind the photoluminescence emission are very complicated and involve exciton-exciton and exciton-phonon scattering [33]. This complicates even more the time-dependent evolution of the Green's function. A simplification is thus needed. The scattering processes in the non-equilibrium transient lead electron and holes to thermalize, with pseudo-equilibrium occupations equal to

$$f_{n\mathbf{k}} = \frac{1}{e^{\frac{\varepsilon_{n\mathbf{k}} - \mu_{el}}{k_B T}} + 1}, \quad \bar{f}_{n\mathbf{k}} = \frac{1}{e^{-\frac{\varepsilon_{n\mathbf{k}} - \mu_{ho}}{k_B T}} + 1} \quad (2.130)$$

for electrons and holes respectively. Here $\varepsilon_{n\mathbf{k}}$ is the quasiparticle energy of the state $\{n\mathbf{k}\}$ and μ_{el} (μ_{ho}) the chemical potential for electrons (holes). We can thus assume that the system enters a *quasistationary regime*, with the time invariance restored. Under these conditions, $L^<$ can be calculated starting from the equilibrium BSE [34], with the caveat for which electron and hole occupations are now *fractional*, and a symmetrization is required in order to ensure its pseudo-Hermiticity [35]. Following the procedure reported in [36], the luminescence can be eventually written as

$$I_0(\omega) \propto \sum_{\lambda} |\Pi_{\lambda}^2| f_{\lambda}^< \delta(\omega - E_{\lambda}), \quad (2.131)$$

showing an expression very similar to that for the absorption (Eq. 2.112) with the appearance of an additional factor, the *exciton population*

$$f_{\lambda}^< = \sum_K |A_K^{\lambda}|^2 f_K^<, \quad (2.132)$$

with

$$f_K^< = f_{\mathbf{k}c} \bar{f}_{\mathbf{k}v}. \quad (2.133)$$

The physical meaning of this term is straightforward. In an independent-particle framework, we can have emission only if there are electrons in the conduction state and holes in

the valence state, i.e. only if $f_K^< \neq 0$. The higher the population in terms of electrons and holes, the higher the amount of charge that decays with the emission of light, and consequently the intensity of the luminescence. When moving to an interacting-particle picture, the population-contribution of an exciton to the photoluminescence is proportional to the sum of the population-contribution of each transition, weighted by the exciton component $|A_K^\lambda|^2$ for that transition.

2.4 Phonons

In the former sections we illustrated the effort to find a solution to the electronic problem. We now address the nuclear one. This is, in principle, as general as the former, thus requiring very complicated solution methods. Luckily, this problem is greatly simplified by the so called *Harmonic approximation*, which works very well to predict the vibrational properties of the majority of solids. Under such approximation, the solution to the nuclear problem becomes analytic, showing that the motion of nuclei in a crystal is quantized. The quanta of vibration are called *phonons*.

2.4.1 Diagonalization of the harmonic Hamiltonian

Within the Born-Oppenheimer approximation, the Schrödinger equation for the nuclei is expressed by Eq. 2.5. The sum of the terms $V_{ion-ion}(\mathbf{R})$ and $E_n(\mathbf{R})$ describes the potential energy surface (PES), which depends on the electronic state E_n and is thus material-dependent, not allowing a solution holding for all the systems. In crystals, however, when the temperature is much lower than the melting point, the nuclei make very small oscillations around their equilibrium positions \mathbf{R}_0 , for which the free energy is minimum. This allows to approximate the PES with a multivariate parabola, thus leading to an analytic treatment of the eigenvalue problem which holds for *all* the crystals. We start expressing the coordinate $R_\alpha(\mathbf{l}b)$ of the atom at the position b in the unit cell identified by the vector \mathbf{l} (with α the cartesian component) as a function of its displacement $u_\alpha(\mathbf{l}b)$ from its equilibrium position $R_{0\alpha}(\mathbf{l}b)$,

$$R_\alpha(\mathbf{l}b) = R_{0\alpha}(\mathbf{l}b) + u_\alpha(\mathbf{l}b) . \quad (2.134)$$

We can then expand the PES, $U(\mathbf{R})$, at the second order in the atomic displacements:

$$\begin{aligned} U(\mathbf{R}) = U(\mathbf{R}_0) + \sum_{\mathbf{l}b\alpha} \frac{\partial U}{\partial u_\alpha(\mathbf{l}b)}(\mathbf{R}_0) u_\alpha(\mathbf{l}b) + \\ + \frac{1}{2} \sum_{\mathbf{l}b\alpha\mathbf{l}'b'\beta} \frac{\partial^2 U}{\partial u_\alpha(\mathbf{l}b)\partial u_\beta(\mathbf{l}'b')}(\mathbf{R}_0) u_\alpha(\mathbf{l}b) u_\beta(\mathbf{l}'b') + o(u^3). \end{aligned} \quad (2.135)$$

In order to simplify the notation, the so-called *interatomic force constants matrix* ϕ is introduced:

$$\Phi_{\alpha\beta}(\mathbf{l}b, \mathbf{l}'b') = \frac{\partial^2 U}{\partial u_\alpha(\mathbf{l}b)\partial u_\beta(\mathbf{l}'b')}(\mathbf{R}_0) . \quad (2.136)$$

Chapter 2. Theoretical background

The translational invariance of the systems guarantees that

$$\Phi_{\alpha\beta}(\mathbf{l}b, \mathbf{l}'b') = \Phi_{\alpha\beta}(\mathbf{0}b, \mathbf{l}' - \mathbf{l}b') \quad (2.137)$$

The 0-th and 1-st order terms in Eq. 2.135 can be dropped, because the potential energy is defined up to a constant and the first derivatives of the PES with respect to atomic displacements vanish at equilibrium. The harmonic Hamiltonian of the crystal is thus

$$\hat{H} = \sum_{\mathbf{l}b} \frac{\hat{p}^2(\mathbf{l}b)}{2m_b} + \frac{1}{2} \sum_{\mathbf{l}b\mathbf{l}'b'} \Phi_{\alpha\beta}(\mathbf{l}b, \mathbf{l}'b') \hat{u}_{\alpha}(\mathbf{l}b) \hat{u}_{\beta}^{\dagger}(\mathbf{l}'b'). \quad (2.138)$$

This Hamiltonian must be diagonalized imposing periodic boundary conditions on a supercell which is obtained by repeating the crystal unit cell N_1 , N_2 and N_3 times along the primitive vectors \mathbf{a}_1 , \mathbf{a}_2 , \mathbf{a}_3 . Then, the thermodynamic limit is achieved by letting $N = N_1 N_2 N_3$ tend to infinity. The periodicity of the system allows to expand the momenta and the displacements in Fourier series:

$$\hat{u}_{\alpha}(\mathbf{l}b) = \frac{1}{\sqrt{N}} \sum_{\mathbf{q}} \hat{X}_{\alpha}(\mathbf{q}b) e^{i\mathbf{q} \cdot \mathbf{R}_{\mathbf{l}}}, \quad (2.139)$$

$$\hat{p}_{\alpha}(\mathbf{l}b) = \frac{1}{\sqrt{N}} \sum_{\mathbf{q}} \hat{P}_{\alpha}(\mathbf{q}b) e^{-i\mathbf{q} \cdot \mathbf{R}_{\mathbf{l}}}. \quad (2.140)$$

With this transformation the Hamiltonian becomes:

$$\hat{H} = \sum_{\mathbf{q}b\alpha} \frac{\hat{P}_{\alpha}(\mathbf{q}b) \hat{P}_{\alpha}^{\dagger}(\mathbf{q}b)}{2m_b} + \frac{1}{2} \sum_{\mathbf{q}b\mathbf{b}'\alpha\beta} D_{b\alpha b'\beta}(\mathbf{q}) \hat{X}_{\alpha}(\mathbf{q}b) \hat{X}_{\beta}^{\dagger}(\mathbf{q}b'), \quad (2.141)$$

where

$$D_{b\alpha b'\beta}(\mathbf{q}) = \sum_{\mathbf{l}'} \Phi_{\alpha\beta}(\mathbf{0}b, \mathbf{l}'b') e^{-i\mathbf{q} \cdot \mathbf{R}_{\mathbf{l}'}} \quad (2.142)$$

is the dynamical matrix. The dynamical matrix is diagonalized at each \mathbf{q} -point.:

$$\sum_{b'\beta} \frac{1}{\sqrt{m_b m_{b'}}} D_{b\alpha b'\beta}(\mathbf{q}) \xi_{b'\beta}(\mathbf{q}v) = \omega_{\mathbf{q}v}^2 \xi_{b\alpha}(\mathbf{q}v). \quad (2.143)$$

The eigenvalue $\omega_{\mathbf{q}v}$ are the *phonon frequencies* because they correspond to the frequency of vibration of the atoms around the equilibrium position when the phonon of momentum \mathbf{q} and branch v is propagated. The *phonon eigenvector* $\xi(\mathbf{q}v)$, instead, indicates the direction of displacement of the atoms due to the phonon. We now introduce the phonon creation and destruction operators, respectively $a_{\mathbf{q}v}$ and $a_{\mathbf{q}v}^{\dagger}$:

$$\hat{X}_{\alpha}(\mathbf{q}b) = \sum_v \sqrt{\frac{\hbar}{2m_b \omega_{\mathbf{q}v}}} \xi_{b\alpha}(\mathbf{q}v) (\hat{a}_{\mathbf{q}v}^{\dagger} + \hat{a}_{-\mathbf{q}v}), \quad (2.144)$$

$$\hat{P}_\alpha(\bar{q}b) = -i \sum_{\mathbf{v}} \sqrt{\frac{\hbar m_b \omega_{\mathbf{qv}}}{2}} \xi_{b\alpha}^*(\mathbf{qv}) (\hat{a}_{\mathbf{qv}} - \hat{a}_{-\mathbf{qv}}^\dagger),$$

whose action is consists in destroying and creating a phonon. Using these operators, the Hamiltonian becomes

$$\hat{H} = \sum_{\mathbf{qv}} \hbar \omega_{\mathbf{qv}} \left(\frac{1}{2} + \hat{a}_{\mathbf{qv}}^\dagger \hat{a}_{\mathbf{qv}} \right), \quad (2.145)$$

which is a sum of harmonic oscillators, each of which corresponds to a phonon mode. The annihilation and creation operators satisfy the following commutation relations

$$\left[\hat{a}_{\mathbf{qv}}, \hat{a}_{\mathbf{q}'\mathbf{v}'}^\dagger \right] = \delta_{\mathbf{vv}'} \delta(\mathbf{q} - \mathbf{q}'), \quad (2.146)$$

therefore phonons follow a Bose-Einstein statistics:

$$n_{\mathbf{q},\mathbf{v}} = \frac{1}{e^{\frac{\omega_{\mathbf{qv}} \hbar}{k_B T}} - 1}. \quad (2.147)$$

Using Eqs. 2.139 and 2.144, the displacement of the atoms induced by phonons is simply calculated:

$$\hat{u}_{\mathbf{l}b,\alpha} = \frac{1}{\sqrt{N m_b}} \sum_{\mathbf{qv}} \hat{Q}_{\mathbf{qv}} \xi_{b\alpha}(\mathbf{qv}) e^{i\mathbf{q} \cdot \mathbf{R}_\mathbf{l}}, \quad (2.148)$$

with

$$\hat{Q}_{\mathbf{qv}} = \sqrt{\frac{\hbar}{2\omega_{\mathbf{qv}}}} (\hat{a}_{\mathbf{qv}} + \hat{a}_{-\mathbf{qv}}^\dagger). \quad (2.149)$$

2.4.2 Electron-phonon coupling

In the Born-Oppenheimer approximation, the electrons feel the potential of the ions which are frozen at the equilibrium position. In reality, the ions are not frozen, but oscillate around the bottom of the PES, generated by the repulsion with the other ions and the attraction with the electron charge density. This oscillation induces a change in the potential which is felt by electrons, leading to a coupling between the ions and electrons motion, which is described by the following Hamiltonian (at first order in ions displacement):

$$\hat{H}_{el-ph} = \sum_{j,\mathbf{l},b} \frac{\partial \hat{V}_{KS}}{\partial u_{\mathbf{l}b,\alpha}}(\mathbf{r}_j, \mathbf{R}_0) \hat{u}_{\alpha}(\mathbf{l}b). \quad (2.150)$$

Inserting Eq. 2.148 into 2.150 the first equation, we obtain

$$\hat{H}_{el-ph} = \sum_{j,\mathbf{l},b} \sum_{\mathbf{qv}} \frac{1}{\sqrt{N m_b}} \hat{Q}_{\mathbf{qv}} \xi_{b\alpha}(\mathbf{qv}) e^{i\mathbf{q} \cdot \mathbf{R}_\mathbf{l}} \frac{\partial \hat{V}_{KS}}{\partial u_{\mathbf{l}b,\alpha}}(\mathbf{r}_j, \mathbf{R}) \quad (2.151)$$

Chapter 2. Theoretical background

The second-quantized form is

$$\hat{H}_{el-ph} = \sum_{\mathbf{k}\mathbf{k}'} \sum_{ij} \sum_{\mathbf{l},b} \frac{1}{\sqrt{Nm_b}} \hat{Q}_{\mathbf{q}\nu} \xi_{b,\alpha}(\mathbf{q}\nu) e^{i\mathbf{q}\cdot\mathbf{R}_\mathbf{l}} \int d^3\mathbf{r} \psi_{\mathbf{k}'i}^*(\mathbf{r}) \frac{\partial V_{KS}}{\partial u_{\mathbf{l}b,\alpha}}(\mathbf{r}, \mathbf{R}) \psi_{\mathbf{k}j}(\mathbf{r}) \hat{c}_{\mathbf{k}'i}^\dagger \hat{c}_{\mathbf{k}j} \quad (2.152)$$

Using the identity

$$\psi_{\mathbf{k}j}(\mathbf{r} - \mathbf{R}_\mathbf{l}) = \psi_{\mathbf{k}j}(\mathbf{r}) e^{-i\mathbf{k}\cdot\mathbf{R}_\mathbf{l}} \quad (2.153)$$

the integral can be written as

$$e^{-i\mathbf{k}'\cdot\mathbf{R}_\mathbf{l}} e^{i\mathbf{k}\cdot\mathbf{R}_\mathbf{l}} \int d^3\mathbf{r} \psi_{\mathbf{k}'i}^*(\mathbf{r} - \mathbf{R}_{\mathbf{l}b}) \frac{\partial V_{KS}}{\partial u_{\mathbf{l}b,\alpha}}(\mathbf{r}, \mathbf{R}) \psi_{\mathbf{k}j}(\mathbf{r} - \mathbf{R}_{\mathbf{l}b}) . \quad (2.154)$$

Thanks to the translations invariance, the new integral is equal to the integral where $\mathbf{l} = \mathbf{0}$, and thus does not depend on \mathbf{l} :

$$e^{-i\mathbf{k}'\cdot\mathbf{R}_\mathbf{l}} e^{i\mathbf{k}\cdot\mathbf{R}_\mathbf{l}} \int d^3\mathbf{r} \psi_{\mathbf{k}'i}^*(\mathbf{r}) \frac{\partial V_{KS}}{\partial u_{\mathbf{0}b,\alpha}}(\mathbf{r}, \mathbf{R}) \psi_{\mathbf{k}j}(\mathbf{r}) \quad (2.155)$$

This allows to carry out explicitly the sum over \mathbf{l} , leading to

$$\sum_{\mathbf{l}} e^{i(\mathbf{k}+\mathbf{q}-\mathbf{k}')\cdot\mathbf{R}_\mathbf{l}} = N\delta_{\mathbf{k}',\mathbf{k}+\mathbf{q}} . \quad (2.156)$$

We thus end up with

$$\hat{H}_{el-ph} = \sum_{\mathbf{k}i} \sum_{j\mathbf{b}\mathbf{q}\nu} \sqrt{\frac{N}{m_b}} \hat{Q}_{\mathbf{q}\nu} \xi_{b,\alpha}(\mathbf{q}\nu) \langle \psi_{\mathbf{k}+\mathbf{q}i} | \frac{\partial V_{KS}}{\partial u_{\mathbf{0}b,\alpha}} | \psi_{\mathbf{k}j} \rangle \hat{c}_{\mathbf{k}+\mathbf{q}i}^\dagger \hat{c}_{\mathbf{k}j} \quad (2.157)$$

by expressing

$$\hat{Q}_{\mathbf{q}\nu} = \sqrt{\frac{\hbar}{2\omega_{\mathbf{q}\nu}}} \hat{A}_{\mathbf{q}\nu} = \sqrt{\frac{\hbar}{2\omega_{\mathbf{q}\nu}}} (\hat{a}_{\mathbf{q}\nu} + \hat{a}_{-\mathbf{q}\nu}^\dagger) \quad (2.158)$$

we finally have

$$\hat{H}_{el-ph} = \sum_{\mathbf{k}i} \sum_{j\mathbf{b}\mathbf{q}\nu} \sqrt{\frac{N\hbar}{2m_b\omega_{\mathbf{q}\nu}}} \xi_{b,\alpha}(\mathbf{q}\nu) \langle \psi_{\mathbf{k}+\mathbf{q}i} | \frac{\partial V_{KS}}{\partial u_{\mathbf{0}b,\alpha}} | \psi_{\mathbf{k}j} \rangle \hat{c}_{\mathbf{k}+\mathbf{q}i}^\dagger \hat{c}_{\mathbf{k}j} \hat{A}_{\mathbf{q}\nu} \quad (2.159)$$

leading to the definition

$$g_{\mathbf{k}+\mathbf{q}i,\mathbf{k}j}^{\mathbf{q}\nu} = \sum_b \sqrt{\frac{N\hbar}{2m_b\omega_{\mathbf{q}\nu}}} \xi_{b,\alpha}(\mathbf{q}\nu) \langle \psi_{\mathbf{k}+\mathbf{q}i} | \frac{\partial V_{KS}}{\partial u_{\mathbf{0}b,\alpha}} | \psi_{\mathbf{k}j} \rangle . \quad (2.160)$$

These are the so-called electron-phonon (EP) matrix elements. The final expression of the EP Hamiltonian is thus

$$\hat{H}_{el-ph} = \sum_{\mathbf{k}i} \sum_{j\mathbf{q}\nu} g_{\mathbf{k}+\mathbf{q}i,\mathbf{k}j}^{\mathbf{q}\nu} \hat{c}_{\mathbf{k}+\mathbf{q}i}^\dagger \hat{c}_{\mathbf{k}j} \hat{A}_{\mathbf{q}\nu} . \quad (2.161)$$

3 Quantum computing

The impossibility to find an exact solution to the Many-Body problem presented in the last chapter is due to the exponential scaling of the size of the Hilbert space with respect to the number of particles. The limited resources of the *classic computers* have pushed the development of the approximate techniques described in Chap. 2. In this chapter, instead, we present a different paradigm of calculation, known as *quantum computing*, which exploits the peculiar principles of the quantum world in order to achieve advantage over the classic computers in the solution of certain categories of problems. In particular, by virtue of their own nature, quantum computers are expected to perform especially well for the quantum physics problem. In the following, we introduce the basic concepts of quantum computing, starting from the definition of qubits and quantum circuits. We then illustrate the functioning of two hardware technologies, the superconducting qubits, which are currently implemented in the IBM Quantum processors used in this Thesis, and the defect centers in solids, whose optical properties are studied from first principles in Chap. 4.

3.1 Quantum software

A quantum bit or *qubit* is a two-level system obeying the laws of quantum mechanics. Thanks to the quantum superposition principle, its state can be in any combination of the two levels, expressed by the vectors $|0\rangle$ and $|1\rangle$ of the two-dimensional Hilbert space \mathbb{H}^2 :

$$|\psi\rangle = \alpha |0\rangle + \beta |1\rangle, \quad \alpha, \beta \in \mathbb{C}, \quad \alpha^2 + \beta^2 = 1. \quad (3.1)$$

This marks a fundamental difference with the classic bits, which can be in only one of the two levels per time, and opens to a new paradigm of calculation which promises to overcome the limitation of the classic computers.

The normalization condition $\alpha^2 + \beta^2$ of the coefficients in Eq. 3.1 can be imposed by adopting the following parametrization,

$$|\psi\rangle = e^{i\gamma} \left(\cos\left(\frac{\theta}{2}\right) |0\rangle + \sin\left(\frac{\theta}{2}\right) e^{i\phi} |1\rangle \right). \quad (3.2)$$

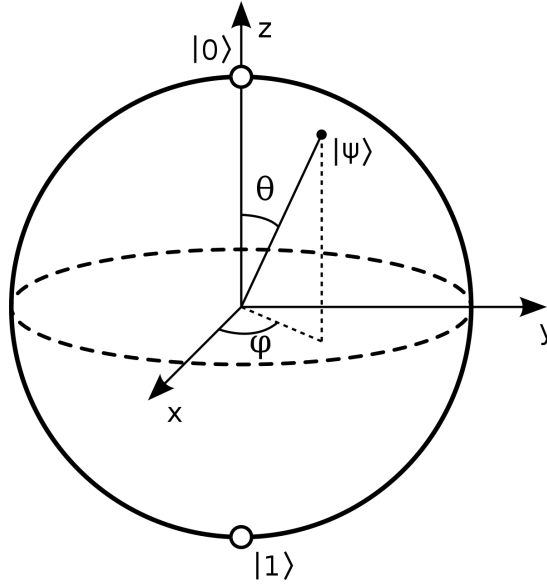


Figure 3.1: The figure shows the Bloch sphere. Any point on its surface corresponds to one possible qubit state. Particularly, the north and south pole correspond to the pure states $|0\rangle$ and $|1\rangle$ respectively.

Since the global phase γ is redundant for the description of a quantum state, the final state can be expressed as

$$|\psi\rangle = \cos\left(\frac{\theta}{2}\right)|0\rangle + \sin\left(\frac{\theta}{2}\right)e^{i\phi}|1\rangle, \quad \theta, \phi \in [0, 2\pi]. \quad (3.3)$$

Eq. 3.3 allows to represent the state of a qubit as a point on the so-called Bloch Sphere in Fig. 3.1. This is particularly useful to understand the operations that can be performed on the qubit state, which will be introduced in Sec. 3.1.1. When N qubits are entangled, their state is described by the superposition of 2^N states spanning the Hilbert space \mathbb{H}^N :

$$|\psi\rangle = \sum_{i_1, i_2, \dots, i_N=0,1} \alpha_{i_1, i_2, \dots, i_N} |i_1 i_2, \dots, i_N\rangle \quad (3.4)$$

where the coefficients α are normalized:

$$\sum_{i_1, i_2, \dots, i_N=0,1} |\alpha_{i_1, i_2, \dots, i_N}|^2 = 1. \quad (3.5)$$

We can now better appreciate the power of the quantum superposition: a system of N qubit can be in 2^N states at the same time. Imagine that each of these states corresponds to the possible solutions to a problem under exam. The quantum computer can process *all* the solutions in one shot, including thus the true solution. This phenomenon is called *quantum parallelism*. However, although the quantum computer can process all the 2^N possibilities in one shot, only one state is read during the measurement. Therefore the good quantum algorithm is the one that, after exploiting the parallelism, projects the state of the

qubits onto the solution to the problem.

3.1.1 Quantum circuits

The quantum computing operations are performed by evolving the qubit quantum state. The general evolution of a N-qubit state can be represented by a unitary operator acting on \mathbb{H}^N . Of course, for technological reasons, such general unitary operation can not be realized practically. It is thus necessary to break it into modular operations, involving mainly one and two qubits, which are called *quantum gates*. The sequence of quantum gates applied on the qubits is the *quantum circuit*. It is usually represented as a set of horizontal lines, each of which corresponds to a qubit. The gates are drawn on the line corresponding to the qubit on which they act, from left to right in chronological order (see for example Fig. 6.7).

We will now present some of the one-qubit gates which are relevant for the rest of the work.

1. The *Pauli* gates

$$X = \begin{pmatrix} 0 & 1 \\ 1 & 0 \end{pmatrix} \quad Y = \begin{pmatrix} 0 & -i \\ i & 0 \end{pmatrix} \quad Z = \begin{pmatrix} 1 & 0 \\ 0 & -1 \end{pmatrix} \quad (3.6)$$

are among the most used one-qubit gates. Particularly, the X gate is also called NOT, as it switches the state of a qubit:

$$X|0\rangle = |1\rangle \quad X|1\rangle = |0\rangle . \quad (3.7)$$

2. The exponentiation of the Pauli gates defines the *rotations*,

$$R_x(\theta) = e^{-iX\frac{\theta}{2}}, \quad R_y(\theta) = e^{-iY\frac{\theta}{2}}, \quad R_z(\theta) = e^{-iZ\frac{\theta}{2}}, \quad \theta = [0, 2\pi] \quad (3.8)$$

which are so-called because their action corresponds to the rotation on the Bloch Sphere of the state of the qubit. The rotation about the unit vector $\hat{\mathbf{n}}$ is described by

$$R_{\hat{\mathbf{n}}}(\theta) = e^{-i\frac{\theta}{2}\hat{\mathbf{n}}\cdot\boldsymbol{\sigma}} = \cos\left(\frac{\theta}{2}\right)I - i\sin\left(\frac{\theta}{2}\right)\hat{\mathbf{n}}\cdot\boldsymbol{\sigma} \quad (3.9)$$

with $\boldsymbol{\sigma} = (X, Y, Z)$.

3. Particularly important for the quantum information theory are rotations

$$S = R_z\left(\frac{\pi}{2}\right), \quad (3.10)$$

and

$$T = R_z\left(\frac{\pi}{4}\right), \quad (3.11)$$

as it will be clearer when talking about universal gates set.

4. The *Hadamard* gate

$$H = \frac{1}{\sqrt{2}} \begin{pmatrix} 1 & 1 \\ 1 & -1 \end{pmatrix} \quad (3.12)$$

can be used to create uniform superposition:

$$H|0\rangle = \frac{|0\rangle + |1\rangle}{\sqrt{2}}, \quad H|1\rangle = \frac{|0\rangle - |1\rangle}{\sqrt{2}}. \quad (3.13)$$

5. The *phase* gate

$$P(\phi) = \begin{pmatrix} 1 & 0 \\ 0 & e^{i\phi} \end{pmatrix}, \quad (3.14)$$

multiplies $|1\rangle$ by a phase $e^{i\phi}$ and leaves $|0\rangle$ unchanged.

The generic one-qubit gate could be obtained *exactly* as

$$U = e^{i\alpha} R_z(\beta) R_y(\gamma) R_z(\delta). \quad (3.15)$$

At the same time, a generic one-qubit gate can be approximated with an arbitrary accuracy ε using combinations of the only T and H. The idea of *approximating* a quantum gate is formalized by the definition of the *error* with which the gate V approximates the gate U:

$$E(U, V) = \max_{|\psi\rangle} \|(U - V)|\psi\rangle\|. \quad (3.16)$$

This definition of error ensures that:

1. if $E(U, V)$ is small, then the measure outcomes of $U|\psi\rangle$ and $V|\psi\rangle$ occur with similar probability. This can be proved using the notion of measurement introduced in the next section;
2. if we approximate a sequence of gates $U_1 U_2 \dots U_m$ with $V_1 V_2 \dots V_m$, then the errors add at most linearly, as

$$E(U_m U_{m-1} \dots U_1, V_m V_{m-1} \dots V_1) < \sum_{j=1}^m E(U_j, V_j). \quad (3.17)$$

The single-qubit gates alone do not allow to achieve any advantage with respect to classic computers. The reason is that the single-qubit gates evolve the state of the qubit on which they act independently from that of the other qubits. In other words, they do not create *entanglement*, and the system remains trivial on a quantum information point of view. The action of two-qubit gates is therefore necessary to create *correlation* between the qubit states. The two-qubit gates relevant for our work are:

1. The *controlled NOT*

$$\text{CNOT} = |0\rangle\langle 0| \otimes I + |1\rangle\langle 1| \otimes X. \quad (3.18)$$

This gate swaps the state of the target qubit (the one at right in this example) if that of the control qubit (the one at left in this example) is $|1\rangle$. Its matrix form is thus

$$\text{CNOT} = \begin{pmatrix} 1 & 0 & 0 & 0 \\ 0 & 1 & 0 & 0 \\ 0 & 0 & 0 & 1 \\ 0 & 0 & 1 & 0 \end{pmatrix}, \quad (3.19)$$

acting on the vector state

$$\begin{pmatrix} |00\rangle \\ |01\rangle \\ |10\rangle \\ |11\rangle \end{pmatrix} = \{|0\rangle, |1\rangle\} \otimes \{|0\rangle, |1\rangle\}. \quad (3.20)$$

As anticipated above, this gate creates entanglement between qubits. As a proof, we can see that the action of the CNOT on the $H|00\rangle$ qubit states gives

$$\text{CNOT} \cdot H|00\rangle = \frac{|00\rangle + |11\rangle}{\sqrt{2}} = \Phi_+, \quad (3.21)$$

which is a maximally entangled Bell state.

2. Finally the *swap* gate exchanges the state of two qubits, with matrix

$$\begin{pmatrix} 1 & 0 & 0 & 0 \\ 0 & 0 & 1 & 0 \\ 0 & 1 & 0 & 1 \\ 0 & 0 & 0 & 1 \end{pmatrix}. \quad (3.22)$$

As anticipated above, although we would need to implement a general N-qubit unitary operation, we can just rely on a finite set of qubit gates for technological reasons. The question arising spontaneously is thus: are we able to express any N-qubit operation using a fine set of quantum gates? To be more rigorous, a set of gates is said to be *universal for quantum computation* if any unitary N-qubit operation can be approximated with arbitrary accuracy by a combination of those gates. It can be proven that such a universal set of gates exists:

$$\mathcal{G}_1 = \{H, S, T, \text{CNOT}\}, \quad (3.23)$$

$$\mathcal{G}_2 = \left\{R_x\left(\frac{\pi}{2}\right), R_z(\theta), \text{CNOT}\right\}, \quad (3.24)$$

are two interesting examples. The universality of \mathcal{G}_1 can be shown in three steps, following Ref. [4]. The first construction shows that any unitary matrix can be decomposed into a product of unitary matrices acting non-trivially on two vector components. The second step shows that any of these two-level unitary matrices can be expressed in terms of CNOTs and

single-qubit gates. The idea behind this is that it is always possible to recast a two-level unitary matrix into the matrix corresponding to a single-qubit gate through conditional flips of the qubit states, which can be always obtained using combinations of CNOT and single-qubit gates. Finally, the third step makes use of the fact that any single-qubit gate can be approximated with an arbitrary accuracy using only H and T , which completes the proof. Although $S = T^2$, it is included in the set \mathcal{G}_1 because of its natural role in the quantum error correction. It is important to stress that circuits consisting only of H , S and CNOT gates (the Clifford group's gates) can be simulated efficiently by classical means according to the *Gottesman-Knill theorem* [37]. This result is very important, because it shows that the gate T , which is the most problematic to error correct, can not be eliminated from the set \mathcal{G}_1 , if we want to achieve quantum advantage.

The universality of \mathcal{G}_2 can be proven by combining the first two constructions discussed above with the fact that the general single-qubit gate can be expressed in terms of $R_x(\phi/2)$ and $R_z(\theta)$. This stems from Eq. 3.15 which can be rewritten (a part of a global phase) as

$$U = R_z\left(\alpha - \frac{\pi}{2}\right) R_x\left(\frac{\pi}{2}\right) R_z\left(\alpha - \beta\right) R_x\left(\frac{\pi}{2}\right) R_z\left(\gamma - \frac{\pi}{2}\right). \quad (3.25)$$

\mathcal{G}_2 is the native gate set adopted in the processors based on *superconducting qubits* which are used in this work.

We conclude the section with the following remarks about the scaling. Although the arguments used above allow us to prove the universality of the sets, they say nothing about the scaling with the number of qubits of the number of gates required to approximate the unitary operations. This is of primary importance, because it is possible to show that there exist unitary transformations whose approximation requires *exponentially many gates*. Therefore the goal of the *quantum engineer* is to design algorithms making use of families of unitary transformations which can be approximated efficiently.

3.1.2 Measurement

At the end of a quantum circuit, a set of measurements is needed to extract information from the quantum state of the qubits. The theory of measurements is one of the most articulated and delicate on a conceptual point of view. Here we just illustrate some basic concept, and point to Ref. [4] for a more complete reading. We start introducing the concept of *projective measurement*, which is described by a Hermitian operator M with spectral decomposition

$$M = \sum_m m P_m, \quad (3.26)$$

where $P_m = |m\rangle\langle m|$ projects the quantum state on the eigenspace of M with eigenvalue m . The possible outcomes of the measurement correspond to the eigenvalues m with probability

$$p_m = \langle \psi | P_m | \psi \rangle. \quad (3.27)$$

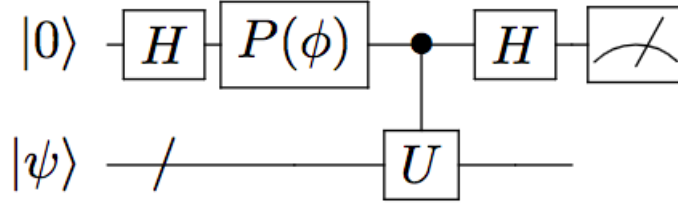


Figure 3.2: Circuit corresponding to the Hadamard test. The slash appearing in the bottom line indicates that it refers to multiple qubits, whose initial state is $|\psi\rangle$.

By changing the operator M we select the basis on which we want to measure. Most often we measure in the *computational base*, defined by the operator

$$\rho = \sum_{i_1, \dots, i_N} |i_1, \dots, i_N\rangle \langle i_1, \dots, i_N|. \quad (3.28)$$

A set of measurements in the computational basis allows to sample the coefficients $|\alpha_{i_1 i_2 \dots i_N}|^2$ defined in Eq. 3.4. It is important to stress that α is a complex number, therefore with the measurement we lose the information about its phase. For this reason, all the algorithms requiring the knowledge of the real and imaginary part of α must be carefully designed in order to rotate the phase of the qubits so that alpha is either a real or a purely imaginary number. An example is the following. Suppose we want to measure the expectation value of $\langle 0|U|0\rangle$, where $|0\rangle$ is the $|000\dots\rangle$ qubit state and U is a unitary operator, whose eigenvalues are *complex*. We may think to apply the unitary operator U to the qubit system and then measure in computational basis, thus obtaining $|\alpha_0|^2 = |\langle 0|U|0\rangle|^2$. But this would cancel all the information about the phase of the expectation value. We thus need a more complex circuit, which is known as *Hadamard test*, represented in Fig. 3.2.

We can easily check that the circuit allows to calculate the real part of $\langle \psi|U|\psi\rangle$ when $\phi = 0$ and the imaginary part for $\phi = -\frac{\pi}{2}$. First of all, it is necessary to prepare the state $|\psi\rangle$ on the qubit register. This can be always done by means of an opportune unitary transformation. The action of H on $|0\rangle$ creates the superposition $\frac{|0\rangle + |1\rangle}{\sqrt{2}}$, while the gate $P(\phi)$ rotates the phase of $|1\rangle$:

$$P(\phi)H|0\rangle = \frac{|0\rangle + e^{i\phi}|1\rangle}{\sqrt{2}}. \quad (3.29)$$

The action of the controlled-U (CU) turns the global qubit state into

$$\frac{|0\rangle}{\sqrt{2}} \otimes |\psi\rangle + \frac{e^{i\phi}|1\rangle}{\sqrt{2}} \otimes U|\psi\rangle. \quad (3.30)$$

The final state after the application of the second H is

$$\frac{|0\rangle}{2} \otimes (I + e^{i\phi}U)|\psi\rangle + \frac{|1\rangle}{2} \otimes (I - e^{i\phi}U)|\psi\rangle. \quad (3.31)$$

The z-measurement $p_0 - p_1$ of the first qubit gives

$$\frac{1}{4} \langle \psi | (I + e^{-i\phi} U^\dagger) (I + e^{i\phi} U) | \psi \rangle - \frac{1}{4} \langle \psi | (I - e^{-i\phi} U^\dagger) (I - e^{i\phi} U) | \psi \rangle = \Re \langle \psi | e^{i\phi} U | \psi \rangle, \quad (3.32)$$

which is equal to

$$\Re \langle \psi | e^{i\phi} U | \psi \rangle = \begin{cases} \Re \langle \psi | U | \psi \rangle, & \phi = 0 \\ \Im \langle \psi | U | \psi \rangle, & \phi = -\frac{\pi}{2} \end{cases} \quad (3.33)$$

The Hadamard test will play a central role in Chap. 6, where it will be used to design an efficient algorithm for the calculation of the Green's function.

3.1.3 Errors

The theory of quantum computing is based on the assumption that the set of qubits behaves as an *isolated* quantum system. In practice, it is very difficult to protect the qubits from the interaction with the environment, which modifies their dynamics thus leading to noisy results. Additional errors occur in the process of initialization and measurement. The impact of the noise can be reduced both by improving the quality of the hardware and implementing *quantum correction* codes [38]. Unfortunately, these codes require around 1000 physical qubits to correct a logical qubit, and are not implementable on the current quantum processors.

In order to obtain meaningful results from the current noisy quantum processors, we need to design shallow circuits, i.e. circuits with the least number of gates possible, in order to reduce the errors associated to the gates. In IBM Quantum processors, the error rate of two-qubit gates is around 10^{-2} while that of one-qubit gates is ten times smaller. The accuracy of the results is thus limited essentially by the number of the formers. As a thumb rule, this number should not be higher than ~ 20 per circuit. Since the number of CNOTs required by an algorithm is proportional to the number of qubits used, it is easy to understand that, although the current quantum processors have up to 60 qubits, we can use only a limited number of them.

3.1.4 Quantum annealing

To provide a complete picture, we expand the discussion about the quantum annealing technique introduced in Sec. 2.2.3. Unlike the *digital quantum computing* presented so far, the quantum annealing (also called *analogic quantum computing*) can be used to solve only a specific category of problems, i.e. the optimization. As anticipated, this technique exploits the Gell-Mann and Low theorem, which states that, when turning on very slowly the interaction in a quantum system, its physical state naturally evolves from the ground state of the non-interacting system to that of the fully-interacting system. The idea behind quantum annealing is thus to map the optimization problem into a qubit Hamiltonian, so that the knowledge of the ground state of the latter directly points to the solution to the former. The steps are the following:

1. The qubit register is first prepared in the ground state of the non-interacting Hamiltonian. This can be usually done without problems, as the non-interacting ground state is usually a simple product state.
2. The interacting term is turned on, very slowly. This means to act physically on the qubit register, e.g. through electromagnetic fields.
3. After a time which is long enough, the physical state of the qubit coincides with the fully-interacting ground state, and its energy can be associated to the optimum value of the minimization problem.

This method is very appealing, as the Gell-Mann and Low theorem ensure that the solution found coincides with the *global minimum*, and has lead to interesting results for different applications [39, 40]. However, its main limitation relies in the “long duration” of the experiment, which should be infinite in principle. This requirement is very demanding because of the short coherence time of the current noisy quantum hardware.

3.2 Quantum hardware

Since the theorization of quantum computers in 80' s, many typologies of hardware have been proposed. At the time of writing, superconducting qubits [41] and trapped ions [42] seem to be the most promising platforms which could lead to the realization of a large, scalable and reliable digital quantum computer in the next decades. The first are made up of superconducting circuits with quantized current, behaving as anharmonic oscillators. The trapped ion technology, instead, relies on charged particles suspended in free space thanks to electromagnetic fields. Quantum information is stored in stable electronic states of each ion, and is transferred through the collective quantized motion of the ions in a shared trap. However, several challenges remain to be addressed in the scaling up of these technologies [43]. This is the reason why research is focusing also on other architectures, such as photonic chips [44, 45] controlled impurities in silicon [46], semiconductor based quantum dots [47] and Rydberg atom arrays [48] could also potentially emerge as contending candidates for building a large scale and fully operational quantum computer. Finally, defect centers in semiconductors, such as the negatively charged nitrogen vacancy center in diamond, stood out among the qubit candidates of the first hour due to their extremely long coherence time at room temperature.

In any case, in order to actually build a digital (universal) quantum computer some requirements must be met by the chosen architecture according to the proposal of David DiVincenzo [49]:

- A scalable physical system with well characterized qubits.
- The ability to initialize the state of the qubits to a simple fiducial state.

- Long relevant coherence times.
- A universal set of quantum gates.
- A qubit-specific measurement capability.

3.2.1 Superconducting qubits

Superconducting qubits are made up of micrometer-sized circuits which behave as anharmonic quantum oscillators when cooled at sufficiently low temperatures (10-15 mK). Depending on the circuit involved, the qubit states can be encoded in the quantum oscillations of Cooper pairs on a superconducting island (charge qubits) [50], or different numbers of magnetic flux quanta trapped in a superconducting ring (flux qubits) [51] or phase across a Josephson junction (phase qubits) [52]. Other than these basic models, many hybridized devices exist, including the Fluxonium [53], Transmon [54], Xmon [55] and Quntronium [56]. Here, we will mainly focus on transmon qubits, which are those implemented in IBM Quantum Devices [57], and briefly sum up the theory presented in Ref. [58].

The quantum properties of these circuits can be easily understood considering a LC circuit (See Fig 3.3a) of Hamiltonian

$$\hat{H}_{LC} = \frac{\hat{Q}^2}{2C} + \frac{\hat{\Phi}^2}{2L}, \quad (3.34)$$

where the charge \hat{Q} and the flux $\hat{\Phi}$ operators are canonical conjugate observables

$$[\hat{\Phi}, \hat{Q}] = i\hbar. \quad (3.35)$$

If we define the reduced charge $\hat{n} = \hat{Q}/2e$ and flux $\hat{\phi} = \hat{\Phi}/\Phi_0$ with $\Phi_0 = \hbar/2e$, the Hamiltonian becomes

$$\hat{H}_{LC} = 4E_C \hat{n}^2 + \frac{1}{2} E_L \hat{\phi}^2. \quad (3.36)$$

(where \hat{n}^2 stands for $\hat{n}\hat{n}^\dagger$). The Hamiltonian in Eq. 3.36 is formally equivalent to that of a quantum harmonic oscillator

$$\hat{H}_{os} = \frac{\hat{p}^2}{2m} + \frac{1}{2} k \hat{x}^2, \quad (3.37)$$

with

$$[\hat{x}, \hat{p}] = i\hbar. \quad (3.38)$$

It is thus possible to define creation and annihilation operators \hat{a} and \hat{a}^\dagger

$$\hat{n} = \left(\frac{E_L}{32E_C} \right)^{1/4} i(\hat{a} - \hat{a}^\dagger), \quad \hat{\phi} = \left(\frac{2E_C}{E_L} \right)^{1/4} (\hat{a} + \hat{a}^\dagger), \quad (3.39)$$

such that the Hamiltonian is diagonal:

$$\hat{H}_{LC} = \hbar\omega_r \left(\hat{a}^\dagger \hat{a} + \frac{1}{2} \right), \quad (3.40)$$

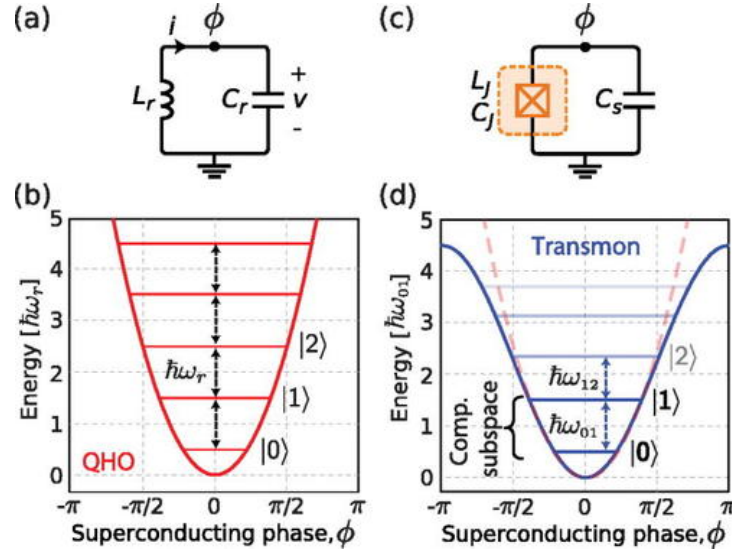


Figure 3.3: As it can be easily seen in panel (b), the energetic levels of the linear LC circuit (a) are equally spaced, making it impossible to address the transition $|0\rangle \rightarrow |1\rangle$ individually. The insertion of a non-linear induction in the circuit (c) adds a small anharmonicity, as a consequence of which the energy levels are not equally spaced anymore, as shown in panel (d). This allows to address the transition $|0\rangle \rightarrow |1\rangle$ without affecting the other transitions. This figure is taken from Ref. [58].

with $\omega_r = \sqrt{8E_L E_C}/\hbar$. The ladder structure of such a quantized Hamiltonian is pictorially represented in Fig 3.3b. It is easy to see that the energy difference between the states $i+1$ and i , i.e. $\Delta E_{i+1,i} = \omega_r \hbar$, is independent from i . This means that when exciting the system e.g. with electromagnetic waves of frequency $\omega = \omega_r$, all the transitions $i \rightarrow i+1$ will be addressed, thus making the realization of a qubit impossible. It is thus necessary to add a source of anharmonicity which will split the oscillator levels unevenly. This is achieved by adding a Josephson junction to the superconducting circuit, which behaves as a non-linear inductor. The Hamiltonian of the system is modified as

$$\hat{H}_{JC} = 4E_C \hat{n}^2 - E_J \cos(\hat{\phi}), \quad (3.41)$$

where $E_C = e^2/(2[C + C_J])$ is the total capacitance energy (which includes the contribution C_J of the Josephson junction) and $E_J = I_C \Phi_0$, with I_C being the critical current on the Junction. At this point, the only difference between charge qubits and transmons relies in the regime dictated by the ratio between E_C and E_J . Over time, the superconducting qubit community has converged toward circuit designs with $E_J \gg E_C$ (transmon regime), where the qubit is highly sensitive to the flux noise but not to the charge noise, which is difficult to mitigate. In this regime, which is realized by shunting the junction with a large capacitor $C \gg C_J$, the flux is a good quantum number. Since $\hat{\phi}$ is usually small, the Josephson part of the Hamiltonian

can be expanded in Taylor series:

$$E_J \cos(\hat{\phi}) = \frac{1}{2} E_J \hat{\phi}^2 - \frac{1}{24} E_J \hat{\phi}^4 + o(\hat{\phi}^6), \quad (3.42)$$

which leads to the following quantized Hamiltonian

$$\hat{H}_{JC} = \omega_q \hat{a}^\dagger \hat{a} - \frac{E_C}{2} \hat{a}^\dagger \hat{a}^\dagger \hat{a} \hat{a}. \quad (3.43)$$

Usually $\omega_q = (\sqrt{8E_J E_C} - E_C)/\hbar \simeq 3 - 6$ GHz and $E_C = 100 - 300$ MHz. Since $E_C \ll \omega_q$, the system is only weakly anharmonic. It is now possible to address the transition $|0\rangle \rightarrow |1\rangle$ without exciting the higher energies states, thus allowing to operate in the subspace spanned by the lowest two states, with Hamiltonian

$$\hat{H} = \frac{\omega_q}{2} Z. \quad (3.44)$$

The superconducting qubits can implement the fundamental operations of quantum computing:

1. **Initialization.** It is achieved by waiting long enough for the qubit to relax to its energy ground state.
2. **Readout.** The readout technique implemented on IBM Quantum devices is the *dispersive readout* [59], which is performed by coupling the qubit with a resonator, leading to the following Hamiltonian

$$\hat{H}/\hbar = \omega_{res} \left(\hat{a}^\dagger \hat{a} + \frac{1}{2} \right) + \frac{\omega_q}{2} Z + g(\sigma_+ \hat{a} + \sigma_- \hat{a}^\dagger), \quad (3.45)$$

where $\sigma_\pm = (X \pm iY)/\sqrt{2}$ and ω_{res} is the resonator frequency. The *dispersive regime* is that in which $g \ll \Delta = |\omega_q - \omega_{res}|$. In this regime, the Hamiltonian can be expanded as a series of g/Δ , obtaining

$$\hat{H}_{disp}/\hbar = \left(\omega_{res} + \frac{g^2}{\Delta} Z \right) \left(\hat{a}^\dagger \hat{a} + \frac{1}{2} \right) + \frac{1}{2} \left(\omega_q + \frac{g^2}{\Delta} \right) Z. \quad (3.46)$$

The last term in Eq. 3.46 introduces a splitting between the energies of the $|0\rangle$ and $|1\rangle$ levels which is used to discriminate the state of the system.

3. **Manipulation.** The transmon qubits in the IBM Quantum processors are controlled through *capacitive coupling* between the qubit and an external macroscopic microwave source, the *drive line*. When the potential of the drive line is tuned with the qubit frequency, so that its temporal law is

$$V_d(t) = V_0 s(t) \sin(\omega_q t + \phi), \quad (3.47)$$

the effective Hamiltonian of such a coupling is

$$\tilde{H}/\hbar = -\frac{\Omega}{2} V_0 s(t) (\cos(\phi) X + \sin(\phi) Y) , \quad (3.48)$$

where Ω is a coupling constant depending on the circuit. We can easily see that if $\phi = 0$, the qubit state is evolved of

$$U = e^{i \frac{\Omega V_0}{2} \int_0^t s(t') dt' X} = R_x(\theta) , \quad (3.49)$$

with

$$\theta = -\frac{\Omega V_0}{2} \int_0^t s(t') dt' . \quad (3.50)$$

By choosing instead $\phi = \frac{\pi}{2}$, the $R_y(\theta)$ rotation is implemented. In order to improve the fidelity, on IBM superconducting devices the *virtual Z gate* technique is used [60]: imagine to apply two pulses, the first with zero phase and angle θ , while the second with phase ϕ and the same angle θ . The unitary evolution of the qubit is thus

$$U = e^{-i \frac{\theta}{2} [\cos \phi X + \sin \phi Y]} R_x(\theta) , \quad (3.51)$$

which is mathematically equal to

$$U = R_z(-\phi) R_x(\theta) R_z(\phi) R_x(\theta) . \quad (3.52)$$

The gate $R_z(-\phi)$ does not affect the measures, which are carried in computational basis, and can be ignored. The fundamental result of Eq. 3.52 is that we can apply a virtual and thus high fidelity and 0-time rotation R_z by just acting on the phase shift between two pulses. Given that we can easily create Z gates, it is convenient to exploit Eq. 3.25 to express the general $SU(2)$ operation, and adopt $\{R_x(\frac{\pi}{2}), R_z(\theta)\}$ as universal 1-qubit set.

An example of IBM Quantum processor is shown in Fig. 3.4.

We conclude this section with a recap of the main characteristics of the IBMQuantum processor Falcon r4 *ibmq_montreal*, which is the main adopted for the calculation of the Green's function:

- resonance frequency $\simeq 5$ GHz;
- operating temperature $\simeq 15$ -20 mK;
- universal gate set implemented: $\mathcal{G}_2 = \{R_x(\frac{\pi}{2}), R_z(\theta), \text{CNOT}\}$;
- number of qubits = 27;
- single-qubit gates average error rate $\sim 5 \cdot 10^{-4}$;
- CNOT error rate $\sim 5 \cdot 10^{-3}$.

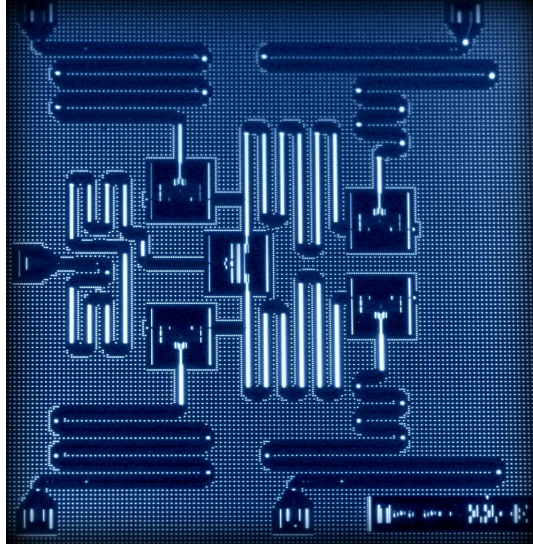


Figure 3.4: Example of IBM Quantum processor making use of 4 superconducting qubits.

3.2.2 Defect centers in semiconductors

Defect centers in semiconductors emerged for their very long coherence time at room temperature. These systems are usually *optically-addressed*, because their initialization and read-out are performed optically, even though it has been shown that the electrical readout is also possible [61, 62]. In order to understand how quantum operations can be performed on defect centers, it is necessary to introduce the representative of this category, the negatively charged nitrogen vacancy (NV^-) center in diamond. This system has been intensively studied for its exceptional coherence time of milliseconds at room temperature [63]. It is ideally obtained by replacing a pair of near neighboring carbon atoms with a nitrogen atom and a vacancy. The symmetry reduction from O_h to C_{3v} plays a fundamental role in the optical polarization cycle. Quantum information is stored in its paramagnetic ground state, a triplet of symmetry 3A_2 (see Fig. 3.5), while the relevant excited states are a triplet of symmetry 3E and two singlets of symmetry 1A_1 and 1E . Spin-spin interactions and spin-orbit coupling lift the degeneracy between the $m_s = 0$ and the $m_s = \pm 1$ levels of the triplets, causing a splitting of 2.88 GHz for the ground state and 1.42 GHz for the excited state. A further splitting between the $m_s = \pm 1$ levels of the triplet can be obtained by applying a magnetic field parallel to the axis of the defect, at a rate of 2.8 MHz/T. The energetic ordering of the excited states, particularly that of the singlets which are *dark*, has been matter of long debate [64, 65, 66, 67, 68, 69], and plays a crucial role in the process of optical polarization of the qubit. The conclusive picture of the defect energies is the one reported in Fig. 3.5.

Once the electronic structure is known, it is possible to understand the three fundamental operations which allow this system to behave as qubit:

1. **Initialization** When irradiating the defect with green light (546 nm), the electronic population is excited from the ground state 2A_3 to 3E with conservation of spin. Then

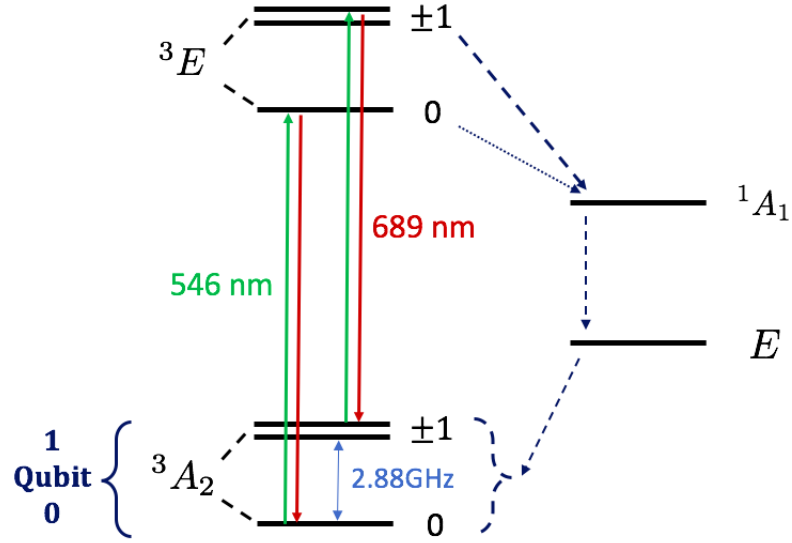


Figure 3.5: Energy diagram for the lowest states of the negatively charged nitrogen vacancy center in diamond. The 0 and ± 1 levels of the ground state triplet are split of 2.88 GHz. These levels correspond to the qubit states $|0\rangle$ ($m_s = 0$) and $|1\rangle$ ($m_s = \pm 1$). The spin conserving excitation (green arrow) can link only levels with the same spin 0 or ± 1 . The IC from 3E to A is much more likely if the spin is ± 1 , as symbolized by the thicker arrow.

it can either decay radiatively to the ground state with the emission of red light (689 nm) or undergo an intersystem crossing (IC) from 3E to 1A_1 , with a probability which is large for the $m_s = \pm 1$ state and small for the $m_s = 0$. The consecutive decay from 1A_1 to 1E_1 and then to the ground state happens with similar probability for the final states $m_s = 0$ and $m_s = \pm 1$. Therefore, if at the beginning of the evolution the electron is in the state $m_s = \pm 1$, then there is a good probability that it will undergo an IC and will end up in the state $m_s = 0$ at the end of the cycles. But once the electron ends in the $m_s = 0$, the probability of undergoing the IC and change spin is small, therefore it will remain trapped in this state. For this reason, after few optical cycles, a high percentage of the electron population will be initialized in the state $|0\rangle$ [70].

2. **Readout.** The IC is dark. The probability of undergoing the IC is larger for the initial state $|1\rangle$ than for the state $|0\rangle$, therefore the photoluminescent emission will be less intense if the initial state is $|1\rangle$ and brighter if the state is $|0\rangle$. This *spin-dependent luminescence* is used to perform the readout [71] (see Fig. 3.6).
3. **Manipulation.** The splitting of 2.88 GHz between the $|0\rangle$ and $|1\rangle$ levels allows manipulation through irradiation with micro-waves. The coupling between a electro-magnetic field and the spin of the NV center is described by the Hamiltonian

$$\hat{H} = g\mu_B \mathbf{B} \cdot \boldsymbol{\sigma} , \quad (3.53)$$

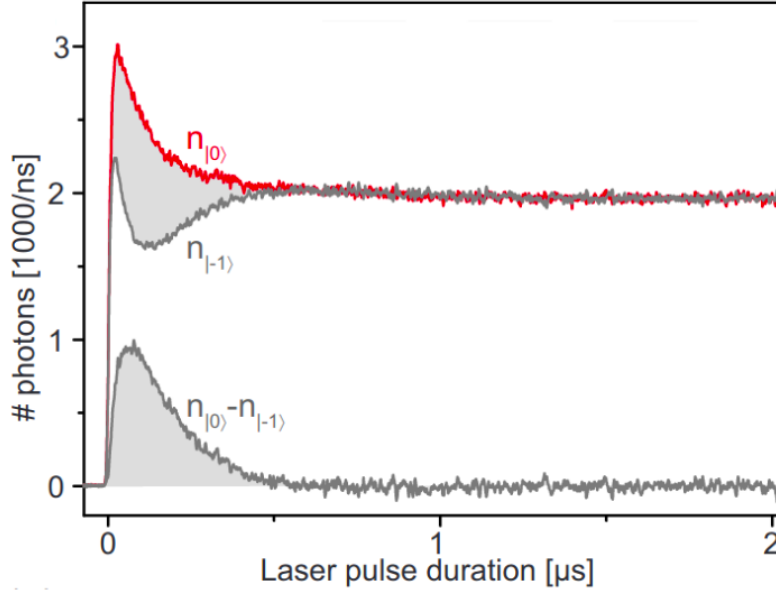


Figure 3.6: The red line marked with $n_{|0\rangle}$ shows the average count of phonons emitted when the state is initially $|0\rangle$, and is more intense than the grey line marked with $n_{|1\rangle}$, corresponding to the initial state $|1\rangle$. The difference between these two curves, reported in the lower part of the graph, is proportional to the fidelity of the measurement, i.e. how precisely the two states can be distinguished. This figure is adapted from Ref. [76].

where \mathbf{B} is the applied magnetic field, μ_B is the Bohr magneton and g is the Landé g -factor, which is a tensor whose value depends on the material. However, in most of the cases this tensor is isotropic with value $g \approx 2$. The evolution operator associated to this Hamiltonian is thus

$$U = e^{-ig\mu_B\mathbf{B}\cdot\boldsymbol{\sigma}t}, \quad (3.54)$$

which, according to Eq. 3.9, rotates the qubit state on the Bloch sphere around an axis parallel to the applied magnetic field, with frequency $\omega = 2g\mu_B|B|$. These dynamics would be perfectly coherent, if there were not additional dephasing terms due to the interaction with the surrounding magnetic ions

$$\hat{H}_{int} = \sum_n \boldsymbol{\sigma} \cdot \mathbf{A}_n \cdot \mathbf{I}_n, \quad (3.55)$$

where \mathbf{I}_n is the spin operator for the n -th ion and \mathbf{A}_n is the *hyperfine tensor*. These hyperfine interactions are the main cause of decoherence in NV center [72, 73]. In order to increase the coherence time, the NV center is created in isotopically purified samples. The interaction with the magnetic nuclei can be turned from a weakness into an opportunity, because the coherent dynamics of coupled electron and nuclear spin can be used to realize qubit registers [74, 75]. More complex operations, such as the controlled rotations can be implemented as described in Ref. [76].

The exceptional properties of the NV center in diamond have pushed the research in novel defect centers in semiconductors. In analogy with the famous DiVincenzo criteria [49] for a general qubit to work, Weber et al. [77] identified five main conditions to be satisfied in order to use a defect for quantum computing:

1. A bound state that is paramagnetic and long-lived, with a splitting between at least two of the spin sub-levels whose size falls in the range of radio frequencies.
2. An optical pumping cycle that polarizes the qubit state. The cycle most likely consists of a transition from the ground to an excited state, followed by a spin-selective decay path.
3. Luminescence that varies by qubit sub-level (0 - 1), whether by intensity, wavelength or other properties. The difference must be marked enough to allow high fidelity measurement.
4. Optical transitions that do not introduce interference from the electronic state of the host.
5. Bound states that are separated from each other by energies large enough to avoid thermal excitation between them, which would destroy the coherence.

In addition, four minor requirements should be also verified, the presence of a large band-gap for satisfying automatically point 4, small spin-orbit coupling in order to avoid unwanted couplings between the $S = 0$ and $S = 1$ levels of the qubit, availability of high quality bulks, so that interactions with different kinds of defects are excluded and constituent elements with low natural abundance of magnetic isotopes, to reduce the decoherence due to hyperfine interactions.

Following these criteria, many researchers proposed solid-state qubits candidates based on defect centers in diamond [78], aluminum-nitride [79, 80, 81] and silicon-carbide [82].

Although being potential qubit candidates, defect in semiconductors are very promising for quantum sensing [9, 10, 11, 12, 13], since the splitting of the ground state sublevels is very sensitive to magnetic fields and strain, and the features of the photoluminescence spectrum depend sharply on the temperature. They have also been successfully used to implement quantum communication protocols [7, 8].

In the very recent years, the search for novel defect centers in semiconductor has finally addressed 2D materials. Particularly, a great deal of attention has been focused on defect centers in 2D hexagonal boron nitride [83, 84, 85, 86], where a wide band-gap, together with low spin-orbit coupling and reduced dimensionality, may overcome the limitations of existing 3D defect centers in terms of coherence [87], resolution and interfaciability with cavities and resonators [14]. In particular, the negatively charged boron vacancy (V_B^-) in 2D hBN has been predicted to be responsive to optically-detected magnetic resonance (and thus usable for quantum computing), and to emit in the infrared when stimulated with continuous green

laser light [14]. Since this photoluminescence is a key property in this material, as it is used for the readout of its state at the end of a quantum computing/communication protocol, is the measured property in quantum sensing, and is also adopted for the characterization of the defect, its prediction from first-principles is extremely important for the advancement of the research and for an improvement in the understanding of this defect. The next chapter illustrates the effort in the theoretical prediction of the photoluminescence of V_B^- and its dependence on temperature.

4 Phonon-assisted luminescence in V_B^-

In this chapter, we study the electronic and optical properties of V_B^- , using the MBPT introduced in chapter 2. Particularly, we focus on the theoretical prediction of photoluminescence (PL). Due to the coupling of excitons with vibronic modes of the atoms around a defect, the photoluminescence of defect centers in semiconductors is often phonon-assisted. This is usually studied using the Huang-Rhys model [88, 89, 90, 91, 92, 93], whose parameters are determined through constrained-DFT or quantum-chemistry calculations, as reviewed in Ref. [94]. The Huang-Rhys model, which has proven to give very good results for defects in diamond and silicon carbide [89, 95], is based on the assumption that the optical dipole moments are not affected by phonons (Franck-Condon approximation), which limits its predictive power for systems (such as V_B^-) where the phonon-independent dipole moment vanishes. Furthermore, it does not lead to an interpretation of the phonon-assisted luminescence in terms of coupling between excitons and phonons, which is essential for the understanding of this phenomenon.

The optical properties of *pristine* hBN have been studied using MBPT [96, 97], and its phonon-assisted emission spectrum has been calculated both for the bulk and the monolayer [36, 98, 99]. However, due to the complexity and computational cost of these analyses, the luminescence of defect centers has never been studied with such advanced methods.

In the following, we investigate the optical properties of the negatively charged boron vacancy in 2D hBN using first-principles MBPT, and compare with the experimental results of Ref. [94]. This predictive approach for the luminescence of defect centers gives a tool to include the nontrivial couplings beyond the Franck-Condon approximation for PL lineshapes, and allows to reach a microscopic understanding of the emission mechanism in these systems. In particular, we study the coupling between excitons and phonons leading to the phonon-assisted luminescence, and identify the phonon modes which interact most strongly with excitons, thus leading to peaks in the sideband of the emission spectrum. We show that the phonon-independent emission is dark due to symmetry reasons, and prove that the emission observed experimentally is due to the symmetry-breaking caused by phonons. Conversely, we show that the symmetry-breaking induced by the static Jahn-Teller effect is not able to activate photoluminescence.

4.1 Electronic structure and excitons in pristine hBN

In this section, we analyse the electronic structure and optical properties of the pristine 2D hBN. This will be useful to understand the more complex properties of the negatively charged boron vacancy. The 2D hBN is a largely studied two dimensional material, characterized by a honeycomb lattice where the boron and nitrogen atoms are arranged in triangular sublattices (see Fig. 4.1). The reflection symmetry about the materials plane confers this system a D_{3h} point group. The wide band-gap of this semiconductor (around 6.0 eV) makes of it a very good candidate to host deep centers for quantum information and quantum computing. We

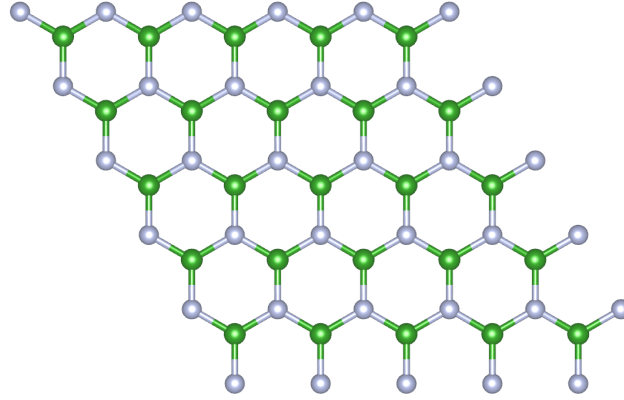


Figure 4.1: Structure of the 2D hBN.

study its electronic structure performing first DFT calculation with the open-source Quantum ESPRESSO distribution [16], using a planewave cutoff of 80 Ry and sampling the Brillouin zone with a 16x16x1 unshifted grid. The norm-conserving pseudopotential adopted for boron and nitrogen are taken from the PseudoDojo library [100]. We then apply a G_0W_0 correction under the plasmon-pole approximation [101], using the Yambo Code [102, 103]. We use 5 Ry and 30 Ry cutoff respectively for the response function and the exchange self-energy, and sum 200 bands both for the response function and the correlation self-energy (corresponding to an energy window of ~ 100 eV). The DFT band structure, represented in black solid line in Fig. 4.2, predicts a *direct* band-gap of 4.8 eV at the point K of the Brillouin Zone. As expected, this value underestimates the experiments [104]. The G_0W_0 correction of the band structure, represented in red dotted line, predicts instead an *indirect* band-gap of 6.0 eV between the K and Γ . Since, after the excitation with a laser, electrons and holes relax respectively towards the bottom of the conduction and the top of the valence band, the radiative recombination requires the scattering with phonons of momentum $q = |\Gamma - K|$, meaning that the luminescence of this material is phonon-assisted [98].

As 2D hBN is an atomically thin material, the electronic screening is small and spatially confined around the material's plane, thus leading strong excitonic effects. In order to correctly

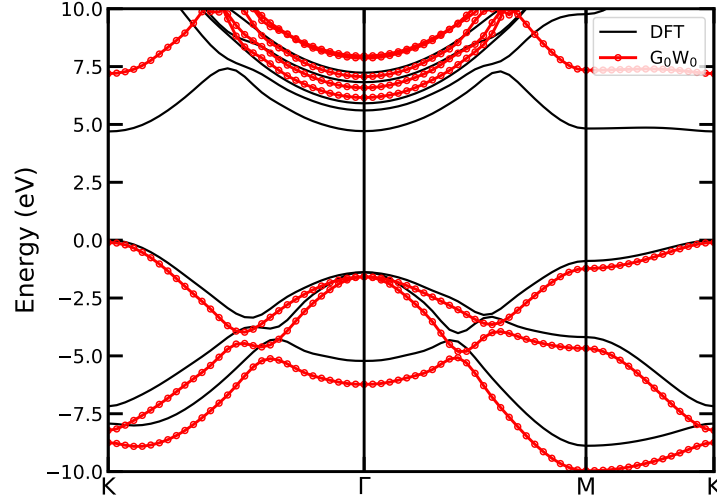


Figure 4.2: the band structure of pristine 2D hBN, calculated at the DFT (black) and GW (red) level of theory.

account for them, it is necessary to calculate the dielectric function by solving the Bethe-Salpeter equation. This is done using 4 Ry cutoff for the electron-hole attraction part of the kernel, 9 Ry cutoff for the exchange part of the kernel and bands from 1 to 10 (~ 20 eV). The Brillouin zone is sampled with a 20×20 k-points grid. In order to avoid spurious interactions between periodic images in the out-of-plane direction, we use the cutoff for the Coulomb potential suggested in Ref. [105], and size the simulation cell so that the length of the out-of-plane lattice vectors is 37.9 a.u. The absorption spectrum is shown in Fig. 4.3. The blue dots correspond to the squared modulus of the exciton dipole moment (Π_λ^2), which is also known as exciton strength. This spectrum is dominated by two peaks. Both these peaks, of energies 5.3 eV and 6.15 eV respectively, are associated to direct transitions around the K-point of the Brillouin zone. The band-gap at this point is around 7.3 eV, witnessing very large exciton binding energies, respectively 2.0 eV and 1.15 eV. The wiggles at energies higher than 6.2 eV are due to numerical effects, and tend to disappear when the sampling of the Brillouin zone is further increased.

4.2 Electronic structure of V_B^-

In order to study the negatively charged boron vacancy in 2D hBN we perform DFT calculations using the PBE exchange-correlation functional on a 8×8 supercell. The planewave cutoff used is 80 Ry and the Brillouin zone is sampled with a $2 \times 2 \times 1$ unshifted grid. We use the same norm-conserving pseudopotentials for boron and nitrogen as for pristine hBN.

Following to the creation of the boron vacancy, the neighboring nitrogen atoms relax outwards, with a distance of 5.00 a.u. from each other, corresponding to 1.05 times the boron nitride lattice parameter (see Fig. 4.4). The dangling bonds left by the removal of the boron atom

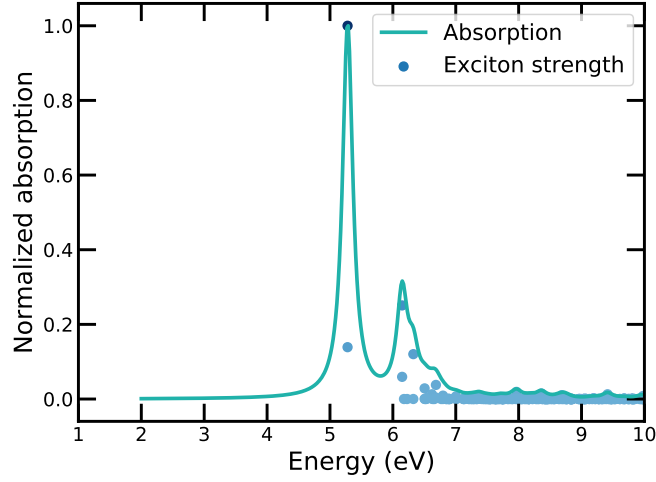


Figure 4.3: This figure shows the absorption spectrum of the pristine hBN.

form localized states around the vacancy, and cause the appearance of discrete levels in the band-structure. For example, the state whose wavefunction is shown in Fig. 4.5 is made up of a linear combination of the boron-nitrogen σ -bonds, and corresponds to the spin down level a'_1 in the defect diagram represented in Fig. 4.6.

We correct the Kohn-Sham eigenvalues with a G_0W_0 calculation under the plasmon pole approximation, using the Yambo code. We use 5 Ry and 19 Ry cutoff respectively for the response function and the exchange self-energy, and sum 2000 bands (~ 44 eV) both for the response function and the correlation self-energy. We sample the Brillouin zone with a $2 \times 2 \times 1$ unshifted grid. We checked the results by performing the same calculations on a 10×10 supercell, sampling the Brillouin zone with a gamma-only grid, summing 3000 bands (~ 43 eV) both for the response functions and the correlation self-energy and using 4 Ry and 15 Ry cutoff respectively for the response function and the exchange self-energy.

A lot of information about the optical properties of this system can be obtained by simply studying its electronic structure, focusing particularly on the position of defect levels inside the band-gap. The presence of the negatively charged boron vacancy in 2d hBN causes the appearance of many donor levels close to the valence band, but just one spin down empty acceptor close to the conduction band (see Fig. 4.6). The presence of such a spin down acceptor opens up transition channels inside the bandgap, which are responsible for the observed emission (as it will be explained in detail in the next sections). The absence of an empty spin up electron in the higher part of the band-gap forces the spin up electrons to be excited directly to the conduction manifold. The defect levels are labeled by the irreducible representation of the D_{3h} group corresponding to the symmetry of their wavefunction. The knowledge of these irreducible representations is extremely useful, as it allows us to determine a priori which optical transitions are forbidden by symmetry. It is simply necessary to use the symmetry product rules to determine whether the dipole defined in Eq. 2.95 vanishes. We do this explicitly for the transition between the highest occupied spin down levels a'_1 , e'' ,

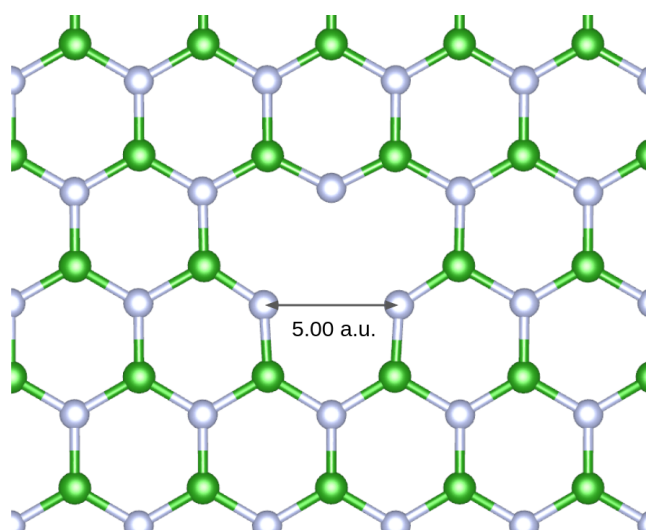


Figure 4.4: Ground state geometry of V_B^- in 2D hBN.

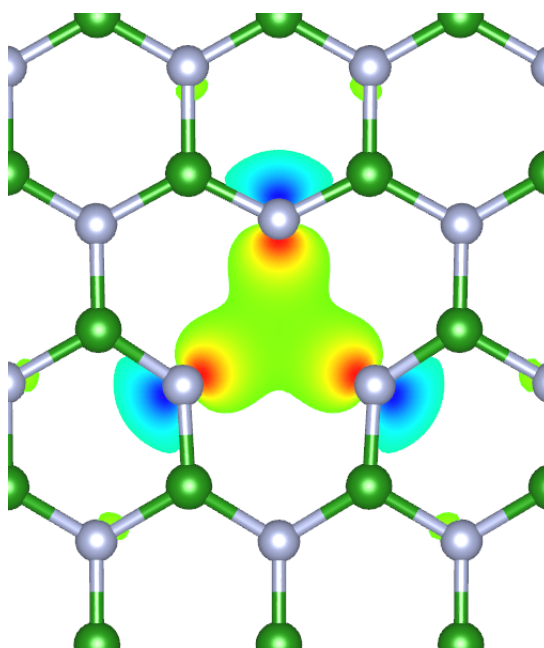


Figure 4.5: Wavefunction of a spin down defect level of symmetry a_1' . We can see that it is very localised around the vacancy, and possesses all the symmetries of the D_{3h} group.

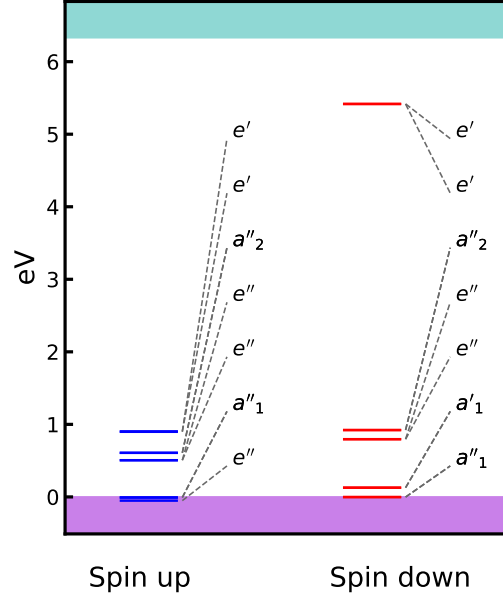


Figure 4.6: This figure shows the defect levels inside the band-gap in V_B^- . The blue lines on the left correspond to the spin up levels, while the red lines on the right to the spin down ones.

a''_2 and the lowest unoccupied spin down level e' , as they play a very important role in both absorption and emission. According to the character table for the symmetry group D_{3h} , the x and y (in-plane) components of the displacement operator \hat{r} transform as the irreducible representation e' , while the z (out-of-plane) component transforms as a''_2 . By applying the product rule we obtain that

1. the transition $a'_1 \leftrightarrow e'$ has a non-vanishing in-plane dipole (i.e. $\langle a'_1 | (x, y) | e' \rangle \neq 0$); therefore, it is expected to contribute to the absorption spectrum with an intense peak.
2. the transition $e'' \leftrightarrow e'$ has a non-vanishing out-of-plane dipole but a vanishing in-plane dipole. Since 2D hBN is an atomically thin material, the out-of-plane polarization is much weaker than the in-plane one, therefore this transition is expected to contribute weakly to the absorption spectrum.
3. the transition $a''_2 \leftrightarrow e'$ is forbidden by symmetry, therefore no contribution to the absorption is expected.

4.3 Optical absorption and excitons

We calculate the absorption spectrum by solving the Bethe-Salpeter equation on the 8x8 supercell. We use 2 Ry cutoff for the electron-hole attraction part of the kernel, 9 Ry cutoff for

the exchange part of the kernel and bands from 190 to 320 (~ 11 eV, whose energy is corrected through the G_0W_0 approximation). The FFT grid is reduced to 21 Ry. The Brillouin zone is sampled with a $2 \times 2 \times 1$ k-points grid. Also in this case we double check the results by repeating the calculations for a 10×10 supercell. The absorption spectrum is shown in Fig. 4.7 and

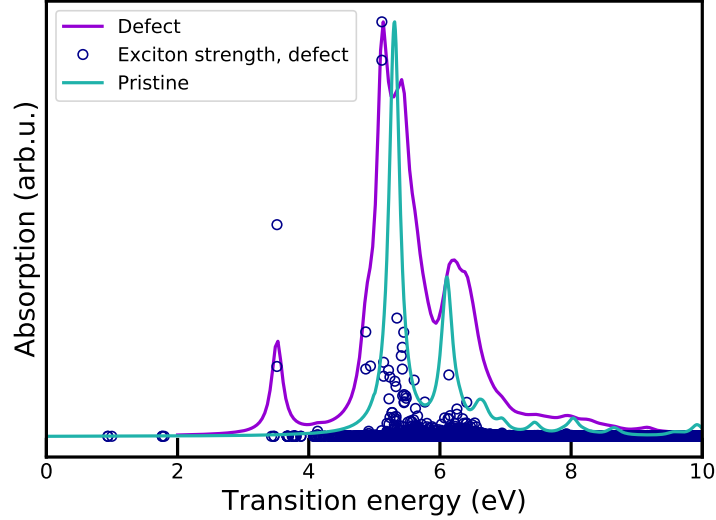


Figure 4.7: Absorption spectrum for V_B^- center in 2D hBN (purple line) and for the pristine 2D hBN (light blue line). The blue circles represent the strength of the excitons of the defected system as a function of their energy.

compared with that of the pristine 2D hBN studied in the previous section. The blue dots correspond to the squared modulus of the exciton dipole moment ($|\Pi_\lambda|^2$), which is also known as *exciton strength*. Here we perform an analysis similar to that reported in Ref. [106] for the absorption spectrum of the neutral defects in 2D hBN. The strong peak at 5.3 eV which dominates the pristine spectrum, is splitted into two subpeaks at 5.15 eV and 5.40 eV by the resonant coupling of transitions between the extended conduction and valence states with the defect states close to the band edges. The shoulder at 4.85 eV, instead, arises due to the mixing of the transitions from the defect levels to the conduction band and the bulk excitations.

A new peak, which is absent in the pristine spectrum, appears at 3.5 eV. It corresponds to an exciton that is localised on the transition $a'_1 \leftrightarrow e'$, which, according to the symmetry rules listed above, is expected to contribute sharply to the absorption due to its in-plane dipole. It is worth stressing that the energy of this peak is significantly smaller than the energy difference between the defect levels e' and a'_1 , which is around 4.3 eV, witnessing the importance of excitonic effects in this material. In the lower frequency part of the plot we notice the presence of dots with negligible strength, at 0.94 eV and 1.77 eV. These very weak excitons are localised on the transitions $e'' \leftrightarrow e'$ (which has a weak out-of-plane dipole) and $a''_2 \leftrightarrow e'$ (which is forbidden by symmetry). The presence of this excitons is confirmed when repeating the calculations using a 10×10 supercell. Although their contribution to absorption is irrelevant, they will play a fundamental role in the photoluminescent emission, which is peaked at 1.6

eV. The convergence of exciton energies with respect to the size of the cell has been checked by repeating the calculations on a 10x10 supercell. For instance, the energy of the exciton which is responsible for the first peak at changes from 3.51 eV (8x8 supercell) to 3.49 eV (10x10 supercell) denoting very tight convergence. We can thus see that the exciton energies do not suffer the well-known convergence issues affecting the defect energetics [107, 108], which are caused by the integral over bigger and bigger cells of the slow-decaying tail of the electrostatic potential.

4.4 Photoluminescence of V_B^-

4.4.1 Purely-electronic luminescence

In this chapter, we study the luminescence of V_B^- , and report the results which are published in Ref. [109]. We first use the formula derived in the Sec. 2.3 to calculate the purely-electronic photoluminescence, i.e. luminescence in absence of phonons. In the current work, we set the chemical potential for the electrons in such a way that a whole electron is promoted to the excited state manifold, consistently with what is done in works based on quantum chemistry techniques or cDFT [94]. The occupation picture is shown in Fig. 4.8. In Fig. 4.8b

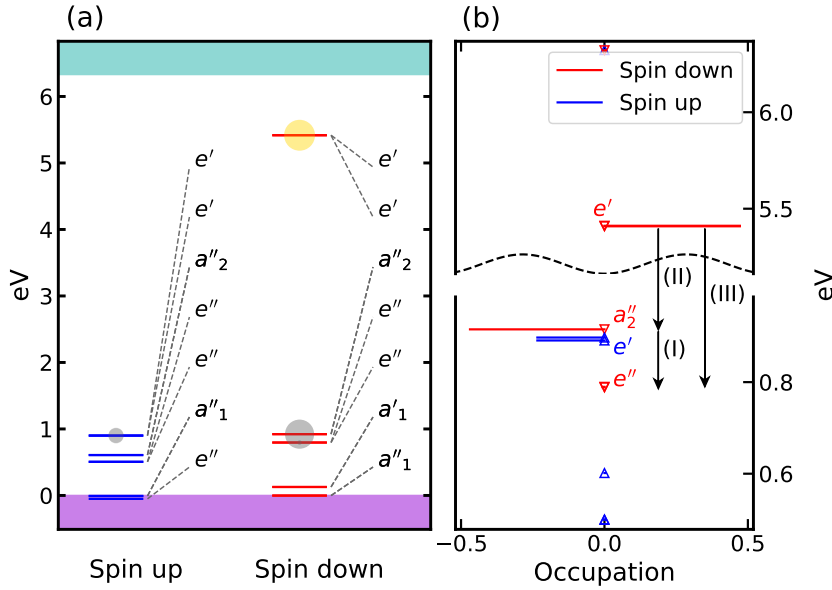


Figure 4.8: Panel (a) shows the defect levels inside the band-gap for V_B^- center in 2D hBN, determined through G_0W_0 calculations. The blue and red lines represent spin up and spin down levels respectively. The yellow and grey circles represent pictorially the non-equilibrium occupations of the levels. Panel (b) shows the non-equilibrium occupations of the defect levels as a function of their non-renormalized energies. The black arrows mark the only possible recombinations which can give rise to photoluminescence.

we show the non-equilibrium occupation of the defect levels (Eq. 2.130) as a function of their quasiparticle energy at 300 K. Only the energy levels closest to the band edges will show significant populations (with a thermal width of 26 meV). The spin down degenerate levels e' are occupied on average by one excited electron (0.5 each), while the spin down a_2'' level by close to 0.5 holes. The spin down level e'' has a very small but not negligible population (0.006 holes), while all the other spin down levels are empty. Only transitions between these levels will contribute to the photoluminescence.

In order to calculate the luminescence we solve the fractional-occupations Bethe-Salpeter equation using a not-yet released version of Yambo [102]. We compute the spectrum using Eq. 2.131 and show it in Fig. 4.9. It is made up of three main peaks: the first peak at 0.6 eV (I in Fig. 4.9) is mainly associated to the spin down $a_2'' \rightarrow e''$ transition, which has a non vanishing in-plane dipole. Due to the very small hole population of the level e'' , this peak is expected to be extremely weak, and is not observed in experiments; for the same reason the third peak at 3.3 eV (III in Fig. 4.9) is very weak and not observed, despite the finite out-of-plane dipole moment of the transition. It is associated to the transition between the spin down levels e' and e'' . Last, the second peak at 1.5 eV (II in Fig. 4.9) is associated to the transition from the spin down level e' to a_2'' , which is the only one where both the levels involved have a non-negligible population in terms of electrons/holes. However, this transition is prohibited by symmetry, therefore the corresponding peak is even weaker than the others. So, two of the three peaks are very weak because of population arguments, and are not observed in experiments, while a third peak, which has the same energy of the peak observed experimentally (1.5 eV), is dark due to symmetry reasons. Following this analysis, we can conclude that there must be some symmetry-breaking phenomenon which enables the transition $e' \rightarrow a_2''$ (the only one which is not removed by the lack of electron/hole population) and leads to the peak at 1.5 eV which dominates the photoluminescence spectrum, and makes it observable by experiments. The two main candidate mechanisms to activate the second peak are the Jahn-Teller distortion of the excited state e' , and lattice vibrations. In the following sections, we highlight the contribution of both these effects to the “activation” of the luminescence peak.

4.5 Jahn-Teller distortion

The doubly degenerate excited state which is obtained promoting an electron from a_2'' to e' can undergo a Jahn-Teller distortion which reduces the symmetry of the system from D_{3h} to C_{2v} , splits the levels e' into a_1 and b_1 , and changes the irreducible representation of the level a_2'' into b_2 (4.11). The transition $a_1 \rightarrow b_2$ has now a non-vanishing out of-plane-dipole, while the transition $b_1 \rightarrow b_2$ is still forbidden. We determine the geometry of the two Jahn-Teller distorted by relaxing the structure of the material when constraining the occupation of one of the e' levels to 1 and that of the level a_2'' to 0 and slightly distorting the initial positions of the atoms, in order to move away from the symmetric local minimum. Depending on the initial position of the atoms, the relaxation procedures outputs two different structures, one where the nitrogen atoms around the vacancy form a triangle with a sharper angle 57.5° , and one

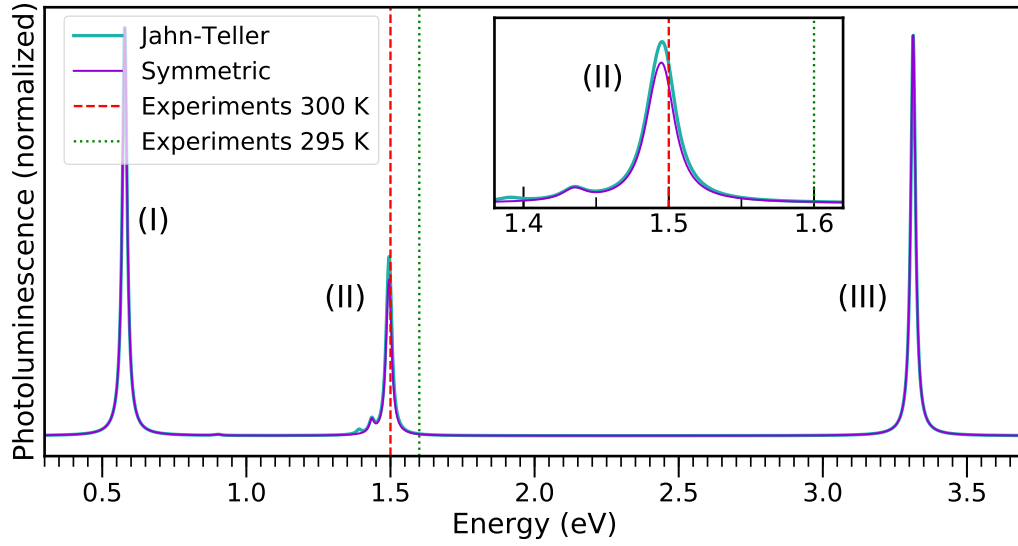


Figure 4.9: The phonon-independent photoluminescence spectrum of the original symmetric system (purple solid line) is compared to that of the Jahn-Teller distorted system (light blue solid line). The roman numbers indicate which of the recombinations reported in Fig. 4.8b is associated to the peak. The activation of the transition $a_1 \rightarrow b_2$ caused by the symmetry breaking due to the Jahn-Teller effect leads to an enhancement of the peak at 1.5 eV, which, however, is still weaker than the other two peaks and therefore not observable by experiments.

where the angle is 62.1° (see Fig. 4.10). One of them has the level a_1 lying below the level b_1 , while in the other this order is switched. In our occupation model, only the lowest-lying empty level has a non-negligible nonequilibrium population. Therefore, we consider the atomic configuration in which the a_1 level is the lowest (Fig. 4.11), as the transition $a_1 \rightarrow b_2$ is allowed by symmetry while the transition $b_1 \rightarrow b_2$ is forbidden (see Tab. A.3b).

Since the Jahn-Teller distortion is small, we assume in a first approximation that the exciton energies and wavefunctions remain equal to those of the original symmetric system. The significant difference between the distorted and the symmetric systems is that now the transition $a_1 \rightarrow b_2$ ($e' \rightarrow a_2''$) is symmetry-allowed, and this affects the contribution of each exciton to the photoluminescence spectrum. Therefore, in order to check whether the Jahn-Teller effect could be the responsible for the activation of the peak at 1.5 eV, we compute the dipole matrix elements corresponding to the transitions $a_1 \rightarrow b_2$ and $b_1 \rightarrow b_2$ for the distorted system, and use these to recalculate the exciton contributions to photoluminescence. As shown in Fig. 4.9, the activation of the transition $a_1 \rightarrow b_2$ caused by the symmetry break leads to an enhancement of the peak at 1.5 eV. This enhancement, however, is still not sufficient, as this peak remains weaker than the other two peaks, which are not observable as discussed before. Therefore, we conclude that the static Jahn-Teller effect is not the symmetry breaking phenomenon which activates the photoluminescence and the peak observed at 1.5 eV. A tell tale signature for this reasoning can be also found in the lack of an apparent zero-phonon line (ZPL) in the experimental spectra.

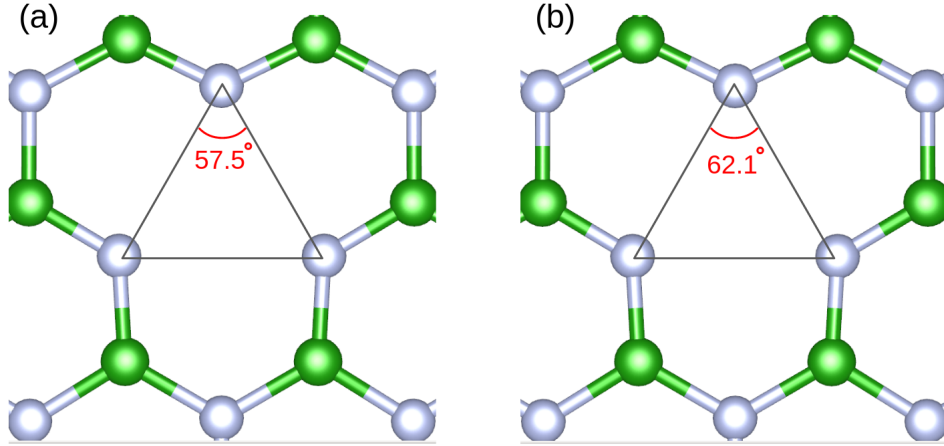


Figure 4.10: This figure shows the two possible geometries in which the structure is distorted by the static Jahn-Teller effect.

4.6 Phonon-assisted luminescence

Once recognised that the symmetry lowering of the Jahn-Teller effect is not the responsible for the activation of the photoluminescence, as it leads to a very small enhancement of the peak at 1.5 eV, we study the effect of the symmetry-break due to the lattice vibrations. Following the work of Cannuccia et al. [36], the contribution of phonons to the emission can be evaluated perturbatively in a frozen-phonon framework, leading to the following expression:

$$I_{ph}(\omega, T) \propto \sum_{\lambda, \nu} \frac{\partial^2 |\Pi_\lambda|^2}{\partial x_\nu^2} f_\lambda^< \left[\delta(\omega - E_\lambda - \omega_\nu) \frac{n_B(\omega_\nu, T)}{2\omega_\nu} + \delta(\omega - E_\lambda + \omega_\nu) \frac{1 + n_B(\omega_\nu, T)}{2\omega_\nu} \right]. \quad (4.1)$$

This equation has a very similar structure to Eq. 2.131. The exciton dipole moment $|\Pi_\lambda|^2$ is now replaced by its derivative with respect to nuclear displacement $\frac{\partial^2 |\Pi_\lambda|^2}{\partial x_\nu^2}$. The symmetry break induced by phonons allows this term to be non-vanishing even though the dipole moment vanishes at the equilibrium position. The derivative of the dipole is a sign that this theory goes beyond the Franck-Condon approximation, which consists in assuming that the dipole moment between ground and excited state is independent on the lattice coordinates, thus allowing this model to work even when the latter fails. The nonequilibrium occupation $f_\lambda^<$ is the same both in Eq. 4.1 and Eq. 2.131, since no emission can take place by unpopulated excitons. Finally the Dirac's δ centered at the exciton energy in Eq. 2.131 is now replaced by two Dirac's δ , corresponding to the cases where an exciton recombines with the creation $\left(\delta(\omega - E_\lambda + \omega_\nu)\right)$ or annihilation $\left(\delta(\omega - E_\lambda - \omega_\nu)\right)$ of a phonon, leading to two peaks at the energies $E_\lambda \pm \omega_\nu$ whose weight depends on the Bose-Einstein distributions $n_B(\omega_\nu, T)$. The derivatives of the exciton dipole moments are calculated using a finite differences approach [110, 111], while the Dirac's delta are broadened with Lorentians of width $\sigma = 0.04$ eV. The phonon-assisted luminescence spectrum calculated in Eq. 4.1 is reported in Fig. 4.12, showing

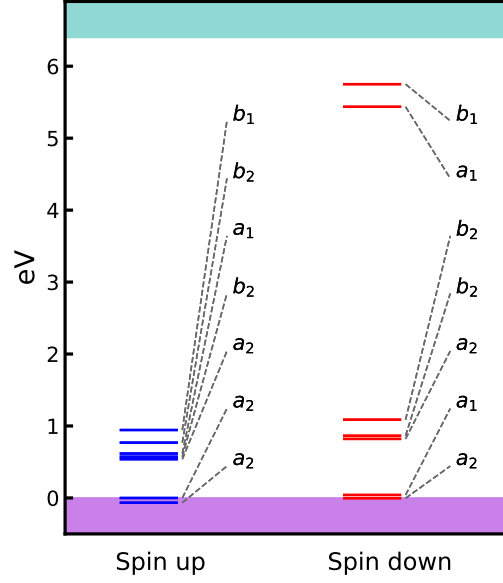


Figure 4.11: Energy levels in one of the Jahn-Teller distorted systems.

a lineshape in very good agreement with experiments. the inset of Fig. 4.12 shows the theoretical and experimental spectra after aligning the ZPLs. The experimental ZPL, 1.64 eV at $T = 295K$, is taken from the supplementary information of Ref. [94]. The theoretical ZPL is assumed to coincide with the energy of the exciton contributing the most to the photoluminescence spectrum (this choice is discussed in detail later). In order to identify the contribution of each exciton to the photoluminescence spectrum it is useful to plot a simplified version of Eq. 4.1:

$$B(\omega) = \sum_{\lambda,v} \frac{\partial^2 |\Pi_\lambda|^2}{\partial x_v^2} f_\lambda^< \delta(\omega - E_\lambda), \quad (4.2)$$

which is obtained by replacing the Dirac δ corresponding to the phonon absorption and emission with a single Dirac δ centered at the exciton energy. This simplified expression has the merit of highlighting the “excitonic backbone” which stands behind the spectra of Fig. 4.12. As shown in Fig. 4.13a this backbone is dominated by a main peak at 1.5 eV (λ_1) and a smaller peak at 1.39 eV (λ_2). The peak at 1.5 eV is distributed into multiple new ones by phonons, whose sum leads to the main peaks of the curve reported in Fig. 4.12. The peak at 1.39 eV in the exciton backbone is instead responsible for the shoulder that appears in the spectra of Fig. 4.12 towards 1.3 eV. The experimental spectrum is asymmetric with a shoulder at low energy which may correspond to the 1.3 eV peak, though the intensity ratio is different. If the phonons had vanishing frequency, almost all the emission would take place at 1.5 eV, which is the energy of the bare exciton contributing most to the photoluminescence spectrum. Taking this as a

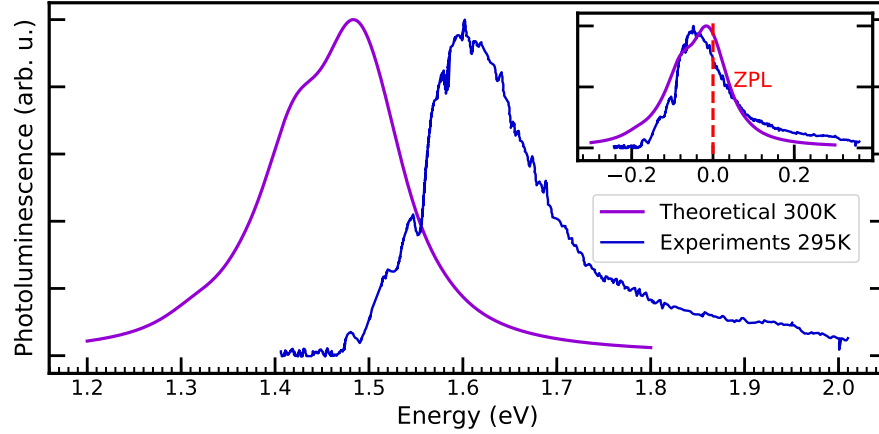


Figure 4.12: Theoretically predicted phonon-assisted luminescence (Eq. 4.1), normalized and compared to experiments [94], at $T=300\text{K}$. The inset shows the theoretical and experimental curves after aligning the ZPLs.

definition of the “zero phonon line” then 1.5 eV can be used for a direct comparison with the ZPL of the Huang-Rhys model. The error of 0.14 eV between the experimental (1.64 eV) and theoretical (1.5 eV) ZPLs witness a good agreement between simulations and experiments. In order to understand which phonon modes couple most strongly with excitons, we plot a simplified version of Eq. 4.1, defining the “exciton-phonon coupling” function:

$$C(\omega) = \sum_{\lambda, \nu} \frac{\partial^2 |\Pi_\lambda|^2}{\partial x_\nu^2} f_\lambda^< \left[\delta(\omega - E_\lambda - \omega_\nu) + \delta(\omega - E_\lambda + \omega_\nu) \right] \quad (4.3)$$

obtained from Eq. 4.1 by removing the Bose-Einstein distributions, which otherwise would affect the amplitudes of the peaks and would depend on temperature. We can see from Fig. 4.13b that the mode that couples most with excitons is $\nu = 120$, of frequency 597 cm^{-1} and symmetry E'' , which is characterised by an out-of-plane oscillation of the first and second nearest neighbours around the vacancy (see Fig. 4.19). The other phonon modes which dominate the exciton-phonon coupling function have similar frequencies to mode $\nu = 120$ and either E'' or A_2'' symmetry (mode $\nu = 24$, characterized by in-phase out-of-plane oscillation of the nitrogen atoms around the vacancy). This ranking is overturned by the Bose-Einstein occupations, especially at high temperatures. If we plot the full contribution of each phonon to the luminescence (as defined in Eq. 4.1), we can see that the factors $\frac{n_B(\omega_\nu, T)}{2\omega_\nu}$ and $\frac{n_B(\omega_\nu, T)+1}{2\omega_\nu}$, which multiply the phonon annihilation and the phonon creation peaks respectively, have two main effects. First of all, at low temperatures, the weight corresponding to the phonon creation tends to zero; therefore, only emission at energies lower than E_λ is expected: Fig. 4.14a shows a vanishing contribution to the emission for energies higher than 1.5 eV at $T=0\text{K}$, while it increases remarkably at $T=300\text{K}$. This growth in importance of the phonon creation term with the temperature leads to a broadening of the PL spectrum, as shown in Fig. 3 of the main paper. Furthermore, as the temperature increases, the low-energy phonons tend to

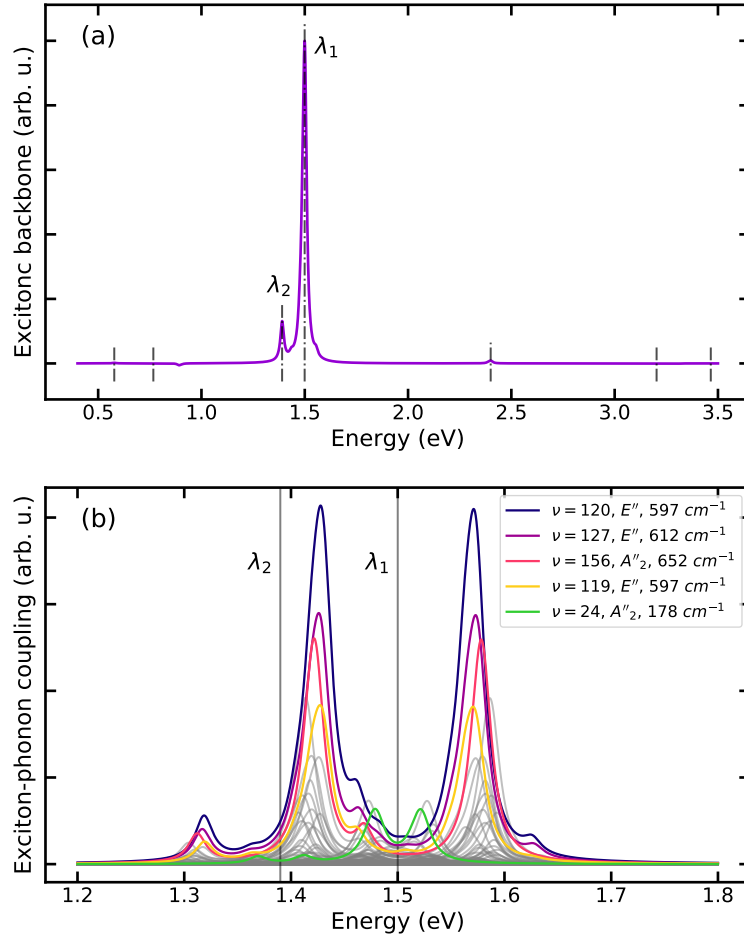


Figure 4.13: Panel (a) shows the exciton backbone, as defined in Eq. 4.2 and normalized. It is clearly dominated by a main excitonic peak at 1.50 eV (λ_1), which is assumed to coincide with the ZPL of the system, while a smaller detached peak appears at 1.39 eV (λ_2). Panel (b) represents instead the exciton phonon coupling function, as defined in Eq. 4.3. The phonon modes that couple most strongly with excitons are enlightened with coloured lines and reported in the legend in decreasing order of contribution, while the other phonon modes are represented with grey lines. Mode $\nu = 24$ is not among those coupling most strongly with excitons; however, its contribution to the PL will become one of the highest when including the Bose-Einstein terms, as shown in the SI.

contribute more than the high-energy ones. This can be observed by considering the increase in importance of mode $\nu = 24$ of frequency 178 cm^{-1} (green line), with respect to mode $\nu = 120$ of frequency 570 cm^{-1} (blue line), leading to the shift towards higher energies of the maximum of the photoluminescence spectrum, as shown in Fig. 4.15. Chen et al. [112] suggest to use defects in 2D hBN as sensitive local thermometers, by exploiting the temperature dependence of the full-width at half-maximum (FWHM) of the PL. We calculate the FWHM for a set of temperatures ranging from 0 to 600 K (Fig. 4.15) and observe an initial very steep increase, due to the combined effects of the increasing contribution of the phonon annihilation term and

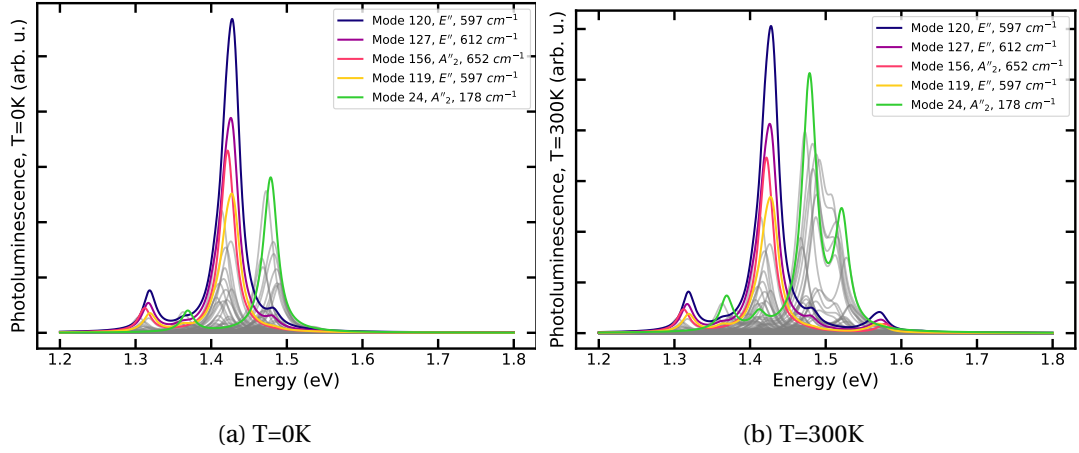


Figure 4.14: Contribution of each phonon to the luminescent emission at $T=0\text{K}$ (panel a) and $T=300\text{K}$ (panel b). The phonon modes which couple most strongly with excitons are enlightened with coloured lines while the other phonon modes are represented with grey lines.

the increasing importance of lower energy modes. Eventually the low frequency (178 cm^{-1}) phonon mode $\nu = 24$ of symmetry A''_2 starts to dominate the PL spectrum. Lower ω lead to smaller energy splittings, and beyond 200K our exciton-phonon coupling model predicts a smooth decrease in the FWHM, but we emphasize that we are neglecting the temperature dependence of the phonon lifetimes as well as multi-phonon effects beyond the perturbation theory used here. These would add to the full spectral peak width, but are of very different nature. Furthermore, the presence of modes with very low frequency ($30\text{--}100\text{ cm}^{-1}$) implies large phonon displacements at high temperatures, suggesting that anharmonic corrections to these phonon modes should be considered when evaluating the photoluminescence, and limiting to low temperatures the validity of the harmonic theory introduced in Ref. [36] and adopted herein. It would be thus more rigorous to compare the theoretical prediction at $T=0\text{K}$ with the experiments at $T=77\text{K}$ (the lowest temperature for which the experimental values are available). This comparison is reported in Fig. 4.16, witnessing again a very good agreement of the lineshapes. A linear fit of the FWHM from 0 to 200K yields a coefficient of 0.343 meV/K , which shows very high sensitivity to temperature variations and suggests that this defect can indeed be used as a nano-scale thermometer.

4.7 Analysis of the phonon modes

Phonons are calculated at the Γ point only using a finite differences approach, using the open source package Phonopy [113] for the generation of the displacements and the calculation of the dynamical matrix and Quantum ESPRESSO for the evaluation of the forces in the displaced configurations. The other points of the Brillouin zone are not considered in the exciton-phonon coupling calculations, as they are characterized by a periodicity that is unphysical for

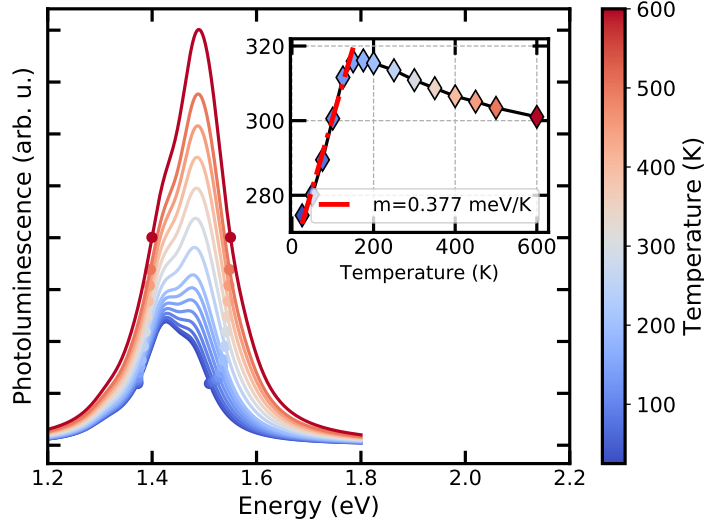


Figure 4.15: Temperature dependence of the phonon-assisted luminescence spectrum. The pair of dots which are plotted for each spectrum show the points where it has a value which is half its maximum (full width at half maximum - FWHM). The inset shows the behaviour of this FWHM (in meV) as a function of temperature. Note that the increase of the curves along the vertical axis is not quantitative, as Eq. 4.1 does not fix the amplitude of the PL spectrum: only the shape and width are relevant.

a defect center.

The 8x8 supercell contains 127 atoms, leading to 381 phonon modes, whose frequencies range from 0 to around 1500 cm^{-1} . Four membrane modes have slightly negative frequencies, and are not included in the exciton-phonon coupling calculations; the instability of these very soft modes lies most likely on the fact that we are neglecting the anharmonicity. The phonons density of states is reported in Fig. 4.17.

It is interesting to analyze the localization of the phonon modes around the defect centers. With this purpose, we calculate a localization factor defined as the sum of the squared modulus of the phonon eigenvector ξ_v for the atoms up to the second nearest neighbors around the vacancy:

$$f^v = \sum_{i \leq 2^{nd} \text{ nn}} |\xi_b(v)|^2. \quad (4.4)$$

The phonons modes with a localization factor higher than 50% are (in decreasing order of f^v) $v=116, 262, 348, 380, 381$. Their radial density of displacement

$$d_v(r) = \sum_b |\xi_b(v)|^2 \delta(|\mathbf{r}_b - \mathbf{r}_{vac}|), \quad (4.5)$$

the radial number density

$$n(r) = \sum_b \delta(|\mathbf{r}_b - \mathbf{r}_{vac}|), \quad (4.6)$$

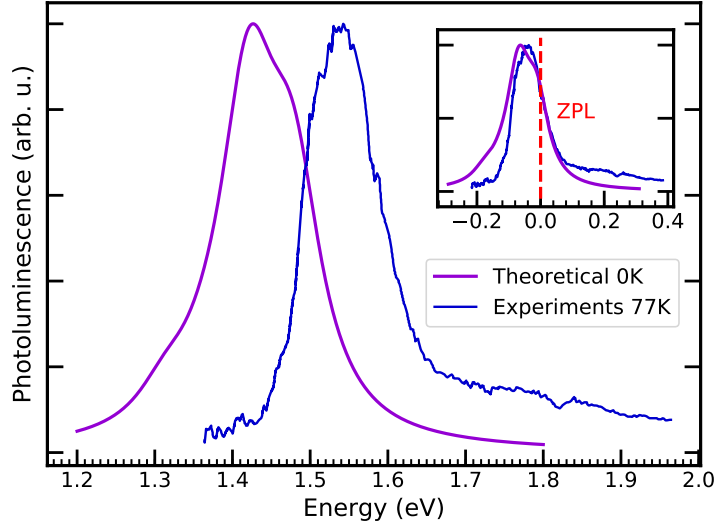


Figure 4.16: Theoretically predicted phonon-assisted luminescence (Eq. 4.1), at $T=0K$, is compared to the experiments of Ref. [94], at $77K$. The inset shows the theoretical and experimental curves after aligning the ZPLs.

and the average density of displacement

$$d_v^{av}(r) = \frac{d_v(r)}{n(r)} \quad (4.7)$$

are represented in Fig. 4.18 (Here the index b refers to the atomic sites and \mathbf{r}_{vac} is the vacancy position). It is easy to see that these very local phonon modes do not coincide with those dominating the exciton-phonon coupling spectrum of Fig. 4.13, although the phonon mode $\nu = 120$ has a localization factor of 40.1%. Therefore we conclude that there is not a trivial relation between exciton-phonon coupling and the localization of the phonons around the vacancy. The phonon mode dominating the exciton-phonon coupling spectrum is $\nu = 120$. As shown in Fig. 4.19, it is characterized by a out-of-plane displacement of the atoms around the vacancy, and is peaked in correspondence of the second nearest-neighbours boron atoms.

4.8 Luminescence spectra via the Van Roosbroeck–Shockley relation

In this section we follow the method suggested in Ref [98] to calculate the photoluminescence spectrum via the Van Roosbroeck–Shockley formula, which relates the stimulated emission to the dielectric constant calculated at the equilibrium:

$$R_{sp}(\omega) \propto \omega^3 \Im \epsilon_M(\omega) e^{-(\hbar\omega - \Delta\mu)/k_B T}. \quad (4.8)$$

This theory coincides with that illustrated in Sec. 4.6 when the amount of the excited electrons is small, with the only difference that, in the former, the population of excitons is assumed

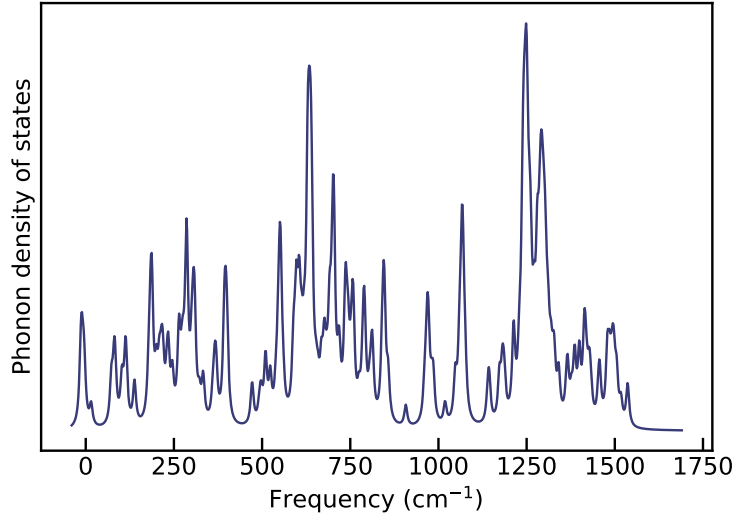


Figure 4.17: Phonon density of states

to be a Bose-Einstein distribution, while in the latter the population of excitons is calculated through Eq. 2.132. We set the chemical potential equal to the exciton energy of 1.77 eV, as it is the most likely to be associated to the observed emission. The comparison with experiments is shown in Fig. 4.20a, witnessing again a good agreement.

4.9 Single-phonon spectrum

Eq. 4.1 can be derived from the adiabatic Williams-Lax approximation [114, 110, 110] under the assumption of single-phonon mode involved. In the presence of multiple phonons there are cross-terms that are not included in Eq. 4.1. It is thus worth checking whether the photoluminescence spectrum maintains its shape when considering a single phonon at a time. In order to do this, we repeat the calculations illustrated in Sec. 4.8 by considering uniquely the contribution of the phonon modes $\nu=120$, which is the most coupled with excitons. The result is reported in Fig. 4.20b. We can see that the shape of the experimental peak is correctly reproduced, even though the theoretical results predict a slow decaying tail which is absent in experiments. It must be stressed that the linewidth of the phonon mode $\nu=120$ has been increased to match that of the experimental peak. Therefore, while the theoretical PL represented in Fig. 4.20a is obtained as the sum of many narrow phonon lines, the spectrum of Fig. 4.20b is made up of a single, broad phonon peak.

Comparison with the Huang-Rhys method

As anticipated in the main text, the most used technique for the calculation of the PL lineshape of defect centers in semiconductors is based on a generalization of the Huang-Rhys (HR)

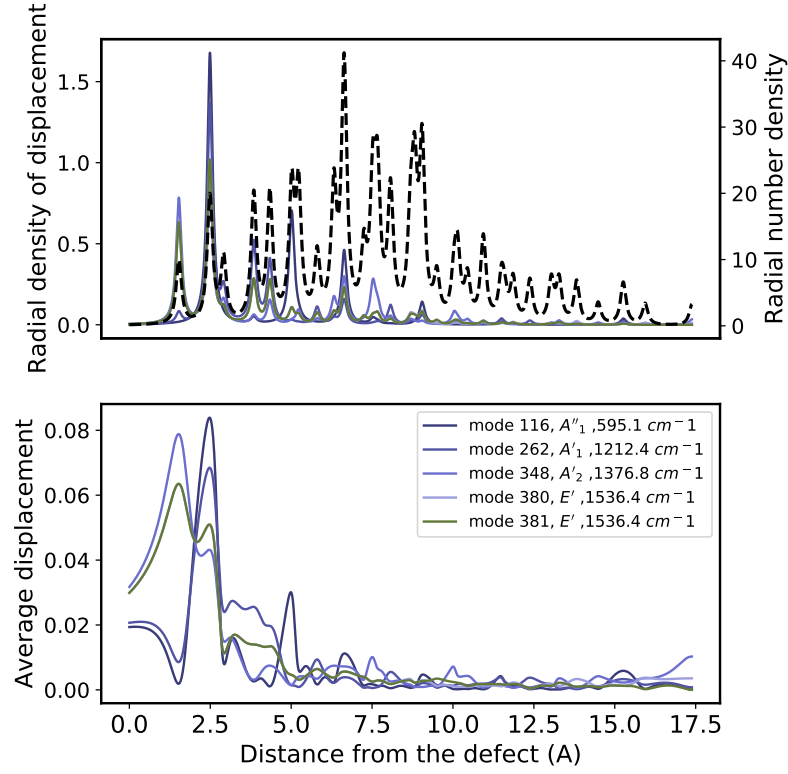


Figure 4.18: The upper panel shows the radial density of displacement $d_v(r)$ as defined in Eq. 4.5 for the phonons with the highest localisation factor f^v . The black dashed line indicates the radial number density. The lower panel represents the average displacement as defined in Eq. 4.7.

model [93]. This technique has been proven to give very good results for 3D defect centers in diamond and silicon carbide [89, 95]. It is based on the assumption that the energy difference between the ground and excited state depends on a fictitious coordinate ξ which is a linear function of the ground state normal modes. The difference between the relaxed position of the atoms in the excited and in the ground state is thus expanded in terms of normal modes to determine the modal coordinates [89]

$$q_v = \sum_{\alpha, b} m_b^{1/2} (R_{b\alpha}^e - R_{b\alpha}^g) e_{b\alpha}(v), \quad (4.9)$$

which are later used to calculate the partial Huang-Rhys factor S_k measuring the coupling of the phonon k with the electrons:

$$S_v = \frac{\omega_v q_v^2}{2\hbar}. \quad (4.10)$$

Here b labels the atoms, α refers to the cartesian component, $R_{b\alpha}^{e/g}$ are the equilibrium positions of the atoms in the excited/ground state and $e_{\alpha i}(v)$ is the phonon eigenvector. The

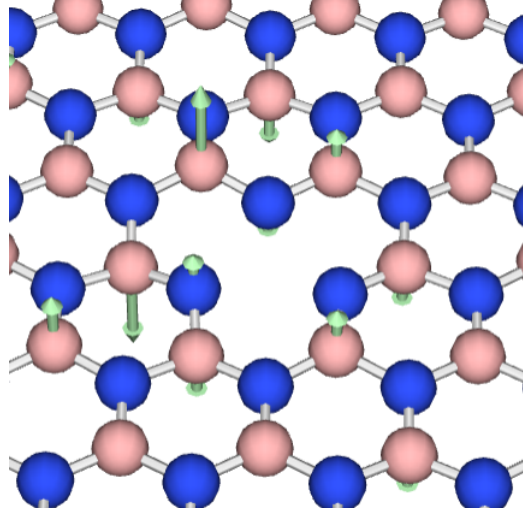


Figure 4.19: Representation of the eigenvector of the phonon mode $\nu = 120$.

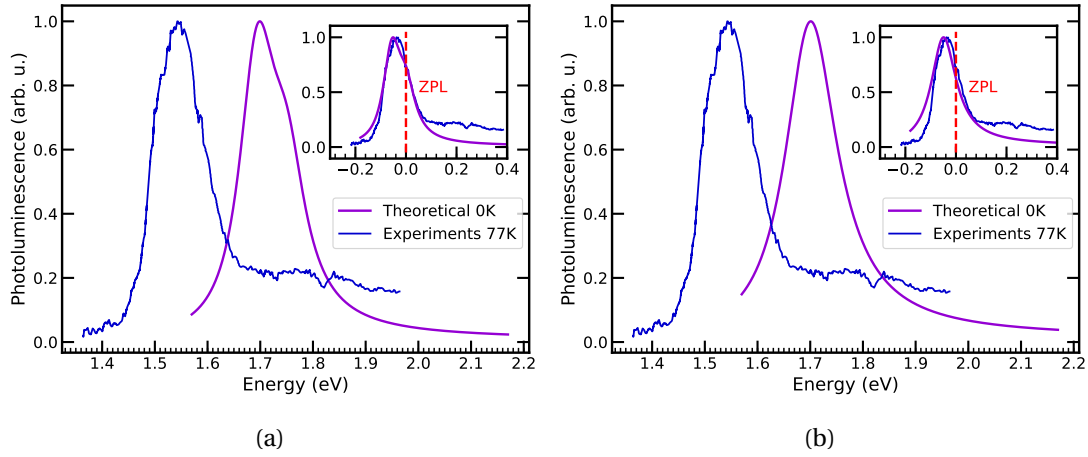


Figure 4.20: Panel (a) shows the phonon-assisted PL spectrum via the Van Roosbroeck-Shockley relation, obtained considering the contribution of all the phonon modes. Panel (b) instead shows the PL spectrum obtained when considering uniquely the contribution of the phonon mode $\nu=120$. In the latter case, the linewidth of the phonon mode has been broadened in order to match that of the experimental peak.

electron-phonon coupling function

$$S(t) = \int_0^\infty \sum_{\nu} S_{\nu} \delta(\hbar\omega - \hbar\omega_{\nu}) e^{-i\omega t} d(\hbar\omega) \quad (4.11)$$

is used to calculate the generating function

$$G(t) = e^{S(t) - S(0)} \quad (4.12)$$

(see Ref. [91] for a finite temperature treatment) whose Fourier transform is proportional to the PL lineshape:

$$L(E_{ZPL} - \hbar\omega) = \omega^3 \int_{-\infty}^{\infty} \frac{1}{2\pi} G(t) e^{i\omega t - \gamma|t|} dt. \quad (4.13)$$

Here γ and E_{ZPL} are respectively the broadening and the energy of the zero-phonon line. The former is usually assumed, while the latter is determined through constrained DFT or quantum chemistry calculations. The starting point of the theory summarized above is the following expression for the absolute intensity of the emission [93, 89]:

$$I(\hbar\omega) = \frac{n_D \omega^3}{3\epsilon_0 \pi c^3 \hbar} |\mu_{eg}|^2 \sum_m |\langle \chi_{gm} | \chi_{e0} \rangle|^2 \delta(E_{ZPL} - E_{gm} - \omega \hbar), \quad (4.14)$$

where n_D is the refractive index, and $|\mu_{eg}|$ is the optical dipole moment between ground and excited states. The main assumption behind the Huang-Rhys theory is that $|\mu_{eg}|$ is not affected by phonons (Frank-Condon approximation). This allows to take $|\mu_{eg}|$ out of the summation in Eq. 4.14. As we will show later, this assumption limits the predictivity of the theory in systems such as V_B^- in which this dipole is vanishing for symmetry. In the MBPT, instead, phonon dependence of the optical dipole moments is correctly taken into account, as witnessed by the terms $\frac{\partial^2 |\Pi_A|^2}{\partial x_v^2}$ in Eq. 2 of the main text.

As shown by Eq. 4.10, only the phonon modes with non-vanishing modal coordinate q_k contributes to the PL lineshape of the Huang-Rhys method. Now, both Refs. [90, 94] agree that the observed luminescence is associated to the transition between the many-body states $(1)^3 E'' \rightarrow (1)^3 A'_2$, which corresponds to the transition between the single-particle states $e' \rightarrow a''_2$ of the main text. However, the relaxed geometry of the state $(1)^3 E''$ remains flat even when considering the Jahn-Teller distortion (i.e. all the atoms have 0 displacement in the out-of-plane direction). This has the fundamental consequence that $q_k = 0$ for all the out-of-plane phonon modes: therefore, these modes do not contribute to the HR luminescence. The formalism presented in the main text is beyond the Franck-Condon approximation, and instead predicts that the out-of-plane phonon modes are those affecting most the photoluminescence. It is instructive to calculate the PL with the MBPT approach presented in the main text and excluding the contribution of the phonons of symmetry A'_1 , A''_2 and E'' (i.e. those phonons which do not contribute to the PL in the Huang-Rhys method). The result is shown in violet dashed line in Fig. 4.21, and compared with the calculations of the PL through the HR method from Ref. [90] (represented in green solid line). In both cases, the spectrum is much broader than the experimental one [94], represented in solid blue line. The result is improved dramatically when the contribution of phonons of all the symmetries is considered when calculating the PL with the MBPT approach, leading to the curve represented in solid violet line (and reported in Fig. 4.12). We thus conclude that the PL is dominated by the phonon modes which are odd with respect to the mirroring with the plane of the 2D material. This explains the failure of the HR method in reproducing the PL lineshape of the charged B vacancy.

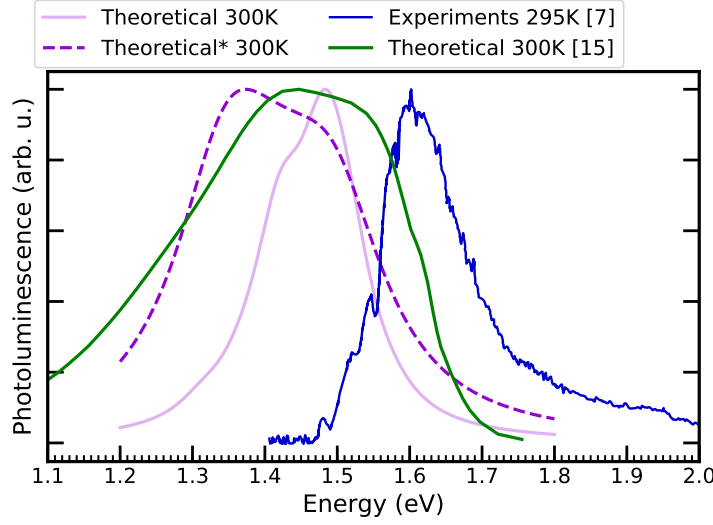


Figure 4.21: The violet dashed line is obtained from the MBPT approach of the main text when excluding the contribution of the phonon modes of symmetry A_1'' , A_2'' and E'' . This curve is compared to the result from the HR method of Ref. [90], represented in green solid line. The solid violet line represents the PL calculated through the MBPT approach when including the contribution of all the phonons, while the solid blue curve represents the experimental PL from Ref. [94].

4.10 Limitations and future perspectives

Our theory can be seen as a particular case of the Herzberg-Teller theory [95] in which the relaxation of the excited state geometry is neglected. This assumption is valid in cases where the reorganization energy associated to the geometry variation of the excited state is small. The reorganization energies extrapolated from the experimental spectra [94] are of the order of tens of meV, suggesting that this approximation is accurate for the V_B^- . However, in other defects, the reorganization energy may be higher, affecting both the position of the ZPL and the shape of the spectrum. This renormalization of the ZPL energy can be computed either perturbatively by including the electron-phonon diagrams in the self-energy [115], or even non-perturbatively, by performing a single shot calculation at the Zacharias-Giustino point [110, 111]. The multi-phonon replica in the photoluminescence spectrum caused by the relaxation of the geometry in the excited state requires development of the theory, which is the object of ongoing work. This information is contained in the electron-phonon matrix elements: in an independent-particle picture,

$$\Delta q_v = \sqrt{\frac{2\hbar}{\omega_v}} \frac{g_{vv} - g_{cc}}{\omega_v \hbar}, \quad (4.15)$$

thus allowing a generalization of our theory within a MBPT framework.

5 Electron-phonon coupling through finite differences

The knowledge of the electron-phonon coupling is fundamental for the determination of the properties of the defect centers and their dependence on temperature. The interaction between electrons and phonons is responsible for a series of phenomena, such as the broadening of the peaks in the photoluminescence spectrum, the relaxation of the geometry of the excited states, which causes the appearance of the multi-phonon replica in the spectrum, and the band-gap renormalization, which leads to a red-shift of the emission frequency. Therefore the prediction of EP coupling from first principles is very important for an accurate description of the optical properties of the defect centers.

The most used framework for the calculation of the EP coupling coefficient is the density functional perturbation theory (DFPT) [116, 115, 117, 118]. The striking advantage of this theory is that it allows to calculate the phonon dispersions and electron-phonon coupling coefficients for any point of the Brillouin zone, without the need to commensurate the size of the supercell to the phonon momentum. Its drawback is that the computational cost scales very quickly with the number of atoms, thus making the calculation of the vibrational properties of defects extremely expensive. On the contrary, the finite differences technique for the calculation of phonons and EP coupling is considerably cheaper than DFPT for calculations at the Γ point of the Brillouin zone, for which it is not necessary to use a supercell, but its computational cost grows quickly for phonon momenta which require big supercells. Since defects behave as molecules immersed in a crystal environment, the vibrational properties should be determined only in the Γ point of the Brillouin zone. This makes the finite differences technique a preferential tool for the study of the defect centers.

The finite differences technique has two further advantages with respect to DFPT. First of all, it can be used in conjunction with any electronic structure solver, which implies that systems with weak and strong electronic correlations can be treated on the same footing. The second is the possibility to incorporate easily electron-phonon interaction terms beyond the lowest order in perturbation theory. Although softwares for the finite differences calculation of phonons exist, such as the open-source package Phonopy [113], there is no such a program to determine the EP coupling through finite differences.

In the following, we develop a technique that allows to calculate the EP through finite dif-

ferences as a *simple postprocessing of the phonons calculation*. This is possible because this technique exploits *the very same displacements necessary to determine the vibrational properties through finite differences*. We can thus set up an efficient, fully automated workflow for the determination of phonon and electron phonon coupling for 2D and 3D crystals.

5.1 Finite differences

Following Eq. 2.160, once the phonons are calculated, the calculation of the EP matrix elements requires only the evaluation of the bracket

$$\langle \psi_i | \frac{\partial V}{\partial u_{b\alpha}} | \psi_j \rangle . \quad (5.1)$$

From now on, we adapt our formalism to the Γ -only calculations, for which our theory is developed. Therefore we drop the dependence on the \mathbf{k} -point \mathbf{k} , the phonon momentum \mathbf{q} , and the lattice vector \mathbf{l} . In a finite differences approach, the bracket of Eq. 5.1 can be calculated as

$$\langle \psi_i | \frac{\partial V}{\partial u_{b\alpha}} | \psi_j \rangle \simeq \langle \psi_i | \frac{V(u_{b\alpha}) - V(0)}{u_{b\alpha}} | \psi_j \rangle . \quad (5.2)$$

$V(u_{b\alpha})$ is the KS potential of a crystal where the atom b is displaced from the equilibrium position of an amount $u_{b\alpha}$, while $V(0)$ and $|\psi_i\rangle$ are respectively the KS potential and wavefunctions of the crystal at equilibrium. In principles, the determination of the EP matrix elements requires $3N$ displacements, thus leading to a very large amount of *scf* calculations for systems with many atoms. In the following, we devise a strategy aimed at exploiting the symmetries of the material to reduce significantly the number of displacements necessary to calculate the EP coupling. Our goal is to use the very same amount of *scf* calculations required to calculate phonons, thus turning the determination of EP coupling into a simple *postprocessing* of the phonon calculations. This strategy exploits a different treatment for the derivatives of the local and non-local parts of the Kohn-Sham potential, as illustrated in the following.

5.1.1 Non-local part of the KS potential

The non-local part of the KS potential derives from the non-local component of the pseudopotentials [119]. The implementation is carried out for norm-conserving pseudopotentials [120, 121] in the fully-separable form [119], but can be easily generalized to the ultrasoft pseudopotentials [122]. For the former, this non-local component reads

$$V_{NL} = \sum_{\beta} \sum_{m=-l(\beta)}^{l(\beta)} |Y_{lm}\beta\rangle D_{\beta} \langle Y_{lm}\beta| , \quad (5.3)$$

where the β s are short-ranged radial functions, with angular momentum $l(\beta)$, and Y_{lm} are spherical harmonics. This potential is centered at the position \mathbf{R} of the atom to which it

corresponds. It's expectation value must be computed as

$$\langle \psi_i | V_{NL} | \psi_j \rangle = \int d^3\mathbf{x} d^3\mathbf{x}' \psi_i(\mathbf{x})^* \langle \mathbf{x} - \mathbf{R} | V_{NL} | \mathbf{x}' - \mathbf{R} \rangle \psi_j(\mathbf{x}') . \quad (5.4)$$

Since we know the analytic expression of such a non-local part, we can calculate its derivatives efficiently without the need to displace the atoms [116]. First of all, we express the ket $|Y_{lm}\beta\rangle$ in reciprocal space by exploiting the identity

$$e^{-i\mathbf{G}\cdot\mathbf{x}} = 4\pi \sum_{lm} (-i)^l j_l(|G||r|) Y_{lm}(\hat{\mathbf{G}}) Y_{lm}^*(\hat{\mathbf{x}}) , \quad (5.5)$$

where j_l is the l -order spherical Bessel function, and we have expressed \mathbf{G} and \mathbf{x} in polar coordinates, indicating with $|G|$ and $|r|$ their moduli and with $\hat{\mathbf{G}}$ and $\hat{\mathbf{x}}$ the unit vectors identifying their angles. Therefore, the Fourier transform of $|Y_{lm}\beta\rangle$ reads

$$\langle \mathbf{G} | Y_{lm}\beta \rangle = \int d\Omega dr \frac{e^{-i\mathbf{G}\cdot\mathbf{x}}}{\sqrt{V}} Y_{lm}(\Omega) r^2 \beta(r) = \frac{4\pi}{\sqrt{V}} (-i)^l Y_{lm}(\hat{\mathbf{G}}) \int_0^\infty dr r^2 j_l(|G|r) \beta(r) \quad (5.6)$$

The derivative of the bracket $\langle Y_{lm}\beta | \psi_j \rangle$ with respect to \mathbf{R} is thus

$$\frac{\partial}{\partial \mathbf{R}} \langle Y_{lm}\beta | \psi_j \rangle = \sum_{\mathbf{G}} \langle Y_{lm}\beta | \mathbf{G} \rangle i\mathbf{G} e^{i\mathbf{G}\cdot\mathbf{R}} \langle \mathbf{G} | \psi_j \rangle . \quad (5.7)$$

Thanks to this relation, we can finally calculate

$$\langle \psi_i | \frac{\partial V_{NL}}{\partial \mathbf{R}} | \psi_j \rangle = \sum_{\beta} \sum_{m=-l(\beta)}^{l(\beta)} D_{\beta} \left[\left(\frac{\partial}{\partial \mathbf{R}} \langle \psi_i | Y_{lm}\beta \rangle \right) \langle Y_{lm}\beta | \psi_j \rangle + \langle \psi_i | Y_{lm}\beta \rangle \left(\frac{\partial}{\partial \mathbf{R}} \langle Y_{lm}\beta | \psi_j \rangle \right) \right] . \quad (5.8)$$

The bracket in Eq. 5.8 can be efficiently computed for all the atoms exploiting the ground state wavefunctions and the information contained in the pseudopotentials, therefore the non-local part of the KS potential does not require a finite differences treatment.

5.1.2 Local part of the KS potential

Contrary to the non-local term, the local part of the KS potential depends on the screened response of the electrons to the perturbation caused by the displacement of the atoms, therefore its derivatives need to be calculated through finite differences. The local KS potential can be expressed as a function of the coordinates of the ions, $\mathbf{R}_1, \mathbf{R}_2, \dots, \mathbf{R}_N$ and the electronic coordinate \mathbf{r}

$$V = V(\mathbf{R}_1, \mathbf{R}_2, \dots, \mathbf{R}_N, \mathbf{r}) . \quad (5.9)$$

The finite differences calculation of the phonons requires to carry out *scf* calculations for a set of $n < 3N$ displacements. The question is: how can we calculate the gradient of the KS potential at each atomic site by exploiting the information that we already know thanks to the phonon calculation on this set of displacements? We can divide the problem into two steps.

1. Calculate the gradient with respect to the coordinates of an atom that is displaced during the phonon calculations;
2. Calculate the gradient with respect to the coordinates of an atom that is no displaced during the phonon calculations;

We will address these points separately.

Case 1. Suppose to calculate explicitly the KS potential in the crystal when the first atom is displaced along the direction λ . This allows determining the directional derivative

$$\frac{dV}{d\lambda} \simeq \frac{V(\mathbf{R}_1^0 + \lambda|u|, \dots, \mathbf{R}_N^0, \mathbf{r}) - V(\mathbf{R}_1^0, \dots, \mathbf{R}_N^0, \mathbf{r})}{|u|}, \quad (5.10)$$

where we the superscript 0 is used to refer to the equilibrium positions. Let us consider the representation of the symmetry group of the crystal on the space of 3x3 matrices, and label its generic element with \hat{P} . If there exist some \hat{P} such that

$$\hat{P}\mathbf{R}_1^0 = \mathbf{R}_1^0, \quad (5.11)$$

then

$$V(\mathbf{R}_1^0 + \hat{P}\lambda|u|, \dots, \mathbf{R}_N^0, \mathbf{r}) = V(\mathbf{R}_1^0 + \lambda|u|, \dots, \mathbf{R}_N^0, \hat{P}^1\mathbf{r}). \quad (5.12)$$

This means that once we find an *autosymmetry* of the atom 1, (i.e. symmetry that maps the atom in itself), we can calculate the derivative in the direction $\mu = \hat{P}\lambda$ by simply rotating the derivative in the direction λ according to Eq. 5.12. The problem simply reduces to search for the *autosymmetries* of the atom 1, until the directional derivative in three independent directions λ, μ, ν is known. If one displacement is required to calculate the phonons, then the two other displacements are obtained by looking for the autosymmetries. If instead two displacements are required for the phonon calculations, an autosymmetry will give the third independent displacement. In any case, no further *scf* calculation must be done, as it is shown at the end of this section. The gradient at the atom 1 can be simply computed by solving the equation

$$\begin{pmatrix} \lambda_1 & \lambda_2 & \lambda_3 \\ \mu_1 & \mu_2 & \mu_3 \\ \nu_1 & \nu_2 & \nu_3 \end{pmatrix} \begin{pmatrix} \frac{dV}{dx} \\ \frac{dV}{dy} \\ \frac{dV}{dz} \end{pmatrix} = \begin{pmatrix} \frac{dV}{d\lambda} \\ \frac{dV}{d\mu} \\ \frac{dV}{d\nu} \end{pmatrix}. \quad (5.13)$$

For example, Fig. 5.1 illustrates, for a hexagonal lattice, how it is possible to exploit the knowledge of the first derivative in one direction to calculate the directional derivative along all the other equivalent directions.

Case 2. This case is very similar to the former. Suppose we want to calculate the derivatives of atom 2, which is equivalent by symmetry to atom 1. This means that there exist operators \hat{P} such as

$$\mathbf{R}_2^0 = \hat{P}\mathbf{R}_1^0. \quad (5.14)$$

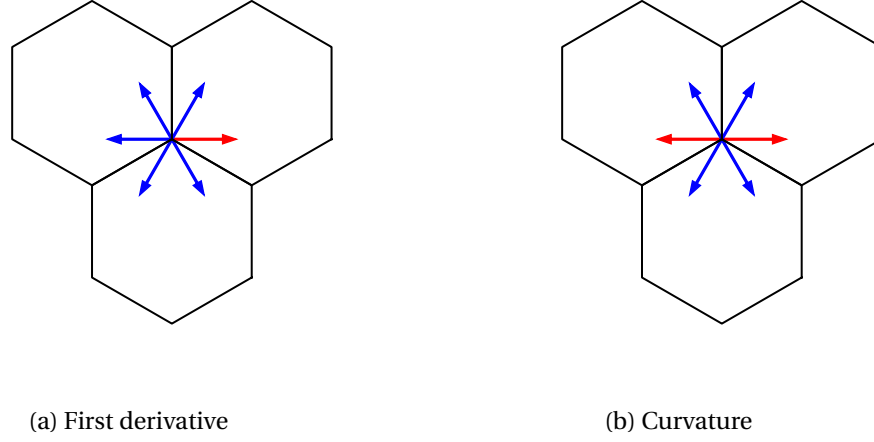


Figure 5.1: The knowledge of the first derivative of the potential in the direction marked with red arrow in panel (a) allows to determine the first derivatives of the potentials along the directions marked with blue arrows. Equivalently, the knowledge of the curvature on the direction marked by the pair of red arrows in panel (b) allows to determine the curvature along the directions marked by the pairs of blue arrows.

Therefore

$$V(\mathbf{R}_1^0, \mathbf{R}_2^0 + \hat{P}\lambda|u|, \dots, \mathbf{R}_N^0, \mathbf{r}) = V(\mathbf{R}_1^0 + \lambda|u|, \mathbf{R}_2^0, \dots, \mathbf{R}_N^0, \hat{P}^1\mathbf{r}). \quad (5.15)$$

We can thus calculate the gradient at atom 2 by rotating appropriately the derivatives at atom 1.

We can now prove that it is possible to calculate both phonons and EP coupling using the same set of *irreducible displacements*. This can be easily done using similar arguments to those expressed before: a *scf* calculation for the configuration in which atom j is displaced along the direction λ allows to calculate the force F_i acting on the atom i , for all the atoms ($i = 1, \dots, N$).

$$\mathbf{F}_i(\mathbf{R}_j^0 + \lambda|u|, \dots, \mathbf{R}_N^0, \mathbf{r}) \simeq \frac{\partial \mathbf{F}_i}{\partial u_{j\lambda}}(\mathbf{R}_1^0, \mathbf{R}_2^0, \dots, \mathbf{R}_N^0)|u_{j\lambda}|, \quad \forall i = 1, \dots, N. \quad (5.16)$$

For any autosymmetry \hat{P} of the atom j it holds

$$\mathbf{F}_i(\mathbf{R}_j^0 + \hat{P}\lambda|u|, \dots, \mathbf{R}_N^0) = \hat{P}^1 \mathbf{F}_i(\mathbf{R}_j^0 + \lambda|u|, \dots, \mathbf{R}_N^0), \quad (5.17)$$

while for an atom k equivalent (Eq. 5.14) to the atom j

$$\mathbf{F}_i(\mathbf{R}_j^0, \mathbf{R}_k^0 + \hat{P}\lambda|u|, \dots, \mathbf{R}_N^0) = \hat{P}^1 \mathbf{F}_i(\mathbf{R}_j^0 + \lambda|u|, \mathbf{R}_k^0, \dots, \mathbf{R}_N^0), \quad (5.18)$$

Given the perfect analogy between Eqs. 5.12-5.15 and Eqs. 5.17-5.18 we conclude that the set of displacements which allows to calculate the interatomic-force constant matrix for any couple of atoms allows also to calculate also the EP coupling matrix elements.

5.2 Second derivatives

In order to calculate the phonons with a *second order* finite differences scheme, it is necessary to know the value of the forces for a displacement \mathbf{u} and its inverse $-\mathbf{u}$. We can exploit this *information*, which is stored into the *scf* calculation necessary for the calculation of phonons, to evaluate the second derivatives of the KS potential and their brackets with the KS states:

$$\langle \psi_i | \frac{\partial^2 V}{\partial u_{b\alpha} \partial u_{b'\beta}} | \psi_j \rangle . \quad (5.19)$$

The number of derivatives is $\sim 9N^2/2$, and becomes extremely big for defect supercells. Fortunately, since the first derivatives are very localised around the atoms which are displaced, we can safely assume that the second derivatives with respect to the displacement of two different atoms are much smaller than the derivatives where the same atom is displaced. In other words, the second derivative matrix is diagonal with respect to the atoms label (but not their cartesian coordinates).

$$\langle \psi_i | \frac{\partial^2 V}{\partial u_{b\alpha} \partial u_{b'\beta}} | \psi_j \rangle = \langle \psi_i | \frac{\partial^2 V}{\partial u_{b\alpha} \partial u_{b\beta}} | \psi_j \rangle \delta_{bb'} . \quad (5.20)$$

This not only reduces drastically the number of derivatives to calculate, from $\mathcal{O}(N^2)$ to $\mathcal{O}(N)$, but also allows to suggest a simple scheme to calculate the second derivatives. In fact, it is necessary to compute the curvature along six independent directions in order to determine the whole Hessian \mathbf{H} with respect to the coordinates of one atom. This is simply shown starting from the relation

$$\frac{\partial^2 V}{\partial \lambda \partial \mu} = \boldsymbol{\lambda} \cdot \mathbf{H} \cdot \boldsymbol{\mu} , \quad (5.21)$$

where $\boldsymbol{\lambda}$ and $\boldsymbol{\mu}$ are two directions which are not necessary orthogonal. By imposing the condition 5.21 for 6 independent unit vectors $\boldsymbol{\lambda}_i$, we obtain the following equation:

$$\begin{pmatrix} \lambda_{1x}^2 & \lambda_{1y}^2 & \lambda_{1z}^2 & \lambda_{1x}\lambda_{1y} & \lambda_{1x}\lambda_{1z} & \lambda_{1y}\lambda_{1z} \\ \lambda_{2x}^2 & \lambda_{2y}^2 & \lambda_{2z}^2 & \lambda_{2x}\lambda_{2y} & \lambda_{2x}\lambda_{2z} & \lambda_{2y}\lambda_{2z} \\ \lambda_{3x}^2 & \lambda_{3y}^2 & \lambda_{3z}^2 & \lambda_{3x}\lambda_{3y} & \lambda_{3x}\lambda_{3z} & \lambda_{3y}\lambda_{3z} \\ \lambda_{4x}^2 & \lambda_{4y}^2 & \lambda_{4z}^2 & \lambda_{4x}\lambda_{4y} & \lambda_{4x}\lambda_{4z} & \lambda_{4y}\lambda_{4z} \\ \lambda_{5x}^2 & \lambda_{5y}^2 & \lambda_{5z}^2 & \lambda_{5x}\lambda_{5y} & \lambda_{5x}\lambda_{5z} & \lambda_{5y}\lambda_{5z} \\ \lambda_{6x}^2 & \lambda_{6y}^2 & \lambda_{6z}^2 & \lambda_{6x}\lambda_{6y} & \lambda_{6x}\lambda_{6z} & \lambda_{6y}\lambda_{6z} \end{pmatrix} \begin{pmatrix} \frac{\partial^2 V}{\partial x^2} \\ \frac{\partial^2 V}{\partial y^2} \\ \frac{\partial^2 V}{\partial z^2} \\ \frac{\partial^2 V}{\partial x \partial y} \\ \frac{\partial^2 V}{\partial x \partial z} \\ \frac{\partial^2 V}{\partial y \partial z} \end{pmatrix} = \begin{pmatrix} \frac{\partial^2 V}{\partial^2 \lambda_1} \\ \frac{\partial^2 V}{\partial^2 \lambda_2} \\ \frac{\partial^2 V}{\partial^2 \lambda_3} \\ \frac{\partial^2 V}{\partial^2 \lambda_4} \\ \frac{\partial^2 V}{\partial^2 \lambda_5} \\ \frac{\partial^2 V}{\partial^2 \lambda_6} \end{pmatrix} \quad (5.22)$$

whose solution gives the components of the Hessian.

5.3 Workflow

The workflow for the calculation of the EP matrix elements is very simple, and is illustrated in Fig. 5.2. The first step consists in calculating phonons. This is done by generating a set

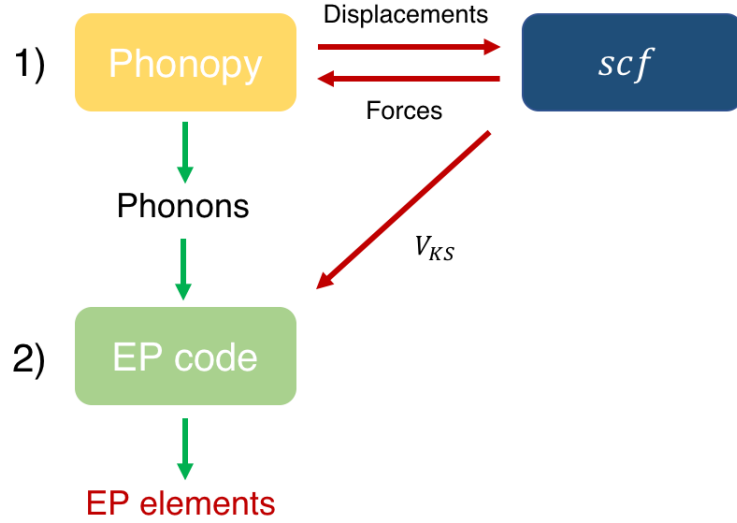


Figure 5.2: Workflow for the calculation of EP matrix elements through finite differences.

of displacements with Phonopy and performing a *scf* calculation for each of them, using any first-principles code. The forces for each displaced configuration are then collected by Phonopy, which uses them to determine the phonon frequencies and eigenvectors.

The determination of the EP matrix elements requires the knowledge of the KS local potential in real space for each *scf* calculations. This can be determined as a simple post processing operation (or printed at the end of the *scf* calculation).

The EP coupling can be determined for a selected range of bands (e.g. the defect energy levels), thus reducing even further the computational burden.

5.4 Comparison with DFPT

The finite differences EP code is written in Python, and has been tested by comparing the EP matrix elements in Γ with those calculated through DFPT for a set of semiconductors, both polar (silicon carbide and 2D hBN) and non-polar (graphene, diamond, silicon). The dependence of the EP matrix elements on the gauge of the wavefunctions has been removed by symmetrizing the EP elements as suggested in Ref. [115]. The results are shown in Fig. 5.3, proving that the implementation is correct and the two methods are in agreement. Further useful checks can be carried by simply comparing the KS eigenvalue of the displaced configurations to those predicted from first-order perturbation theory. For a non-degenerate state, the variation of energy due to the perturbation

$$H_1 = \frac{\partial V}{\partial u_{b\lambda}} u_{b\lambda} \quad (5.23)$$

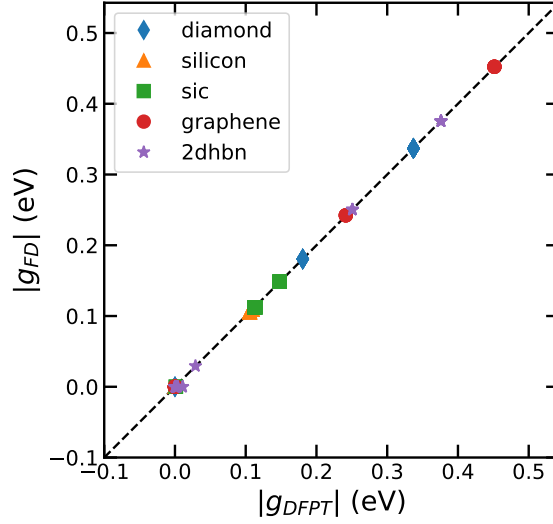


Figure 5.3: EP elements calculated through DFPT (x axis) are compared to those determined through finite differences (y axis). In both cases, the elements have been symmetrized following the criterion suggested in Ref. [115], in order to remove the gauge-dependence. These values may not be fully converged, as the scope of the analysis is just to check the matching between the two methods. We can see clearly that the points align on the bisector (dashed line), showing that the DFPT and the finite differences techniques lead to the same results.

reads

$$\Delta \varepsilon_i = \langle \psi_i | H_1 | \psi_i \rangle, \quad (5.24)$$

while for degenerate states the variation of the eigenvalues is obtained by diagonalizing the following overlap matrix,

$$\Delta \varepsilon_{1,2,\dots} = \text{Eig} \left\{ H \text{ s.t. } H_{ij} = \langle \psi_i | H_1 | \psi_j \rangle \right\}, \quad (5.25)$$

where $|\psi_{i/j}\rangle$ belongs to the degenerate subspace.

One might think to use Eqs. 5.24-5.25 as definition for the calculation of the bracket 5.1. This would work well for non-degenerate states, but would face the following limitations for the degenerate ones. First of all, it is necessary to understand which states are degenerate. This can be done by looking at the difference between the energy levels, but may be tricky for systems with a lot of atoms in the unitcell, since the levels are very close to each other. Furthermore, the perturbed wavefunctions $|\psi'\rangle$ may be rotated of a finite quantity with respect to the unperturbed ones $|\psi\rangle$, thus requiring the calculation of the overlap matrix $\langle \psi' | \psi \rangle$. Finally, the perturbed energies would be available only for the displaced configurations for which the self-consistent calculations are carried. It would thus be necessary to devise a scheme for the rotation of the brackets, which should take into account the symmetry of the wavefunctions as well.

5.5 Future perspectives

The workflow described in the previous sections can be used for the calculation of EP coupling for defects in 3D and 2D crystals. The knowledge of the EP matrix elements will be used go beyond the finite-differences approach to the prediction of optical properties presented in Chap. 4, allowing to calculate e.g. the renormalization of the defect energy levels and the linewidth of the PL spectrum, and assess their dependence on temperature. It will also account to take into account the effects of the relaxation of the excited states geometry both in the position of the PL spectrum and the presence of multi-phonon replica.

6 Green's function on a current quantum processor

In the following we report our work recently published [123], about the design of quantum algorithm for the calculation of the Green's function. This work is done in collaboration with IBM-Zurich under the framework of the EPFLInnovators program, founded by the European union's Horizon 2020 research and innovation program under the Marie Skłodowska-Curie grant agreement No 754354.

6.1 Introduction

The many-body Green's function of an interacting quantum system is a central quantity in many state-of-the-art techniques for solid state physics and quantum chemistry. In the first part of this Thesis, the Green's function theory has been used to calculate the phonon-assisted optical properties of defect centers in semiconductors, but many other important applications are possible, such as the study of electronic and thermal transport in crystals as well as the ultrafast dynamic of electrons. Furthermore, dynamical mean-field theory (DMFT) [124] plays a central role in the study of strongly correlated materials. As shown in Chapter 2, the exact many-body Green's function possesses many important properties. First, it can be used to calculate the expectation value of observables (see Eqs. 2.44-2.46), and the poles of its Fourier transform correspond to the excitation energies. Finally, the retarded Green's function is connected to the exact linear response of the system.

The computation of the exact Green's function on a classical computer is known to become exponentially hard when increasing the size of the system under study, as it requires the knowledge of the exact ground state. It becomes thus attractive to devise algorithms for the calculation of Green's functions on quantum computers, since even though quantum algorithms make use of the many-electron wavefunction to evaluate the Green's functions, there is no actual need of measuring its components. At variance with equivalent classical approaches based on the Lehman representation, the wavefunction is first mapped to the quantum circuit, then optimized and finally used – without explicitly storing its full classical description obtained, for instance, through state tomography – to probe the Green's function. Several works presented in the literature are based on the quantum phase estimation [125,

126, 127, 128] or on the Suzuki-Trotter expansion of the propagator [129, 130, 131]. However, both of these techniques are known to be expensive in terms of circuit depth and number of controlled operations, and therefore are not suitable for near-term quantum computers. One of the first efforts to design an affordable quantum algorithm for the calculation of the Green's function goes back to Endo et al. [132]. In their work these authors suggest two alternative techniques, one in the frequency domain and the other in the time domain. The former exploits the Lehman representation and calculates the excitation energies of the system through the subspace-search variational quantum eigensolver (SSVQE) [133], and an alternative approach has been recently presented in Ref. [134], where the SSVQE is replaced with a generalized quantum equation of motion (qEOM) technique [135] for charged excitations. The second approach of Ref. [132] is based on the real time evolution of a system through the variational quantum simulation (VQS) technique [136], which requires shallower quantum circuits compared to the Suzuki-Trotter expansion of the propagator. The algorithm of Ref. [132] requires the adoption of a variational form U which can accurately describe the time evolution of both the ground state of the system $|\psi\rangle$ and a state of the form $|P_i\psi\rangle$ (where P_i is a n -qubit Pauli operator) with the same choice of parameters. However, as shown in Sec. 6.3, it is quite difficult to find an empiric variational form satisfying this requirement. In addition, such variational form is expected to require deeper circuits than the one needed to evolve one single quantum state.

Here we propose a novel algorithm that makes use of a variational form U evolving only the state $|P_i\psi\rangle$, and show that it leads to much shallower circuits. In the next sections, we first introduce the definition of the components of the Green's function, and show how these can be calculated through real-time evolution techniques. We then discuss the choice of the ansatz for the VQS algorithm, listing the most important requirements and suggesting possible strategies to comply with these. Eventually, we will see how the choice of a variational form falls naturally upon the variational Hamiltonian ansatz [137, 138]. In Sec. 6.4 we present our novel algorithm for the calculation of the Green's function, and in Sec. 6.5 we compare the results obtained from numerical simulations with those from the algorithm of Ref. [132] for the case study of a 2-site Hubbard model. We show that for this particular problem the exact evolution of the state $P_i|\psi\rangle$ can be obtained by exponentiating only *one* of the Pauli components of the qubit Hamiltonian, while the same simplification does not hold when evolving $|\psi\rangle$ and $|P_i\psi\rangle$ at the same time. The quantum circuit corresponding to the algorithm suggested is shallow enough to be executed on current quantum computers. In Sec. 6.6 we compare the results obtained with the two algorithms for the 3-site Hubbard model with open-boundary conditions and 4-site Hubbard model with periodic-boundary conditions, and discuss the scaling for larger problems. Finally, in Sec. 6.7 we show the results for the 2-site Hubbard model obtained with state-of-the-art superconducting IBM Quantum processors.

6.2 Green's function through real-time evolution

We start defining the components of the Green's function of relevance for this work. The lesser Green's function is defined as

$$G_{lm}^<(t) = -i \langle \psi | e^{i\hat{H}t} \hat{c}_l e^{-i\hat{H}t} \hat{c}_m^\dagger | \psi \rangle , \quad (6.1)$$

where $|\psi\rangle$ is the ground state of the Hamiltonian and c_m^\dagger, c_l are fermionic creation and annihilation operators respectively. The greater component is instead

$$G_{lm}^>(t) = +i \langle \psi | \hat{c}_m^\dagger e^{i\hat{H}t} \hat{c}_l e^{-i\hat{H}t} | \psi \rangle . \quad (6.2)$$

The difference between these components gives the retarded Green's function, which is the target of our calculations for its applications in linear-response theory:

$$G_{lm}^R = \left[G_{lm}^<(t) - G_{lm}^>(t) \right] \theta(t) , \quad (6.3)$$

where $\theta(t)$ is the Heavyside step function. The real-time approach to the calculation of the Green's function consists in computing the states $e^{-i\hat{H}t} |\psi\rangle$ and $e^{-i\hat{H}t} c_m^\dagger |\psi\rangle$, which represent the time evolution of the states $|\psi\rangle$ and $c_m^\dagger |\psi\rangle$ respectively. The choice of the time evolution technique, which is crucial for designing an efficient quantum circuit for the calculation of the Green's function, is discussed in the next paragraph.

6.3 Choice of the variational form for the VQS

We briefly introduce the techniques suitable to follow the time evolution of a quantum system, and then focus on the choice of a proper ansatz for the VQS. The time evolution of a generic quantum state $|\phi_0\rangle$ is obtained through the action of the time evolution operator:

$$|\phi(t)\rangle = e^{-iHt} |\phi_0\rangle . \quad (6.4)$$

On a quantum computer, this can be achieved by applying the unitary gate expressing the exponential of the Hamiltonian to the qubit register encoding the state $|\phi_0\rangle$. The qubit Hamiltonian, which is built thanks to the mapping of the fermionic Hamiltonian to the qubit Hilbert space, is a weighted sum of multiple-qubits Pauli gates

$$H = \sum_m c_m P_m . \quad (6.5)$$

Therefore, the exact expression of the propagator is

$$U = e^{-i \sum_m c_m P_m t} . \quad (6.6)$$

Since the operators P_m do not necessarily commute with each other, it is not possible to express U as a product of exponentials in an exact way. Nevertheless, thanks to the Suzuki-Trotter expansion, the propagator can be approximated as a product of exponentials:

$$e^{-i \sum_m c_m P_m t} = \left(\prod_m e^{-i c_m P_m t/n} \right)^n + o\left(\frac{t^2}{n}\right). \quad (6.7)$$

Unfortunately, this approach requires deep circuits, especially when the time evolution is carried for long times, and therefore it is not optimal for near-term noisy quantum devices. A remarkable advantage in terms of circuit depth can instead be obtained by adopting variational quantum simulation (VQS) algorithms [136, 91]. These techniques consist in optimizing the parameters of a variational form $U(\bar{\theta} = \theta_1, \dots, \theta_M)$ to satisfy the variational principles which hold for the exact time evolution. The variational principle most often adopted for quantum simulations is McLachlan's, due to its numerical stability, and reads

$$\delta \|d/dt + iH|\phi(\bar{\theta}(t))\| = 0. \quad (6.8)$$

Eq. 6.8 leads to the following differential equation for the parameters $\bar{\theta}$:

$$\sum_{j=1} M_{ij} \dot{\theta}_j = V_i, \quad (6.9)$$

where

$$M_{ij} = \Re \langle \partial_i \phi | \partial_j \phi \rangle + \langle \partial_i \phi | \phi \rangle \langle \partial_j \phi | \phi \rangle, \quad (6.10)$$

and

$$V_i = \Im \langle \partial_i \phi | H | \phi \rangle + i \langle \partial_i \phi | \phi \rangle \langle \phi | H | \phi \rangle. \quad (6.11)$$

Here, we have adopted the shortcut notations $|\phi\rangle = |\phi(\bar{\theta}(t))\rangle$ and $|\partial_i \phi\rangle = \frac{\partial}{\partial \theta_i} |\phi(\bar{\theta}(t))\rangle$.

The McLachlan variational principle has a simple and instructive geometric interpretation, which is discussed in Ref. [139]: the variational form $U(\theta_1, \dots, \theta_M)$ represents a M -dimensional manifold embedded in the N dimension Hilbert space (N being equal to 2^n , with n number of qubits). In most cases the parameters θ_i are real, and therefore it is more convenient to describe the Hilbert space as a $2N$ -dimensional real vector space, i.e. a space which is spanned by $2N$ complex vectors with *real* coefficients (see Ref. [139] for a detailed discussion). In a real vector space, the tangent space to the manifold \mathcal{M} associated to the variational form $U(\bar{\theta})$ is spanned by the vectors:

$$|T_i\rangle = |\partial_i \phi\rangle - \langle \phi | \partial_i \phi \rangle |\phi\rangle. \quad (6.12)$$

It is easy to check that $\langle T_i | \phi \rangle = 0$, $\forall i = 1, \dots, M$, as $|\phi\rangle$ belongs to the subspace of vectors with norm 1. In Appendix B.1, we show that Eq. 6.9 can be elegantly written as

$$\sum_{j=1}^M \Re \langle T_i | T_j \rangle \dot{\theta}_j = \Im \langle T_i | H | \phi \rangle, \quad (6.13)$$

with $\langle T_i | T_j \rangle$ being the Quantum Geometric Tensor [140, 141]. Eq. 6.13 states that only the component of the vector $H|\phi\rangle$ which is parallel to the tangent subspace to the manifold at the point $|\phi\rangle$ drives the time evolution. Note that when $H|\phi\rangle$ is perpendicular to the tangent subspace at the manifold, the right hand side of Eq. 6.13 vanishes, so there is no time evolution (apart from a global phase). This happens correctly when $|\phi\rangle$ is eigenstate of the Hamiltonian, and $\langle T_i | H|\phi\rangle = E \langle T_i | \phi\rangle = 0$. However, this can happen also due to a poor choice of the variational form, leading to an unphysical evolution where the state remains constant. Unfortunately, the choice of a good variational form is in general quite problematic, as we will show in the following.

A variational form is actually a circuit expressing the unitary operator $U(\bar{\theta})$ which is applied to the state $|\phi_0\rangle$ to be evolved. As such, it must satisfy the following conditions. (I) It must be equal to the identity for the initial choice of the parameters $\bar{\theta}_0$. It is not straightforward to identify the parameters which turn the variational form into the identity, and most often it is easier to design variational forms that are equal to the identity for $\bar{\theta}_0 = 0$. (II) The number of parameters must be much smaller than the size of the Hilbert space, otherwise the advantage of the variational algorithm would be lost. (III) It must be such that the projection of the vector $H|\phi\rangle$ (which is proportional to the exact time derivative of the state $|\phi\rangle$) on the tangent subspace is as large as possible, as underscored by Eq. 6.13. (IV) In order to be realizable on near-term quantum computers, it must contain a limited number of controlled operations, and, more in general, lead to sufficiently shallow circuits. We can now distinguish two main kinds of variational forms. Empiric ansätze are expressive quantum circuits usually characterized by the alternation of CNOTs which create entanglement and rotations for the parametrization [142]. As opposite to empiric ansätze, the physically inspired ansätze are based on the physical properties of the system. The most important representative of this category is the variational Hamiltonian ansatz (VHA) [137, 138]. This takes inspiration from the Suzuki-Trotter expansion of Eq. 6.7, and the parametrization is introduced by replacing the product $c_m t$ with a function $\theta_m(t)$:

$$U_{VHA} = \prod_{d=1}^{n_d} \left(\prod_{m=1}^M e^{i\theta_m(t)P_m} \right); \quad (6.14)$$

here, n_d is the depth of the circuit, and corresponds to the number of Trotter steps. We will now highlight the issues that can drive from the choice of an empiric ansatz, and show how those can be circumvented by adopting the VHA.

The initial value problem. As stated before, any ansatz must contain entangling operators which express an interacting many-body state. One of the most used entangling operator is the CNOT gate, since it is native on many superconducting devices. The position of these CNOTs must be carefully engineered in such a way that the ansatz is equal to the identity at the beginning of the evolution, as required by point I. This is not an easy task to achieve while keeping the circuit shallow at the same time. A strategy to do so can exploit the identity $\text{CNOT}^2 = I$ and compose a circuit of units such as those represented in Fig. 6.1, where a layer

of CNOTs is followed by a layer of rotations which are equal to the identity for $\theta = 0$ and then another layer of CNOTs with the order inverted. We will see that this kind of structure looks very similar to the circuit to exponentiate the single Pauli operator P_m of the qubit Hamiltonian. Another possibility is to use an ansatz of the following form:

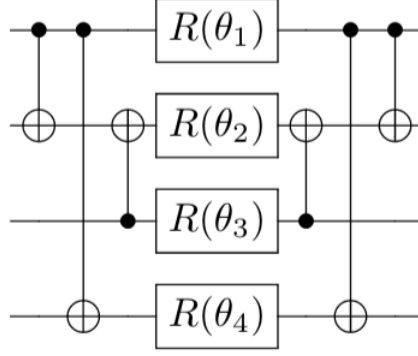


Figure 6.1: Example of quantum circuit which is equal to the identity when $\bar{\theta} = 0$.

$$U = \tilde{U}^\dagger(\bar{\theta}_0) \tilde{U}(\bar{\theta}), \quad (6.15)$$

which guarantees by construction condition I. However, both strategies require to double the number of CNOTs, and are thus less suited for proof-of-principle demonstrations on near-term quantum processors (point IV).

The problem of the initialization of the time evolution. As anticipated above, the VQS can predict erroneously the initial state to remain constant in the time, if the vector $H|\phi_0\rangle$ is orthogonal to the tangent subspace at the point $|\phi_0\rangle$ of the manifold associated to the variational form. Unfortunately, this can happen often, and represents a major issue in the choice of an empiric ansatz. The reason is simple: the vector $H|\phi_0\rangle$ points to one of the $2N$ possible directions of the real vector space associated to the Hilbert space. Choosing an empiric ansatz of M parameters, with M considerably smaller than N (in order to satisfy point II), consists in drawing a M -dimensional surface in a much larger space, while hoping that this surface be parallel to a specific direction, which is likely to fail. Things are made more difficult by the fact that different VQS parameters may span the same direction in the tangent subspace. An example of this is represented by the ansätze with tunable depth

$$U(\bar{\theta}) = \prod_{d=1}^{n_d} \tilde{U}(\theta_1^d, \dots, \theta_l^d), \quad (6.16)$$

which are obtained by repeating the same block \tilde{U} a number of times equal to the circuit depth n_d . It can be easily proven that increasing the circuit depth does not increase the size of the tangent subspace: as expressed in Eq. 6.12, the tangent subspace is generated by the derivatives of the variational form with respect to its parameters; if we consider two

corresponding parameters $\theta_i^{d_1}$ and $\theta_i^{d_2}$ belonging to the layers d_1 and d_2 , we can prove that the derivative of the ansatz U with respect to these two parameters are equal to each other at the origin (in the case in which this coincides with the point $\tilde{\theta} = 0$ and the blocks \tilde{U} are equal to each other):

$$\begin{aligned} \frac{\partial U}{\partial \theta_i^{d_1}}(\tilde{\theta} = 0) &= \tilde{U}(0) \dots \frac{\partial \tilde{U}}{\partial \theta_i^{d_1}}(0) \dots \tilde{U}(0) = \frac{\partial \tilde{U}}{\partial \theta_i^{d_1}}(0) \\ &= \frac{\partial \tilde{U}}{\partial \theta_i^{d_2}}(0) = \frac{\partial U}{\partial \theta_i^{d_2}}(\tilde{\theta} = 0) . \end{aligned} \quad (6.17)$$

The orthogonality problem described above becomes more and more important when the number of qubits (i.e. the size of the Hilbert space) grows. Now, we know that $|H\phi\rangle = \sum_m P_m |\phi\rangle$, and we could try to engineer the empiric ansatz in a way such that the product of the vectors $|T_i\rangle$ and $|P_m\phi\rangle$ is not vanishing. The most straightforward way to do this is to impose that $\partial_m |\phi\rangle = i P_m |\phi\rangle$, but this is exactly the VHA ansatz introduced above.

In fact, the VHA ansatz does not suffer from the problems analysed. First of all, it is equal by construction to the identity when $\tilde{\theta} = 0$. Furthermore, it can be proven (see Appendix B.2) that when adopting this variational form, the VQS solution coincides with the exact propagator for vanishing small times, with parameters

$$\theta_m = c_m t + \mathcal{O}(t^2) , \quad (6.18)$$

and thus respects exactly the condition III. This happens for *any* state $|\phi_0\rangle$ that is evolved. In many cases of interest, the combination of this ansatz with the VQS algorithm allows to reduce remarkably the circuit depth with respect to the Suzuki-Trotter expansion technique. The fact that the VHA is a natural choice for the time evolution of states especially when the size of the Hilbert space grows must be taken into account when designing algorithms for near-term quantum computers and in the following we leverage on its properties to propose a new and optimized algorithm for the calculation of Green's functions.

6.4 Optimized algorithm

The standard technique to calculate correlation functions [129, 130, 131] adopts the circuit shown in Fig 6.2a, where the propagator e^{-iHt} is calculated using the Suzuki-Trotter expansion. Endo et al. [132] improved this algorithm by replacing the Trotter expansion, which requires very deep circuits, with a variational form U whose parameters are determined through the VQS algorithm. In order for this to work, the operator U has to accurately approximate the time evolution for the ground state $|\psi\rangle$ and the state $|P_i\psi\rangle$ at the same time, i.e. with the same parameters θ_i (the evolution of the ground state consists simply in adding the correct phase without modifying the state). This requirement allows one to eliminate the controlled variational form CU from the circuit (see Fig. 6.2b), which would be otherwise necessary when U evolves $|\psi\rangle$ and $|P_i\psi\rangle$ with a different choice of the parameters for the two states. For this reason, we shall refer to this algorithm as control-free (CF). Requiring U to evolve two states at

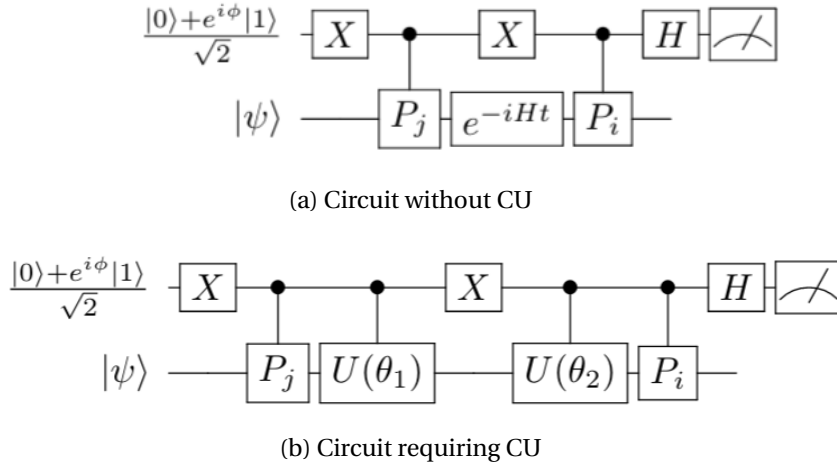


Figure 6.2: Panel (a) shows the circuit for the calculation of correlation functions previously suggested in literature. In Ref. [129, 130, 131] the unitary operator evolving the system is calculated through Suzuki-Trotter expansion. Ref. [132], instead, express the propagator e^{-iHt} through a variational form $U(\tilde{\theta})$ whose parameters are determined through the VQS McLachlan algorithm. It is important to stress that such approach works only if $U(\tilde{\theta})$ approximates accurately the time evolution of the states $|\psi\rangle$ and $P_j|\psi\rangle$; otherwise it becomes necessary to adopt the quantum circuit shown in panel (b), which requires a controlled $U(\tilde{\theta})$.

the same time seems to be a good price to pay to remove the CU operations, since a controlled unitary operation acting on n qubits is in general very complicated to realize and can require a large number of CNOTs for its implementation. However, it turns out that this strategy is not always advantageous: first of all, as discussed in the previous section, it is difficult to find a shallow empiric variational form that can propagate a desired state with a sufficiently small error. This task is even harder as the size of the Hilbert space grows, particularly if one requires the ansatz to evolve two states simultaneously. This leads naturally to the choice of the VHA ansatz. Second, we argue that it is possible to control the VHA by adding a minimal number of controlled operations, as shown in Fig. 6.3b. Therefore, the use of c-VHA does not necessarily imply a significant increase in controlled operations and, consequently, unaffordable circuit depths. Finally, evolving two states at the same time requires a deeper variational ansatz, with a larger cost in terms of controlled operations and circuit depth, as it will be proven numerically in the following sections. This is because the variational ansatz must approximate the ideal time evolution operator in at least two independent directions in the Hilbert space. It is easy to conclude that an algorithm for the Green's function which requires a controlled evolution operator evolving one single state at a time can lead to an improvement in terms of circuit depth and number of CNOTs. This improved algorithm can be obtained under the assumption of a time independent Hamiltonian, which holds in many problems studied in the literature. In this case, the propagator is e^{-iHt} , and its action on the ground state introduces simply a phase rotation $e^{-iHt}|\psi\rangle = e^{-iE_0t}|\psi\rangle$, E_0 being the ground state energy which can be calculated through the variational quantum eigensolver (VQE) algorithm. Using this relation,

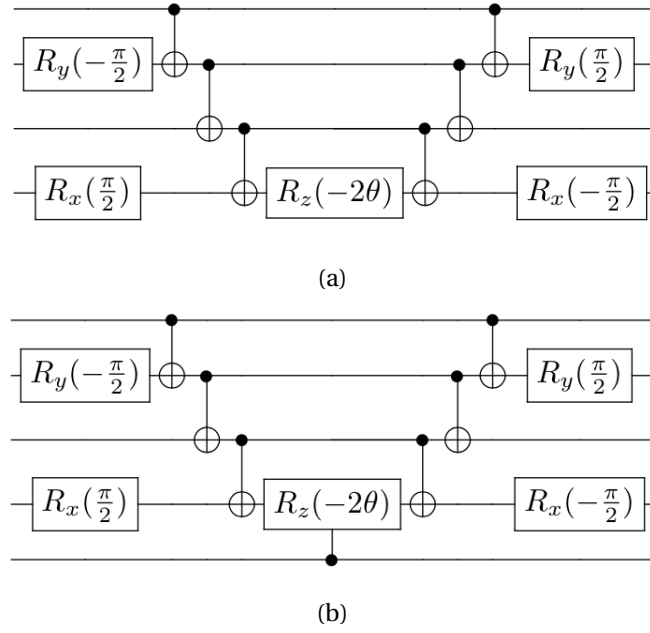


Figure 6.3: The circuit expressing the unitary $e^{-i\theta P_i}$ can be constructed using the rules of Ref. [143]. Panel (a) shows an example of the circuit corresponding to the exponential of the four-qubit Pauli gate ZXZY (namely $e^{-i\theta ZXZY}$). Panel (b) shows its controlled form. Notice that the controlled form is realized by simply controlling the central Rz gate alone. As a result, the controlled VHA simply requires the addition of a control operation for each appearing Pauli term, which is minimal considering that the exponential of a n -qubit Pauli gates requires at most $2(n-1)$ CNOTS.

the expression of the lesser Green's function becomes

$$G_{lm}^<(t) = e^{iE_0 t} \langle \psi | c_l e^{-iHt} c_m^\dagger | \psi \rangle. \quad (6.19)$$

After mapping the fermionic Hamiltonian on a qubit register, the expression for the Green's function becomes

$$G_k^<(t) = e^{iE_0 t} \sum_{ij} \langle \psi | P_i U P_j^\dagger | \psi \rangle \lambda_i \lambda_j^* \quad (6.20)$$

where U is the ansatz of the VQS algorithm, and λ_i are the coefficients of the expansion of the creation/destruction operators in terms of Pauli gates. Since the operator $P_i U P_j^\dagger$ is not Hermitian, the bracket must be computed through the Hadamard test; the circuit is the one shown in Fig. 6.4a. It can be easily observed that in this case the ansatz only implies the evolution of the state $P_i | \psi \rangle$ at the price of a controlled evolution operator. Furthermore, when $P_i = P_j$, it is possible to remove the control operation on these gates, as shown in Fig. 6.4b. Since the operator U^\dagger is removed from the expression, it is necessary to take correctly into account the global phase of the state $U | P_j \psi \rangle$. This can be done in a very simple way, as suggested in Ref. [136], without the need to add a global phase to the ansatz used for the time evolution: indeed, the time dependent global phase $\theta_0(t)$ ensuring that the

state $e^{i\theta_0(t)}U(\theta_1(t), \dots, \theta_m(t))|\phi_0\rangle$ coincides with the time evolution of the state $|\phi_0\rangle$ can be determined using the McLachlan principle. By manipulating Eq. 6.9 we obtain the following differential equation:

$$\dot{\theta}_0 = \sum_{i=1}^M \Im \langle \partial_i \phi | \phi \rangle \dot{\theta}_i - \langle \phi | H | \phi \rangle, \quad (6.21)$$

where the $\dot{\theta}_i$ for $i = 1, \dots, m$ are those calculated through the VQS method. In order to obtain the correct brackets, it is necessary to multiply the result of the circuit in Fig. 6.4 by $e^{i\theta_0(t)}$.

The very same procedure can be followed to calculate the greater component of G , and thus the retarded correlation function. Since the proposed algorithm requires the evolution of one state at time, we shall refer to this algorithm as one-state (OS). In the next sections we will show the advantage of this algorithm for the 2- and 3-site Hubbard model with open-boundary conditions and 4-site with periodic-boundary conditions.

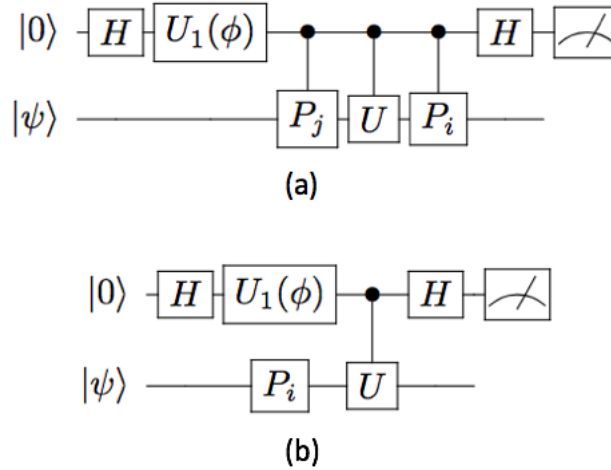


Figure 6.4: Panel (a) shows the circuit to calculate the bracket of Eq. 6.20. When $\phi = 0$, the Z-measurement of the first qubit gives the real part of the bracket, while the imaginary part can be obtained by setting $\phi = -\frac{\pi}{2}$. The controlled operations on the Pauli gates P_i and P_j can be further removed if $P_i = P_j$, as shown in panel (b).

6.5 2-site Hubbard model

First, we test our algorithm on the 2-site Hubbard model. It is possible to take advantage of the many symmetries of this model in order to reduce the depth of the ansatz used to evolve a generic state $P_i|\psi\rangle$. In particular, here we prove that the *exact evolution* of the state $P_i|\psi\rangle$ is obtained by simply exponentiating one single Pauli component of the Hamiltonian (i.e. one among XXZI, YYZI, IXZX, IYZY). It is important to note that the present algorithm can exploit these peculiar symmetry properties, thanks to the fact that it only requires to implement the time-evolution of a single state $P_i|\psi\rangle$. Conversely, the CF algorithm, where the VHA ansatz has to evolve the states $P_i|\psi\rangle$ and $|\psi\rangle$ with the same parameters, requires not only

the exponentiation of all Pauli terms in the Hamiltonian, but also the doubling of the circuit depth (depth=2), resulting in much deeper quantum circuits (see Fig. 6.5).

We start introducing the Hubbard dimer Hamiltonian

$$\hat{H} = -\tau \sum_{\sigma=\uparrow,\downarrow} (\hat{c}_{1\sigma}^\dagger \hat{c}_{2\sigma} + \hat{c}_{2\sigma}^\dagger \hat{c}_{1\sigma}) + U \sum_{i=1,2} \hat{c}_{i\uparrow}^\dagger \hat{c}_{i\uparrow} \hat{c}_{i\downarrow}^\dagger \hat{c}_{i\downarrow} - \frac{U}{2} \sum_{i=1,2} \hat{c}_{i\sigma}^\dagger \hat{c}_{i\sigma} . \quad (6.22)$$

The Jordan-Wigner transformation allow us to map the fermionic Hamiltonian into the following qubit Hamiltonian

$$H = -\frac{U}{2} \text{IIII} - \frac{\tau}{2} (\text{IXZX} + \text{IYZY} + \text{XZXI} + \text{YZYI}) + \frac{U}{4} (\text{IIZZ} + \text{ZZII}) . \quad (6.23)$$

Here we use the mapping $(1 \uparrow, 1 \downarrow, 2 \uparrow, 2 \downarrow) \rightarrow (q_1, q_2, q_3, q_4)$. It is now possible to recognize two sets of operators,

$$S_1 = \{\text{IXZX}, \text{IYZY}, \text{XZXI}, \text{YZYI}\}$$

and

$$S_2 = \{\text{ZZII}, \text{IIZZ}\}$$

such that, $\forall P_l, P_m \in S_i$:

- (i) $[P_l, P_m] = 0$ (each pair of operators commute);
- (ii) $[H, P_l P_m] = 0$ (the product of each pairs of operators commute with H) ;
- (iii) $P_l^2 = I$.

These symmetries have very important consequences on the choices of the ansatz for the time evolution. We will derive now a series of properties that will lead to drastic simplification of the time evolution circuit for the propagation of the Green's functions.

Proposition 1. *If the ground state $|\psi\rangle$ of the Hamiltonian is non-degenerate, then $\forall P_l, P_m \in S_i \implies P_l P_m |\psi\rangle = |\psi\rangle$.*

Proof: By definition, the ground state is the vector $|\psi\rangle$ such that $\langle\psi|H|\psi\rangle$ is minimum. However, $\langle\psi|H|\psi\rangle = \langle\psi|P_m^\dagger P_l^\dagger H P_l P_m |\psi\rangle$ from property (ii) above. Since we assume that the ground state is non-degenerate, then $P_l P_m |\psi\rangle = \alpha |\psi\rangle$. Using the commutation of P_l and P_m (i) we have also that $P_m P_l |\psi\rangle = \alpha |\psi\rangle$. Now, $P_l P_m P_m P_l |\psi\rangle = \alpha^2 |\psi\rangle$. At the same time, since Pauli matrices square to unity, $P_l P_m P_m P_l |\psi\rangle = |\psi\rangle$; it follows that $\alpha = \pm 1$. Finally, $\langle\psi|P_l|\psi\rangle + \langle\psi|P_m|\psi\rangle = \langle\psi|P_m P_l P_m |\psi\rangle + \langle\psi|P_l P_m P_l |\psi\rangle = \alpha (\langle\psi|P_l|\psi\rangle + \langle\psi|P_m|\psi\rangle)$; therefore, $\alpha = 1$.

Following Proposition 1, it is possible to derive the following corollary.

Proposition 2. *If the ground state $|\psi\rangle$ of the Hamiltonian is non-degenerate, then $\forall P_l, P_m \in S_i \implies P_l|\psi\rangle = P_m|\psi\rangle$.*

This result can be obtained by multiplying both the sides of the result of Proposition 1 by P_l and using the property (iii) above.

Let us now proceed with the analysis of the time evolution of a generic state, which is obtained by applying the creation/destruction operators to the ground state $|\psi\rangle$. Because of the Jordan-Wigner transformation, this corresponds to applying a Pauli operator \tilde{P} (e.g. ZZXI) to the ground state; a tilde is used to remark that $\tilde{P} \notin S_i$.

Let us consider $P_l, P_m \in S_i$. For Proposition 2, we have that $P_l|\psi\rangle = P_m|\psi\rangle = |\chi\rangle$. Therefore,

$$P_l \tilde{P} |\psi\rangle = \tilde{P} |\chi\rangle + [P_l, \tilde{P}] |\psi\rangle$$

and

$$P_m \tilde{P} |\psi\rangle = \tilde{P} |\chi\rangle + [P_m, \tilde{P}] |\psi\rangle .$$

In Appendix B.3 we prove that only two cases are possible:

1. $[P_l, \tilde{P}] = 0$, leading to $P_l \tilde{P} |\psi\rangle = \tilde{P} |\chi\rangle$;
2. $[P_l, \tilde{P}] = 2P_l \tilde{P} |\psi\rangle$, leading to $P_l \tilde{P} |\psi\rangle = -\tilde{P} |\chi\rangle$.

Using the simple rules described in Appendix B.3, we can then build the following table showing the sign of the term $P_l \tilde{P} |\psi\rangle$ (i.e. $\pm \tilde{P} |\chi\rangle$) for each couple of P_l (rows) and \tilde{P} (columns). It is now possible to relate these results with the time evolution of the operator $\tilde{P} |\psi\rangle$. At first

	XIII	ZXII	ZZXI	ZZZX	coeff.
XZXI	+	+	-	+	$-\tau/2$
YZYI	-	+	+	+	$-\tau/2$
IXZX	+	+	+	-	$-\tau/2$
IYZY	+	-	+	+	$-\tau/2$
ZZII	-	-	+	+	$U/4$
IIZZ	+	+	-	-	$U/4$

Table 6.1: Sign of the prefactor multiplying $\tilde{P} |\chi\rangle$. The Pauli matrices in the left column are components of the qubit Hamiltonian, with coefficient reported in the last column, while the Pauli matrices in the top row correspond to the fermion creation/annihilation operator in the qubit Hilbert space.

order in the expansion in t ,

$$e^{-iHt} \tilde{P} |\psi\rangle \simeq I - i \sum_m c_m t P_m \tilde{P} |\psi\rangle . \quad (6.24)$$

As the coefficients are the same for all the operators belonging to S_i , then the contributions of the elements of S_2 always cancel each other, while that of the elements of S_1 is always $2\tilde{P}|\chi\rangle$, so

$$e^{-iHt}\tilde{P}|\psi\rangle \simeq I - i2c_1tP_1\tilde{P}|\psi\rangle, \quad (6.25)$$

where P_1 is one of the Pauli matrices belonging to S_1 . For the second order expansion in t ,

$$H^2\tilde{P}|\psi\rangle = \sum_{lm} c_l c_m P_l P_m \tilde{P}|\psi\rangle = 2c_1 \sum_l c_l P_l P_1 \tilde{P}|\psi\rangle. \quad (6.26)$$

Since the Pauli operator belonging to S_2 anticommute with all those belonging to S_1 ,

$$H^2\tilde{P}|\psi\rangle = 2c_1 \sum_{l \in S_1} c_l P_1 P_l \tilde{P}|\psi\rangle - 2c_1 \sum_{l \in S_2} c_l P_1 P_l \tilde{P}|\psi\rangle \quad (6.27)$$

The second term in the r.h.s. of Eq. 6.27 vanishes as shown above, while the first term is equal to $4c_1^2 P_1^2$. It is straightforward to generalize the result at any order in perturbation theory, and conclude that the exact evolution of $\tilde{P}|\psi\rangle$ is obtained by applying the operator

$$U = e^{i\sigma\tau P_1 t} \quad (6.28)$$

where $P_l \in S_1$ and the sign σ can be read in Tab. 6.1 for each specific operator \tilde{P} .

We make now use of this compact form of the propagator in the simulation of the two-site Hubbard model. Fig. 6.5 shows the results for the retarded Green's function calculated numerically with the Qiskit *qasm* simulator [144]. The Green's function obtained with the OS algorithm is represented by green squares. Thanks to the properties shown above, the ansatz adopted is the one of Eq. 6.28, which contains only 5 CNOTs (in its controlled form). The Green's function obtained with the CF algorithm is represented with light blue circles ($d=1$) and violet diamonds ($d=2$). The former contains 20 CNOTs and fails to reproduce the exact Green's function dynamics, while the latter is in good agreement with it, but requires 40 CNOTs, as shown in Tab. 6.2. In summary, the novel OS algorithm manages to reach the same accuracy as the CF does; however, with a number of CNOTs and a total gate count of about one ninth.

6.6 Scaling to larger problem sizes

In order to provide further evidence about the advantages of the OS algorithm, we also performed calculations of the Green's function for the 3-site Hubbard chain with open-boundary conditions and the 4-site Hubbard chain with periodic-boundary conditions. In these cases, it is not possible to exploit the symmetries of the Hamiltonian to simplify the ansatz as much as for the 2-site Hubbard model. Nonetheless, we show that the suggested algorithm allows us to obtain an accurate Green's function with shallow circuits.

The 3-site Hubbard model is characterised by 2 degenerate ground states; here, we calculate the correlation function for one of these two ground states. The 4-site Hubbard model has

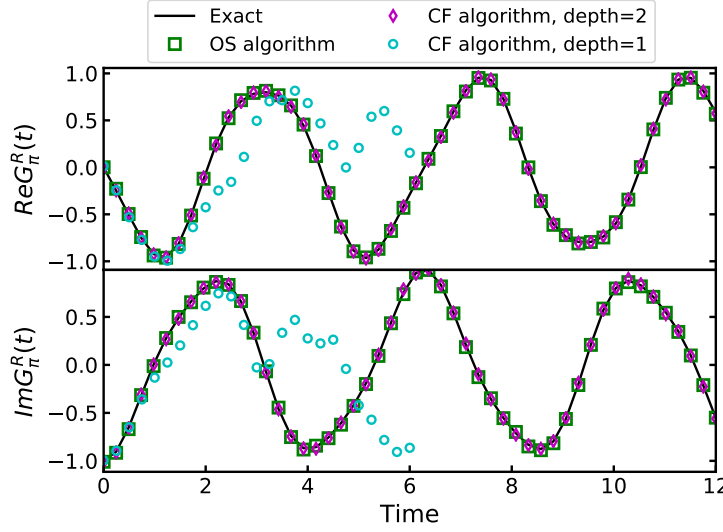


Figure 6.5: Real and imaginary part of the retarded Green's function G^R calculated at $k = \pi \uparrow$. The black line corresponds to the exact Green's function, the green squares to the Green's function obtained through the OS algorithm, and the light blue circles and the violet diamonds to those calculated through the CF algorithm with depth equal to 1 and 2 respectively.

instead a non-degenerate ground state. The retarded Green's function for both the models is computed at a k value such that $c_k = c_{1\uparrow} - c_{2\uparrow}$. The result is shown in Fig. 6.6: we observe that the Green's function for the 3-site Hubbard model obtained with the new algorithm using a VHA of depth $d = 3$ shows the same accuracy as the one computed with the CF algorithm with a depth $d = 5$, which fails to reproduce the exact Green's function when the depth is reduced to $d = 3$. The same happens for the 4-site Hubbard model. The advantage in terms of number of CNOTs and circuit depth is shown in Tab. 6.2.

To further investigate the scaling properties of the OS algorithm, let us summarize the main differences with respect to the CF protocol. On one hand, our strategy generally requires smaller VHA depths, thus reducing significantly the number of quantum operations necessary for a faithful description of the dynamics. On the other hand, one additional ancilla-controlled operation is necessary per Pauli string appearing in the Hamiltonian. Under the decomposition scheme presented in Fig. 6.3a – employing the native gate set of current IBM Quantum processors – the exponentiation of a single Pauli component of the Hamiltonian requires $2(w - 1)$ CNOTs, where w is the corresponding Pauli weight, i.e. the number of non-identity elements in the Pauli string. The total number of controlled operations required by the OS algorithm for a VHA of depth d_1 is thus:

$$n_1^{CNOT} = d_1 \sum_{i=1}^{n_p} (2(w_i - 1) + 1) = d_1 n_p (2(\bar{w} - 1) + 1), \quad (6.29)$$

6.6 Scaling to larger problem sizes

Two-site Hubbard model	1-qubit gates	2-qubit gates	ansatz depth
OS algorithm	4	5	9
CF algorithm, d=1	22	20	42
CF algorithm, d=2	44	40	84
3-site Hubbard model	1-qubit gates	2-qubit gates	ansatz depth
OS algorithm, d=3	96	147	243
CF algorithm, d=3	129	114	243
CF algorithm, d=5	160	190	350
4-site Hubbard model	1-qubit gates	2-qubit gates	ansatz depth
OS algorithm, d=3	192	372	564
CF algorithm, d=4	336	416	752
CF algorithm, d=5	420	520	940

Table 6.2: Number of 1-qubit and 2-qubit gates in the ansätze adopted to calculate the Green's function for the Hubbard model. The number reported for the OS algorithm corresponds to the controlled form of the ansatz, which is the one adopted to calculate the Green's function.

where n_p is the number of Pauli components of the Hamiltonian, w_i is the weight of the i -th component and \bar{w} is the average Pauli weight, defined as $\bar{w} = 1/n_p \sum_{i=1}^{n_p} w_i$. The CF algorithm requires instead, for a VHA of depth d_2

$$n_2^{CNOT} = d_2 \sum_{i=1}^{n_p} 2(w_i - 1) = d_2 n_p 2(\bar{w} - 1). \quad (6.30)$$

Combining Eqs. 6.29 and 6.30 it is easy to see that the suggested algorithm will show an advantage over the CF one when

$$\frac{d_2}{d_1} > 1 + \frac{1}{2(\bar{w} - 1)}. \quad (6.31)$$

Clearly, the OS algorithm is favoured for larger average Pauli weights. In this respect, the n -site Hubbard chain with open-boundary conditions and first nearest neighbours coupling represents the least favourable case: indeed, the average Pauli weight $\bar{w} = (14n - 12)/(5n - 4)$ has an asymptotic value of 2.8, thus requiring $d_2/d_1 > 1.27$ for the OS algorithm to be competitive. However, when replacing the open-boundary conditions with periodic-boundary conditions, or when assuming that the Hubbard sites are disposed on a 2d lattice instead of a chain, the appearance of Pauli components of maximum Pauli weight makes the condition of Eq. 6.31 much more favourable (see Appendix B.4). Finally, in a typical quantum chemistry problem, the interacting term $h_{pqrs} a_p^\dagger a_q^\dagger a_r a_s$ is mapped into

$$H_{pqrs} = \frac{h_{pqrs}}{8} \prod_{j=s+1}^{r-1} Z_j \prod_{k=q+1}^{p-1} Z_k \quad (6.32)$$

$$(XXXX - XXYY + XYXY + YXXY +$$

$$YXYX - YYXX + XYXX + YYYX),$$

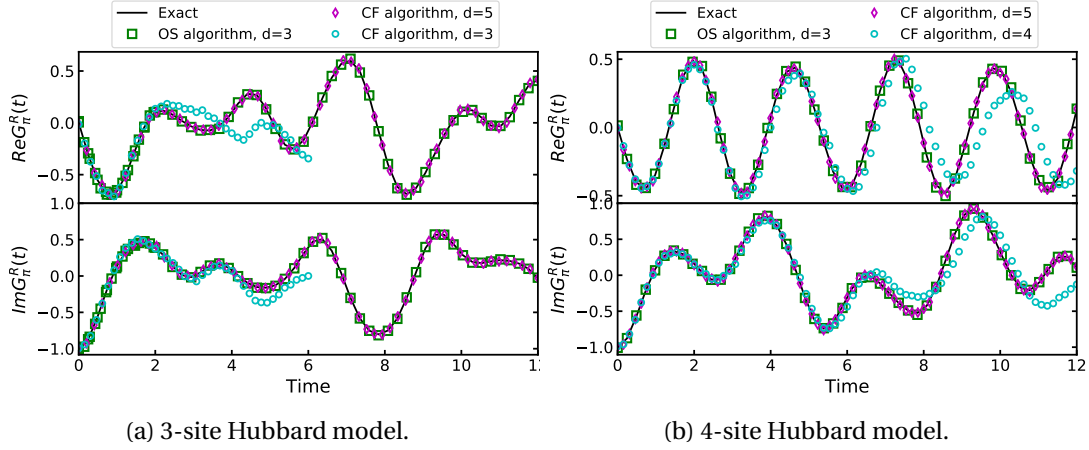


Figure 6.6: Panel (a) shows the real and imaginary time retarded Green's function calculated at $c_k = c_{1\uparrow} - c_{2\uparrow}$ for the 3-site Hubbard model with the different algorithms analysed up to now. Since the ground state is degenerate, we consider the first diagonal component, which is obtained by sandwiching the operator $U^\dagger c_k U c_k^\dagger$ with one of the ground states $|\psi_1\rangle$. Panel (b) shows the real and imaginary time retarded Green's function calculated at $c_k = c_{1\uparrow} - c_{2\uparrow}$ for the 4-site Hubbard model.

which can easily lead to large Pauli weights.

It is worth reminding that, while all the examples above were treated by making use of the Jordan-Wigner fermion-to-qubit mapping, other strategies are known, such as the Bravyi-Kitaev mapping [145], which in general leads to lower average Pauli weight in the asymptotic limit. These alternative mappings also have an impact on the VHA implementation details and required depths, thus requiring a case-by-case assessment [146].

Finally, it is also important to remark that the controlled VHA requires in general a higher connectivity between the ancilla and the system qubits. As a result, native hardware coupling maps and circuit compilation protocols must also be taken into account when selecting the most favorable strategy for specific applications.

6.7 Hardware results

The algorithm presented in this paper allows one to reduce remarkably the size of the circuit used to compute Green's functions for several model Hamiltonians. In the case of the 2-site Hubbard model, the improvement is such that it allows the execution of the algorithm on a current quantum processor. More specifically, we demonstrate an implementation of our OS algorithm on IBM Quantum superconducting devices, accessible via the cloud ¹.

We first obtain an approximate ground state using the VQE algorithm with the SPSA optimizer

¹See <https://quantum-computing.ibm.com/>.

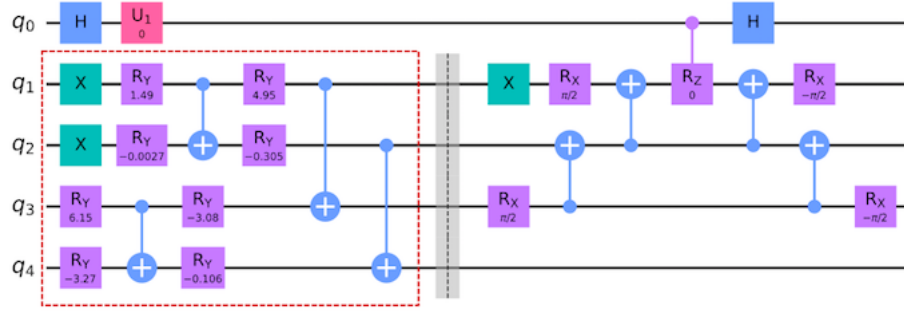


Figure 6.7: Circuit required to calculate the bracket in Eq. 6.20 when $P_i = P_j = \text{XIII}$ at $t = 0$. The part of the circuit which is enclosed in the red rectangle corresponds to the variational form adopted for the VQE.

on *ibmq_manila*. The adopted variational form is represented in Fig. 6.7 (within the red box), and consists of a concatenation of single R_y qubit rotations and CNOTs. For this experiment, we used a Hubbard Hamiltonian with $t = 1$ and $U = 3$. The theoretical ground state energy corresponds to $E_0 = -4$, while the experimental energy obtained with the VQE is -3.63. This result can be further improved on *ibmq_montreal*, due to the lower noise level of the processor. By also applying readout error mitigation [147], we obtain a ground state energy of -3.91.

After the optimization, we calculate the diagonal component of the retarded Green's function, $G_{1|1}^R$. The full circuit used for the calculation of the expectation values in Eq. 6.20 is given in Fig 6.7 for the case of $P_i = P_j = \text{XIII}$ at $t = 0$; further details on the calculation setup are given in Sec. 6.8. Due to the particle-hole symmetry, its real part is vanishing and only the imaginary part survives. The calculation is performed on *ibmq_montreal*, and the results are shown in Fig. 6.8a. This figure, however is not meaningful for a visual comparison with the experiments, due to the frequency shift introduced by the error on E_0 . It is instead much more instructive to consider the Green's function obtained from Eq. 6.20, where all matrix elements are measured on the quantum processor while the value of the energy in the phase of $e^{iE_0 t}$ is taken to be equal to its theoretical value, $E_0 = -4$ (instead of taking the approximated variational energy computed on *ibmq_montreal*) in Fig. 6.8c. The reasons are threefold. First, the adoption of the energy E_0 eliminates the small frequency shift and allows to appreciate visually the accuracy of the algorithm for the evaluation of the brackets in Eq. 6.20. Second, the ground state energy is just a parameter in Eq. 6.20 that could be evaluated with higher accuracy using other techniques (such as imaginary time evolution). Finally and most importantly, a small error in the ground state energy only leads to a small energy shift of the poles of the Green's function in frequency domain, as it can be seen by comparing Fig. 6.8b with Fig. 6.8d, where the noisy energy \tilde{E}_0 and the exact energy E_0 are used respectively (the proof is given in Sec. 6.8). This agrees with the general observation that, through e.g. Fourier analysis, useful and accurate information in the frequency domain can be obtained even from noisy quantum data [131, 148]. Overall, the agreement shown in Fig. 6.8c between the imaginary part of the exact Green's function and the one calculated on the hardware is very good, also considering

that no further error mitigation scheme is adopted at this stage. The real part of the Green's function obtained on hardware shows small oscillations around the exact value 0. These oscillations are mainly caused by the errors of the hardware in reproducing the true ground state wavefunction. In the frequency domain, the agreement between the exact result and the quantum computation is overall very good, both for the shape and the position of the peaks, also when the noisy energy \tilde{E}_0 is adopted.

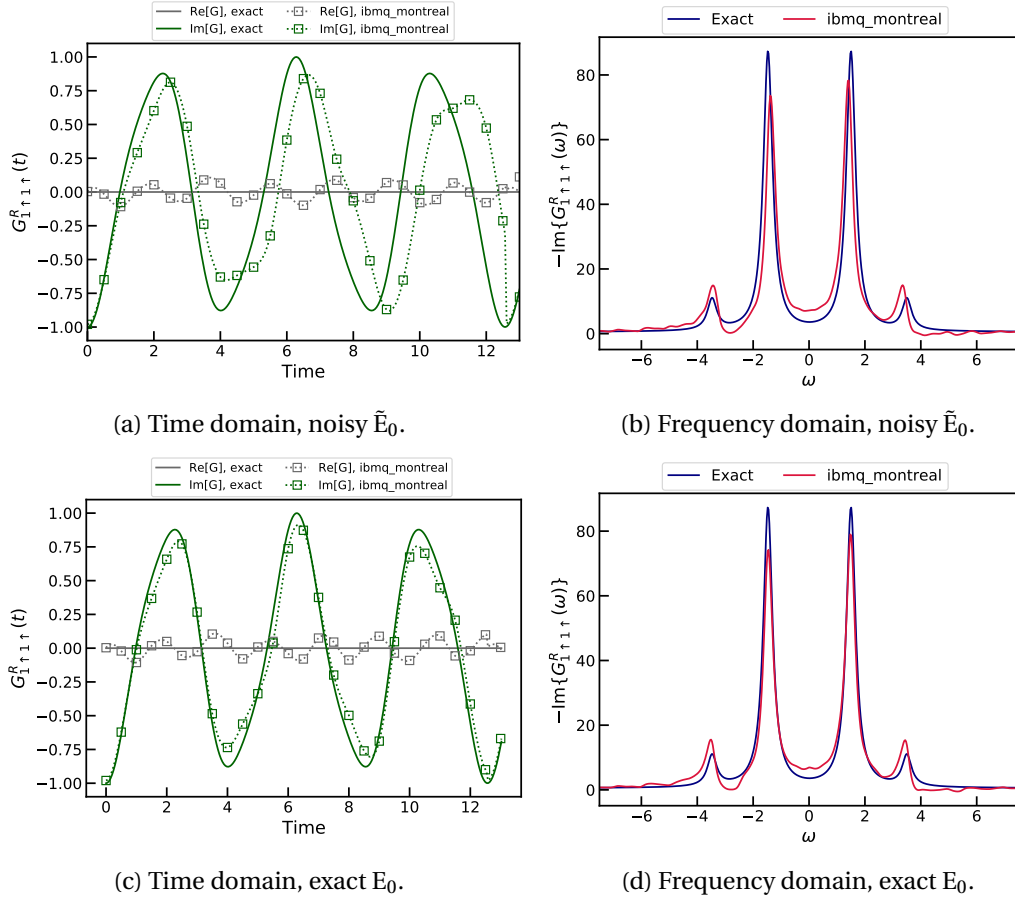


Figure 6.8: Panel (a) shows the retarded Green's function in time domain. The grey and green solid lines correspond to the exact real and imaginary parts respectively. The grey and green squares correspond to the results from the hardware. The dotted lines are obtained by interpolating the hardware result with splines. Panel (b) shows the imaginary part of the retarded Green's function in frequency domain. The blue and the red solid lines correspond respectively to the exact result and the quantum calculation. Panels (c) and (d) show the same quantities as Panels (a) and (b), with the only difference that now the Green's function is calculated using the exact energy $E_0 = -4$ in the phase factor $e^{iE_0 t}$ of Eq. 6.20.

6.8 Details about the calculation of the Green's function

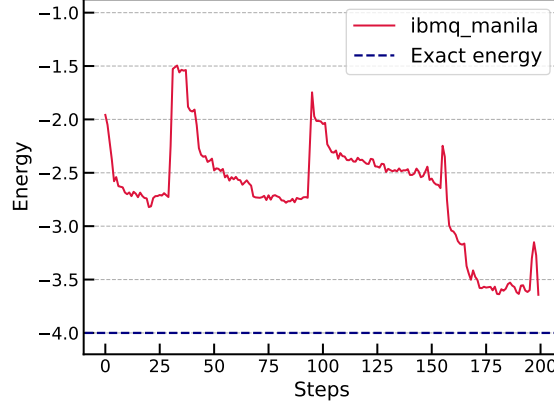


Figure 6.9: VQE algorithm for the ground state on *ibmq_manila*. The blue dashed line corresponds to the exact value, while the red line to the quantum calculation.

The optimization of the ground state energy is reported in Fig. 6.9.

The Green's function is calculated on *ibmq_montreal*. The layout of this quantum computer, together with the qubits used in the calculation are reported in Fig. 6.10.

As it is well known from the MBPT [17], the poles of the Green's function correspond to the energy of the charged excitations, $E_i(N \pm 1) - E_0(N)$, where N is the number of particles in the ground state (in this case $N=2$) and $E_i(N \pm 1)$ is the energy of the i -th excited states with $N \pm 1$ particles. In the 2-site Hubbard model with parameters $U=3$ and $t=1$ there are four poles, corresponding to the energies $\Delta E_1 = \pm 1.5$ and $\Delta E_2 = \pm 3.5$ (see Ref. [19] for the analytic solution of the Hubbard model), therefore the Green's function has a periodicity $T = 4\pi$. This is true only if the value of E_0 used in Eq. 6.20 is the exact one, as the noisy value \tilde{E}_0 would imply a longer period. In order to save quantum-computational time, we adopt the following trick (NB this trick, which relies on our knowledge of the exact solution of the problem, is definitely not necessary for the calculation of the Green's function, and it has been used here only to reduce the number of calculations ran on the quantum computer). First of all, we write the lesser term

$$G_k^<(t) = -ie^{i\tilde{E}_0 t} \langle \psi | c_k e^{-i\hat{H}t} c_k^\dagger | \psi \rangle = -ie^{i(\tilde{E}_0 - E_0)t} e^{iE_0 t} \langle \psi | c_k e^{-i\hat{H}t} c_k^\dagger | \psi \rangle, \quad (6.33)$$

with $g^<(t) = -ie^{iE_0 t} \langle \psi | c_k e^{-i\hat{H}t} c_k^\dagger | \psi \rangle$ periodic on $T = 4\pi$. We therefore calculate $g(t)$ over this time range and then its Fourier transform $g(\omega)$. Thanks to the convolution theorem,

$$G_k^<(\omega) = g^<(\omega + \tilde{E}_0 - E_0), \quad (6.34)$$

therefore we just need to shift the function $g(\omega)$ of $E_0 - \tilde{E}_0$ in order to obtain the correct Fourier transform. We can repeat the very same procedure for the greater term and thus obtain the retarded component.

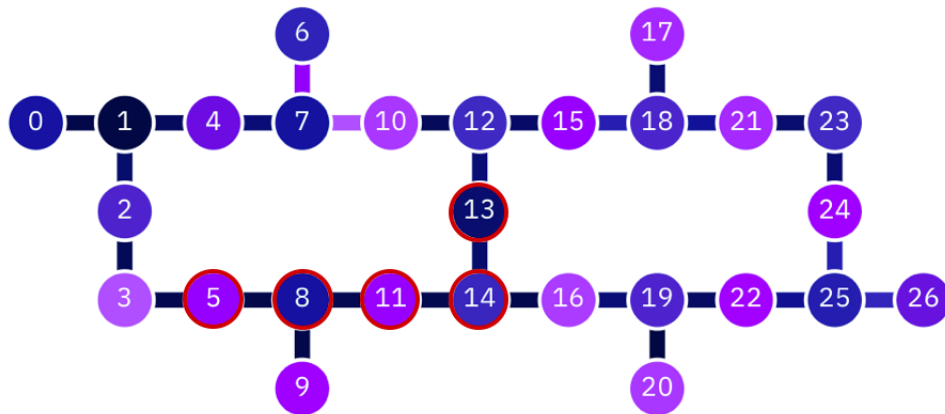


Figure 6.10: Layout of *ibmq_montreal*. The qubits used in the calculation of the Green's function are those circled in red.

Conclusions

This Thesis represented an effort to forward the research in the field of quantum technologies, by studying from first principles the properties of novel materials which could act as qubits or quantum sensors and suggesting new efficient algorithms for the solution of quantum chemistry problems on quantum computers.

We studied the phonon-assisted luminescence of the negatively charged boron vacancy in 2D hBN using MBPT, an analysis that has never been carried before due to the challenges represented by the large supercell of defect centers. Our simulations show that the phonon-independent luminescence is extremely weak, because the transition dipole moment between ground and excited state vanishes for symmetry, and the symmetry-breaking due to the static Jahn-Teller effect leads to a very small out-of-plane dipole moment.

We show instead that the experimentally observed spectrum is well described when including in the simulations the symmetry-breaking due to lattice vibration. We do this by calculating the exciton-phonon coupling through a finite differences technique. This theory goes beyond the Franck-Condon approximation, allowing to achieve a very good agreement with experiments. Our analysis shows that the phonon modes which are coupled most strongly with excitons have frequency between 600 and 700 cm^{-1} .

At low temperatures, the luminescence is determined by high-frequency modes which are strongly coupled with excitons. At $T > 200\text{K}$ the PL spectrum becomes dominated by low-frequency modes due to the Bose-Einstein statistics. The temperature dependence of the FWHM shows a very sensitive behaviour of the PL spectrum with the temperature, suggesting that this defect can be used as a nanoscale thermometer, at least in a range of temperatures between 0 and 200 K. The agreement between theory and experiments is very good, and we hope our explanation of the photoluminescence mechanisms will further the technological integration of defect centers for quantum information and sensing.

We then developed a technique to calculate electron-phonon coupling in defects with a finite differences approach. This technique exploits the symmetries of the system to minimize the set of displacements needed. We eventually show that this set of displacement coincides with that necessary for the calculation of the lattice vibration. The electron-phonon coupling thus becomes a simple post-processing of the finite differences phonons calculation.

Conclusions

We finally proposed an optimized real time propagation algorithm for the calculation of the Green's function on a near-term quantum computer, which exploits the time independence of the Hamiltonian and the features of the VHA ansatz and requires the time evolution of the only state $P_i |\psi\rangle$. We proved that this algorithm is more efficient in term of 2-qubit gates than the previously known ones, both for the 2-site 3-site and 4-site Hubbard models, and we estimate that the reported advantage is likely to persist when considering complex realistic quantum chemistry problems. In particular, this algorithm is able to exploit the symmetries of the 2-site Hubbard model, where the exact propagator of the state $P_i |\psi\rangle$ is obtained by exponentiating only one of the Pauli components of the Hamiltonian. This leads to a very shallow circuit for the calculation of the Green's function which, can then be executed on a current quantum computer, with results in remarkable agreement with the exact solutions.

We studied the scaling of the algorithm with the size of the problems, and proved that the algorithm proposed is favoured in problems where the Pauli weight of the components of the Hamiltonian is large. This is the case, for example, of quantum chemistry problems with interactions beyond first nearest neighbours.

We believe that the present work will promote further research towards the development of hardware efficient quantum algorithms for the calculation of electronic correlation functions, opening up new avenues in the study of complex many-body systems and their excitations on near-term quantum computers.

A Appendix

A.1 Functional derivatives

Be \hat{H} the interacting unperturbed Hamiltonian of the crystal. Due to the action of an external perturbation (e.g. the electromagnetic field), a time dependent term $\hat{H}_{int}(t)$ appears:

$$\hat{H}_{tot} = \hat{H} + \hat{H}_{int} . \quad (\text{A.1})$$

We now define the interaction picture in a different than Chap. 2. In fact, the interaction picture is defined in such a way as to single out the part of the Hamiltonian that we want to treat perturbatively. Since we want to study the response of a system to $\hat{H}_{int}(t)$, then we define the interaction picture as:

$$\hat{O}_I = e^{i\hat{H}t} \hat{O} e^{-i\hat{H}t} . \quad (\text{A.2})$$

Conversely, when we want to calculate the perturbative expansion of the Green's function, the perturbation is the electron-electron interaction term, so

$$\hat{O}_I = e^{i\hat{H}_0 t} \hat{O} e^{-i\hat{H}_0 t} . \quad (\text{A.3})$$

where \hat{H}_0 is the independent particle Hamiltonian. We define the Heisenberg picture with respect to the total Hamiltonian \hat{H}_{tot} :

$$\hat{O}_H = \hat{W}(t_0, t) \hat{O} \hat{W}(t, t_0) , \quad (\text{A.4})$$

where \hat{W} is the propagator defined in Eq. 2.114.

For a wavefunction,

$$\begin{aligned} |\psi_I(t)\rangle &= e^{i\hat{H}t} |\psi(t)\rangle = e^{i\hat{H}t} \hat{W}(t, t_0) |\psi(0)\rangle = \\ &e^{i\hat{H}t} \hat{W}(t, t_0) e^{-i\hat{H}t_0} |\psi_I(0)\rangle = \hat{U}(t, t_0) |\psi_I(0)\rangle \end{aligned} \quad (\text{A.5})$$

where the last equation implicitly defines the propagator \hat{U} , satisfying the equation

$$i \frac{d}{dt} \hat{U}(t, t_0) = \hat{H}_{int,I} \hat{U}(t, t_0) \quad (\text{A.6})$$

Appendix A. Appendix

where $H_{int,I}$ is the perturbative Hamiltonian in the interaction picture. The last equation allows to write the perturbative expansion of \hat{U} :

$$\hat{U}(t, t_0) = \sum_{v=0}^{+\infty} \frac{(-1)^v}{v!} \int_{-\infty}^{\infty} dt_1 \dots dt_v T[\hat{H}_{int,I}(t_1) \dots \hat{H}_{int,I}(t_v)], \quad (\text{A.7})$$

We recall here the definition of the Green's function,

$$G(\mathbf{x}t, \mathbf{x}'t') = -i \frac{\langle \Psi(t_0) | T[\hat{\psi}_H(\mathbf{x}t) \hat{\psi}_H^\dagger(\mathbf{x}'t')] | \Psi(t_0) \rangle}{\langle \Psi(t_0) | \Psi(t_0) \rangle}, \quad (\text{A.8})$$

where $|\Psi(t_0)\rangle$ is the ground state of the total perturbed Hamiltonian at the time t_0 . Since the perturbation $\hat{H}_{int}(t)$ starts at $t = -\infty$ and is switched on exponentially slowly, the Gell-Mann and Low theorem allows us to relate the perturbed ground state $|\Psi(t_0)\rangle$ to the unperturbed (interacting) ground state $|\Psi_0\rangle$:

$$\frac{|\Psi(t_0)\rangle}{\langle \Psi_0 | \Psi(t_0) \rangle} = \frac{|\hat{U}(t_0, \pm\infty) | \Psi_0 \rangle}{\langle \Psi_0 | \hat{U}(t_0, \pm\infty) | \Psi_0 \rangle} \quad (\text{A.9})$$

It follows that

$$G(\mathbf{x}t, \mathbf{x}'t') = -i \frac{\langle \Psi_0 | \hat{U}(-\infty, t_0) T[\hat{\psi}_H(\mathbf{x}t) \hat{\psi}_H^\dagger(\mathbf{x}'t')] \hat{U}(t_0, +\infty) | \Psi_0 \rangle}{\langle \Psi_0 | \hat{U}(-\infty, \infty) | \Psi_0 \rangle} \quad (\text{A.10})$$

by expressing $\hat{\psi}_H(\mathbf{x}t) \hat{\psi}_H^\dagger(\mathbf{x}'t')$ as $\hat{U}(t_0, t) \hat{\psi}_I(\mathbf{x}t) \hat{U}(t, t') \hat{\psi}_I^\dagger(\mathbf{x}'t') \hat{U}(t', t_0)$ and using the combinatorial properties of the time-ordered operator, we can finally obtain the perturbative expression for G :

$$G(\mathbf{x}t, \mathbf{x}'t') = -i \frac{N}{D}, \quad (\text{A.11})$$

with

$$N = \sum_{v=0}^{+\infty} \frac{(-1)^v}{v!} \int_{-\infty}^{\infty} dt_1 \dots dt_v \langle \Psi_0 | T[\hat{H}_{int,I}(t_1) \dots \hat{H}_{int,I}(t_v) \hat{\psi}_I(\mathbf{x}t) \hat{\psi}_I^\dagger(\mathbf{x}'t')] | \Psi_0 \rangle \quad (\text{A.12})$$

and

$$D = \sum_{v=0}^{+\infty} \frac{(-1)^v}{v!} \int_{-\infty}^{\infty} dt_1 \dots dt_v \langle N | T[\hat{H}_{int,I}(t_1) \dots \hat{H}_{int,I}(t_v)] | N \rangle \quad (\text{A.13})$$

We now want to calculate the functional derivative of G when an external perturbation is applied, which is described by H_{int} :

$$\delta G(\mathbf{x}t, \mathbf{x}'t') = -i \delta \frac{N}{D} = -i \frac{\delta N}{D} + i \frac{N}{D} \frac{\delta D}{D} \quad (\text{A.14})$$

then the first order terms in H_{int} are respectively

$$\delta N = -i \int_{-\infty}^{\infty} dt_1 \langle \Psi_0 | T[\hat{H}_{int,I}(t_1) \hat{\psi}_I(\mathbf{x}t) \hat{\psi}_I^\dagger(\mathbf{x}'t')] | \Psi_0 \rangle \quad (\text{A.15})$$

$$\delta D = -i \int_{-\infty}^{\infty} dt_1 \langle N | \hat{H}_{int,I}(t_1) | N \rangle \quad (\text{A.16})$$

Assuming that the perturbation has the shape

$$\hat{H}_{int,I} = \int_{-\infty}^{\infty} dt \int d^3\mathbf{x} d^3\mathbf{x}' U(\mathbf{x}, \mathbf{x}', t) \hat{\psi}_I^\dagger(\mathbf{x}, t) \hat{\psi}_I(\mathbf{x}', t) \quad (\text{A.17})$$

then

$$\frac{\delta N(1, 2)}{\delta(U(\mathbf{x}, \mathbf{x}', t))} = i \langle \Psi_0 | T[\hat{\psi}_I(1) \psi(\mathbf{x}', t) \hat{\psi}^\dagger(\mathbf{x}, t^+) \hat{\psi}_I^\dagger(2)] | \Psi_0 \rangle \quad (\text{A.18})$$

while

$$\frac{\delta D}{\delta(U(\mathbf{x}, \mathbf{x}', t))} = -i \langle \Psi_0 | \hat{\psi}_I^\dagger(\mathbf{x}, t) \hat{\psi}_I(\mathbf{x}', t) | \Psi_0 \rangle = i \langle \Psi_0 | T[\hat{\psi}_I(\mathbf{x}', t) \hat{\psi}_I^\dagger(\mathbf{x}, t^+)] | \Psi_0 \rangle. \quad (\text{A.19})$$

Putting all together:

$$\begin{aligned} \frac{\delta G(1, 2)}{\delta U(\mathbf{x}, \mathbf{x}', t)} &= -(-i)^2 \frac{\langle \Psi_0 | T[\hat{\psi}_I(1) \hat{\psi}_I(\mathbf{x}', t) \hat{\psi}_I^\dagger(\mathbf{x}, t^+) \hat{\psi}_I^\dagger(2)] | \Psi_0 \rangle}{\langle \Psi_0 | \hat{S} | \Psi_0 \rangle} \\ &\quad - i \frac{\langle \Psi_0 | T[\hat{\psi}_I(\mathbf{x}', t) \hat{\psi}_I^\dagger(\mathbf{x}, t^+)] | \Psi_0 \rangle}{\langle \Psi_0 | \hat{S} | \Psi_0 \rangle} G(1, 2) \\ &= -G(1, \mathbf{x}' t, 2, \mathbf{x} t^+) + G(1, 2) G(\mathbf{x}' t, \mathbf{x} t^+). \end{aligned} \quad (\text{A.20})$$

The fractions appearing in Eq. A.20 are related to the interacting one and two-particle Green's functions defined in Eqs. 2.41 and 2.96 because the interaction picture defined in this section coincides with the Heisenberg picture defined in Chap. 2, and $\hat{S} = 1$ in the limit of a vanishing perturbation. By definition

$$\frac{\delta G(1, 2)}{\delta U(\mathbf{x}, \mathbf{x}', t)} = L(1, \mathbf{x}' t, 2, \mathbf{x} t^+) \quad (\text{A.21})$$

is the reducible 2-particles correlation function. with similar arguments

$$\chi(1, x t) = \frac{\delta \langle \rho(1) \rangle}{\delta U(x t)} = \frac{-i \delta G(1, 1^+)}{\delta U(x t)} = L(1, x t, 1^+, x t^+) \quad (\text{A.22})$$

is the reducible polarizability.

A.2 Character tables and product rules

The dipole matrix element between two states $|\psi_i\rangle$ and $|\psi_j\rangle$ is defined as:

$$\mathbf{d}_{ij} = \langle \psi_i | \hat{\mathbf{r}} | \psi_j \rangle \quad (\text{A.23})$$

According to the selection rules from group theory [149], the dipole vanishes if the product of the irreducible representations of the wavefunctions $|\psi_{i/j}\rangle$ and the position operator $\hat{\mathbf{r}}$ does not contain the fully symmetric irreducible representation, which is labelled A'_1 for the D_{3h}

Appendix A. Appendix

and A_1 for the C_{2v} one. The product tables for the D_{3h} and C_{2v} are reported in Tab. A.1 and A.2 respectively.

For the D_{3h} group, the in plane components (x,y) of $\hat{\mathbf{r}}$ transform as the irreducible representation E' , while the out of plane component z as A_2'' . Tab. A.3a shows which dipoles matrix elements vanish for symmetry in the symmetric systems. For the C_{2v} group, the in plane components (x,y) of $\hat{\mathbf{r}}$ transform as the irreducible representations (A_1, B_1), while the out of plane component z as B_2 . Tab. A.3b shows which dipoles matrix elements vanish for symmetry in the Jahn-Teller distorted systems.

	A_1'	A_2'	E'	A_1''	A_2''	E''
A_1'	A_1'	A_2'	E'	A_1''	A_2''	E''
A_2'	A_2'	A_1'	E'	A_2''	A_1''	E''
E'	E'	E'	$A_1' + A_2' + E'$	E''	E''	$A_1'' + A_2'' + E''$
A_1''	A_1''	A_2''	E''	A_1'	A_2'	E'
A_2''	A_2''	A_1''	E''	A_2'	A_1'	E'
E''	E''	E''	$A_1'' + A_2'' + E''$	E'	E'	$A_1' + A_2' + E'$

Table A.1: Product table for the D_{3h} group.

	A_1	A_2	B_1	B_2
A_1	A_1	A_2	B_1	B_2
A_2	A_2	A_1	B_2	B_1
B_1	B_1	B_2	A_1	A_2
B_2	B_2	B_1	A_2	A_1

Table A.2: Product table for the C_{2v} group.

$ \psi_i\rangle$	$ \psi_j\rangle$	d_{xy}	d_z
A_2''	E'	0	0
E''	E'	0	$\neq 0$
E''	E'	0	$\neq 0$
A_1'	E'	$\neq 0$	0
A_2''	E''	$\neq 0$	0

(a) Value of the dipole matrix elements for some transitions of interest in the symmetric system (D_{3h} group).

$ \psi_i\rangle$	$ \psi_j\rangle$	d_{xy}	d_z
B_2	B_1	0	0
B_2	A_1	0	$\neq 0$

(b) Value of the dipole matrix elements for some transitions of interest in the Jahn-Teller distorted system (C_{2v} group).

B.1 Geometry of McLachlan principle

In this section we prove Eq. 6.13 of the main text. First, we use the identity

$$\langle \phi | \phi \rangle = 1 \quad \forall t \quad (\text{B.1})$$

to show that $\langle \partial_i \phi | \phi \rangle$ is a pure imaginary number. In fact

$$\partial_i \langle \phi | \phi \rangle = 0 = \langle \partial_i \phi | \phi \rangle + \langle \phi | \partial_i \phi \rangle \implies \langle \phi | \partial_i \phi \rangle = -\langle \partial_i \phi | \phi \rangle^* \quad (\text{B.2})$$

Therefore

$$\langle \partial_i \phi | \phi \rangle \langle \partial_j \phi | \phi \rangle = -\langle \partial_i \phi | \phi \rangle \langle \phi | \partial_j \phi \rangle = -\Re \langle \partial_i \phi | \phi \rangle \langle \phi | \partial_j \phi \rangle \quad (\text{B.3})$$

Substituting in Eq. 6.10 of the main text,

$$M_{ij} = \Re \left[\langle \partial_i \phi | \partial_j \phi \rangle - \langle \partial_i \phi | \phi \rangle \langle \phi | \partial_j \phi \rangle \right] = \Re \langle T_i | T_j \rangle .$$

Similarly, since $\langle \phi | H | \phi \rangle$ is real, then

$$i \langle \partial_i \phi | \phi \rangle \langle \phi | H | \phi \rangle = -\Im \langle \partial_i \phi | \phi \rangle \langle \phi | H | \phi \rangle . \quad (\text{B.4})$$

Substituting in Eq. 6.11 of the main text,

$$V_i = \Im \left[\langle \partial_i \phi | H | \phi \rangle - \langle \partial_i \phi | \phi \rangle \langle \phi | H | \phi \rangle \right] = \langle T_i | H | \phi \rangle \quad (\text{B.5})$$

B.2 Exact limit of the VAH ansatz

In this section we show that, when using the VHA ansatz (Eq. 6.14), McLachlan-VQS solution coincide with the exact evolution for vanishingly small times. At $t=0$, the partial derivative of

Appendix B.

the VHA with respect to the parameter θ_m is

$$|\partial_m \phi\rangle \Big|_{t=0} = -i P_m |\phi_0\rangle ; \quad (\text{B.6})$$

this means that

$$H|\phi_0\rangle = \sum_m c_m P_m |\phi_0\rangle = \sum_m i c_m |\partial_m \phi\rangle . \quad (\text{B.7})$$

Therefore

$$\langle T_l | H | \phi_0 \rangle = \sum_m i c_m \langle T_l | \partial_m \phi \rangle = \sum_m i c_m \langle T_l | T_m \rangle . \quad (\text{B.8})$$

If the c_m are reals, then

$$\Im[V_l] = \sum_m c_m \Re[\langle T_l | T_m \rangle] . \quad (\text{B.9})$$

Substituting Eq. B.9 in Eq. 6.13 of the main text, we obtain

$$\Re[\langle T_l | T_m \rangle] \dot{\theta}_m = c_m \Re[\langle T_l | T_m \rangle] \quad (\text{B.10})$$

which admit as solution

$$\dot{\theta}_m = c_m , \quad (\text{B.11})$$

therefore

$$\theta_m(t) = c_m t + o(t^2), \quad (\text{B.12})$$

B.3 Algebraic properties of Pauli matrices

Let us consider two n -dimensional Pauli operators, P, P' . We can write (without restriction)

$$P = P_1 P_2 \dots P_m P_{m+1} \dots P_n$$

$$P' = P'_1 P'_2 \dots P'_m P'_{m+1} \dots P'_n$$

where the first corresponding m operators of P and P' are Pauli operators which are different from each other and from identity (e.g $P_1 = X$, $P'_1 = Y$) and the corresponding operators from $m+1$ to n are either equal to each other or one of them is equal to the identity (e.g $P_n = I$, $P'_n = Y$ or $P_n = Y$, $P'_n = Y$). We have that

$$PP' = (i\varepsilon_{11'1''} P''_1) \dots (i\varepsilon_{mm'm''} P''_m) (P_{m+1} P'_{m+1} \dots P_n P'_n) \quad (\text{B.13})$$

$$\begin{aligned} [P, P'] &= (i\varepsilon_{11'1''} P''_1) \dots (i\varepsilon_{mm'm''} P''_m) (P_{m+1} P'_{m+1} \dots P_n P'_n) \\ &\quad - (-i\varepsilon_{11'1''} P''_1) \dots (-i\varepsilon_{mm'm''} P''_m) (P_{m+1} P'_{m+1} \dots P_n P'_n) \\ &\implies [P, P'] = PP' (1 - (-1)^m) \end{aligned} \quad (\text{B.14})$$

So, if m is even, then the commutator is vanishes. If, m is odd, then $[P, P'] = 2PP'$.

B.4 Pauli weight of Hubbard models

The n -site Hubbard chain with first-nearest neighbours hopping and time reversal symmetry has the following Hamiltonian:

$$\begin{aligned} \hat{H} = & -t \sum_{i=1}^{n-1} \sum_{\sigma=\uparrow,\downarrow} (\hat{c}_{i,\sigma}^\dagger \hat{c}_{i+1,\sigma} + \hat{c}_{i+1,\sigma} \hat{c}_{i,\sigma}^\dagger) \\ & + U \sum_{i=1}^n \hat{c}_{i\uparrow}^\dagger \hat{c}_{i\uparrow} \hat{c}_{i\downarrow}^\dagger \hat{c}_{i\downarrow} - \frac{U}{2} \sum_{i=1}^n \sum_{\sigma=\uparrow,\downarrow} \hat{c}_{i\sigma}^\dagger \hat{c}_{i\sigma}, \end{aligned} \quad (\text{B.15})$$

where n is the number of sites. The Wigner-Jordan transformation maps this Hamiltonian into the following set of $2n$ -qubit Pauli gates, denoted by H_n

$$H_n = H_n^{(1)} \cup H_n^{(2)}. \quad (\text{B.16})$$

The elements of $H_n^{(1)}$ have the form

$$e_x = \text{III} \dots \text{XZX} \dots \text{II} \quad (\text{B.17})$$

and

$$e_y = \text{III} \dots \text{YZY} \dots \text{II}, \quad (\text{B.18})$$

where the triplet XZX and YZY can assume any position in the qubit register. The number of elements of this set are thus $4(n-1)$, and their weight is $w = 3$. The elements of $H_n^{(2)}$, instead, have the form

$$e_z = \text{II} \dots \text{ZZ} \dots \text{II}, \quad (\text{B.19})$$

with an even number of identities I before and/or after the doublet ZZ. The number of elements of this set are thus n , and their weight is $w = 2$. The average Pauli weight is

$$\bar{w} = \frac{4(n-1) \times 3 + n \times 2}{4(n-1) + n} = \frac{14n - 12}{5n - 4} \quad (\text{B.20})$$

whose asymptotic value is $\bar{w}=2.8$. When replacing open-boundary conditions with periodic-boundary condition, the hopping between the first and the n -th site cause the appearance of terms such as $e_x = \text{ZXZZZ} \dots \text{ZX}$, where the Z gates act on all the central qubits, so the weight is maximum $w = 2n$. The same condition holds when the Hubbard sites are not displaced on a row (Hubbard chain) but on a 2d or even on a 3d lattice, increasing remarkably the average Pauli weight of the problem.

Bibliography

- [1] Francesco Libbi, Nicola Bonini, and Nicola Marzari. Thermomechanical properties of honeycomb lattices from internal-coordinates potentials: the case of graphene and hexagonal boron nitride. *2D Materials*, 8(1):015026, 2020.
- [2] Dimitrios G. Papageorgiou, Ian A. Kinloch, and Robert J. Young. Mechanical properties of graphene and graphene-based nanocomposites. *Progress in Materials Science*, 90:75–127, 2017.
- [3] K.I. Bolotin, K.J. Sikes, Z. Jiang, M. Klima, G. Fudenberg, J. Hone, P. Kim, and H.L. Stormer. Ultrahigh electron mobility in suspended graphene. *Solid State Communications*, 146(9):351–355, 2008.
- [4] Michael A. Nielsen and Isaac L. Chuang. *Quantum Computation and Quantum Information: 10th Anniversary Edition*. Cambridge University Press, 2011.
- [5] Gabriel Popkin. Quest for qubits. *Science*, 354(6316):1090–1093, 2016.
- [6] L. Childress, M. V. Gurudev Dutt, J. M. Taylor, A. S. Zibrov, F. Jelezko, J. Wrachtrup, P. R. Hemmer, and M. D. Lukin. Coherent dynamics of coupled electron and nuclear spin qubits in diamond. *Science*, 314(5797):281–285, 2006.
- [7] W. Pfaff, B. J. Hensen, H. Bernien, S. B. van Dam, M. S. Blok, T. H. Taminiau, M. J. Tiggelman, R. N. Schouten, M. Markham, D. J. Twitchen, and R. Hanson. Unconditional quantum teleportation between distant solid-state quantum bits. *Science*, 345(6196):532–535, 2014.
- [8] L. Childress, J. M. Taylor, A. S. Sørensen, and M. D. Lukin. Fault-tolerant quantum communication based on solid-state photon emitters. *Phys. Rev. Lett.*, 96:070504, Feb 2006.
- [9] L. T. Hall, J. H. Cole, C. D. Hill, and L. C. L. Hollenberg. Sensing of fluctuating nanoscale magnetic fields using nitrogen-vacancy centers in diamond. *Phys. Rev. Lett.*, 103:220802, Nov 2009.
- [10] G. de Lange, D. Ristè, V. V. Dobrovitski, and R. Hanson. Single-spin magnetometry with multipulse sensing sequences. *Phys. Rev. Lett.*, 106:080802, Feb 2011.

- [11] Florian Dolde, Marcus W. Doherty, Julia Michl, Ingmar Jakobi, Boris Naydenov, Sebastien Pezzagna, Jan Meijer, Philipp Neumann, Fedor Jelezko, Neil B. Manson, and Jörg Wrachtrup. Nanoscale detection of a single fundamental charge in ambient conditions using the NV^- center in diamond. *Phys. Rev. Lett.*, 112:097603, Mar 2014.
- [12] Marcus W. Doherty, Viktor V. Struzhkin, David A. Simpson, Liam P. McGuinness, Yufei Meng, Alastair Stacey, Timothy J. Karle, Russell J. Hemley, Neil B. Manson, Lloyd C. L. Hollenberg, and Steven Prawer. Electronic properties and metrology applications of the diamond nv^- center under pressure. *Phys. Rev. Lett.*, 112:047601, Jan 2014.
- [13] P. Neumann, I. Jakobi, F. Dolde, C. Burk, R. Reuter, G. Waldherr, J. Honert, T. Wolf, A. Brunner, J. H. Shim, D. Suter, H. Sumiya, J. Isoya, and J. Wrachtrup. High-precision nanoscale temperature sensing using single defects in diamond. *Nano Letters*, 13(6):2738–2742, Jun 2013.
- [14] Andreas Gottscholl, Mehran Kianinia, Victor Soltamov, Sergei Orlinskii, Georgy Mamin, Carlo Bradac, Christian Kasper, Klaus Krambrock, Andreas Sperlich, Milos Toth, Igor Aharonovich, and Vladimir Dyakonov. Initialization and read-out of intrinsic spin defects in a van der waals crystal at room temperature. *Nature Materials*, 2020.
- [15] F. Giustino. *Materials Modelling Using Density Functional Theory: Properties and Predictions*. Oxford University Press, 2014.
- [16] Paolo Giannozzi, Stefano Baroni, Nicola Bonini, Matteo Calandra, Roberto Car, Carlo Cavazzoni, Davide Ceresoli, Guido L Chiarotti, Matteo Cococcioni, Ismaila Dabo, Andrea Dal Corso, Stefano de Gironcoli, Stefano Fabris, Guido Fratesi, Ralph Gebauer, Uwe Gerstmann, Christos Gougoussis, Anton Kokalj, Michele Lazzeri, Layla Martin-Samos, Nicola Marzari, Francesco Mauri, Riccardo Mazzarello, Stefano Paolini, Alfredo Pasquarello, Lorenzo Paulatto, Carlo Sbraccia, Sandro Scandolo, Gabriele Sclauszero, Ari P Seitsonen, Alexander Smogunov, Paolo Umari, and Renata M Wentzcovitch. QUANTUM ESPRESSO: a modular and open-source software project for quantum simulations of materials. *Journal of Physics: Condensed Matter*, 21(39):395502, sep 2009.
- [17] A. L. Fetter and J. D. Walecka. *Quantum Theory of Many-Particle Systems*. McGraw-Hill, Boston, 1971.
- [18] Gerald D. Mahan. *Many-particle physics / Gerald D. Mahan*. Plenum Press New York, 1981.
- [19] G. Stefanucci and R. van Leeuwen. *Nonequilibrium Many-Body theory of Quantum Systems*. Cambridge University Press, Boston, 2013.
- [20] P. Hohenberg and W. Kohn. Inhomogeneous electron gas. *Phys. Rev.*, 136:B864–B871, Nov 1964.
- [21] W. Kohn and L. J. Sham. Self-consistent equations including exchange and correlation effects. *Phys. Rev.*, 140:A1133–A1138, Nov 1965.

-
- [22] Junwei Lucas Bao, Laura Gagliardi, and Donald G. Truhlar. Self-interaction error in density functional theory: An appraisal. *The Journal of Physical Chemistry Letters*, 9(9):2353–2358, May 2018.
- [23] Tomáš Bučko, Jürgen Hafner, Sébastien Lebègue, and János G. Ángyán. Improved description of the structure of molecular and layered crystals: Ab initio dft calculations with van der waals corrections. *The Journal of Physical Chemistry A*, 114(43):11814–11824, Nov 2010.
- [24] John P. Perdew. Density functional theory and the band gap problem. *International Journal of Quantum Chemistry*, 28(S19):497–523, 1985.
- [25] Lars Hedin. New method for calculating the one-particle green’s function with application to the electron-gas problem. *Physical Review*, 139(3A):A796, 1965.
- [26] Aleta Berk Finnila, MA Gomez, C Sebenik, Catherine Stenson, and Jimmie D Doll. Quantum annealing: A new method for minimizing multidimensional functions. *Chemical physics letters*, 219(5-6):343–348, 1994.
- [27] M. van Schilfgaarde, Takao Kotani, and S. Faleev. Quasiparticle self-consistent *gw* theory. *Phys. Rev. Lett.*, 96:226402, Jun 2006.
- [28] Giancarlo Strinati. Application of the green’s functions method to the study of the optical properties of semiconductors. *La Rivista del Nuovo Cimento (1978-1999)*, 11(12):1–86, 1988.
- [29] Giovanni Onida, Lucia Reining, and Angel Rubio. Electronic excitations: density-functional versus many-body green’s-function approaches. *Reviews of modern physics*, 74(2):601, 2002.
- [30] K. Hannewald, S. Glutsch, and F. Bechstedt. Theory of photoluminescence in semiconductors. *Phys. Rev. B*, 62:4519–4525, Aug 2000.
- [31] Radi A Jishi. *Feynman diagram techniques in condensed matter physics*. Cambridge University Press, 2013.
- [32] David C. Langreth. *Linear and Nonlinear Response Theory with Applications*, pages 3–32. Springer US, Boston, MA, 1976.
- [33] Pedro Miguel M. C. de Melo and Andrea Marini. Unified theory of quantized electrons, phonons, and photons out of equilibrium: A simplified ab initio approach based on the generalized baym-kadanoff ansatz. *Phys. Rev. B*, 93:155102, Apr 2016.
- [34] E. Perfetto, D. Sangalli, A. Marini, and G. Stefanucci. Nonequilibrium bethe-salpeter equation for transient photoabsorption spectroscopy. *Phys. Rev. B*, 92:205304, Nov 2015.

Bibliography

- [35] André Schleife, Claudia Rödl, Frank Fuchs, Karsten Hannewald, and Friedhelm Bechstedt. Optical absorption in degenerately doped semiconductors: Mott transition or mahan excitons? *Phys. Rev. Lett.*, 107:236405, Nov 2011.
- [36] E. Cannuccia, B. Monserrat, and C. Attacalite. Theory of phonon-assisted luminescence in solids: Application to hexagonal boron nitride. *Phys. Rev. B*, 99:081109, Feb 2019.
- [37] Scott Aaronson and Daniel Gottesman. Improved simulation of stabilizer circuits. *Phys. Rev. A*, 70:052328, Nov 2004.
- [38] Emanuel Knill and Raymond Laflamme. Theory of quantum error-correcting codes. *Physical Review A*, 55(2):900, 1997.
- [39] M. W. Johnson, M. H. S. Amin, S. Gildert, T. Lanting, F. Hamze, N. Dickson, R. Harris, A. J. Berkley, J. Johansson, P. Bunyk, E. M. Chapple, C. Enderud, J. P. Hilton, K. Karimi, E. Ladizinsky, N. Ladizinsky, T. Oh, I. Perminov, C. Rich, M. C. Thom, E. Tolkacheva, C. J. S. Truncik, S. Uchaikin, J. Wang, B. Wilson, and G. Rose. Quantum annealing with manufactured spins. *Nature*, 473(7346):194–198, May 2011.
- [40] Frank Arute, Kunal Arya, Ryan Babbush, Dave Bacon, Joseph C. Bardin, Rami Barends, Rupak Biswas, Sergio Boixo, Fernando G. S. L. Brandao, David A. Buell, Brian Burkett, Yu Chen, Zijun Chen, Ben Chiaro, Roberto Collins, William Courtney, Andrew Dunsworth, Edward Farhi, Brooks Foxen, Austin Fowler, Craig Gidney, Marissa Giustina, Rob Graff, Keith Guerin, Steve Habegger, Matthew P. Harrigan, Michael J. Hartmann, Alan Ho, Markus Hoffmann, Trent Huang, Travis S. Humble, Sergei V. Isakov, Evan Jeffrey, Zhang Jiang, Dvir Kafri, Kostyantyn Kechedzhi, Julian Kelly, Paul V. Klimov, Sergey Knysh, Alexander Korotkov, Fedor Kostritsa, David Landhuis, Mike Lindmark, Erik Lucero, Dmitry Lyakh, Salvatore Mandrà, Jarrod R. McClean, Matthew McEwen, Anthony Megrant, Xiao Mi, Kristel Michielsen, Masoud Mohseni, Josh Mutus, Ofer Naeaman, Matthew Neeley, Charles Neill, Murphy Yuezhen Niu, Eric Ostby, Andre Petukhov, John C. Platt, Chris Quintana, Eleanor G. Rieffel, Pedram Roushan, Nicholas C. Rubin, Daniel Sank, Kevin J. Satzinger, Vadim Smelyanskiy, Kevin J. Sung, Matthew D. Trevithick, Amit Vainsencher, Benjamin Villalonga, Theodore White, Z. Jamie Yao, Ping Yeh, Adam Zalcman, Hartmut Neven, and John M. Martinis. Quantum supremacy using a programmable superconducting processor. *Nature*, 574(7779):505–510, Oct 2019.
- [41] Frank Arute, Kunal Arya, Ryan Babbush, Dave Bacon, Joseph C Bardin, Rami Barends, Rupak Biswas, Sergio Boixo, Fernando GSL Brandao, David A Buell, et al. Quantum supremacy using a programmable superconducting processor. *Nature*, 574(7779):505–510, 2019.
- [42] Nicolai Friis, Oliver Marty, Christine Maier, Cornelius Hempel, Milan Holzäpfel, Petar Jurcevic, Martin B. Plenio, Marcus Huber, Christian Roos, Rainer Blatt, and Ben Lanyon. Observation of entangled states of a fully controlled 20-qubit system. *Phys. Rev. X*, 8:021012, Apr 2018.

- [43] Ehud Altman, Kenneth R. Brown, Giuseppe Carleo, Lincoln D. Carr, Eugene Demler, Cheng Chin, Brian DeMarco, Sophia E. Economou, Mark A. Eriksson, Kai-Mei C. Fu, Markus Greiner, Kaden R.A. Hazzard, Randall G. Hulet, Alicia J. Kollár, Benjamin L. Lev, Mikhail D. Lukin, Ruichao Ma, Xiao Mi, Shashank Misra, Christopher Monroe, Kater Murch, Zaira Nazario, Kang-Kuen Ni, Andrew C. Potter, Pedram Roushan, Mark Saffman, Monika Schleier-Smith, Irfan Siddiqi, Raymond Simmonds, Meenakshi Singh, I.B. Spielman, Kristan Temme, David S. Weiss, Jelena Vučković, Vladan Vuletić, Jun Ye, and Martin Zwierlein. Quantum simulators: Architectures and opportunities. *PRX Quantum*, 2:017003, Feb 2021.
- [44] J. M. Arrazola, V. Bergholm, K. Brádler, T. R. Bromley, M. J. Collins, I. Dhand, A. Fumagalli, T. Gerrits, A. Goussev, L. G. Helt, J. Hundal, T. Isacsson, R. B. Israel, J. Izaac, S. Jahangiri, R. Janik, N. Killoran, S. P. Kumar, J. Lavoie, A. E. Lita, D. H. Mahler, M. Menotti, B. Morrison, S. W. Nam, L. Neuhaus, H. Y. Qi, N. Quesada, A. Repington, K. K. Sabapathy, M. Schuld, D. Su, J. Swinerton, A. Száva, K. Tan, P. Tan, V. D. Vaidya, Z. Vernon, Z. Zabaneh, and Y. Zhang. Quantum circuits with many photons on a programmable nanophotonic chip. *Nature*, 591(7848):54–60, Mar 2021.
- [45] J. Eli Bourassa, Rafael N. Alexander, Michael Vasmer, Ashlesha Patil, Ilan Tzitrin, Takaya Matsuura, Daiqin Su, Ben Q. Baragiola, Saikat Guha, Guillaume Dauphinais, Krishna K. Sabapathy, Nicolas C. Menicucci, and Ish Dhand. Blueprint for a Scalable Photonic Fault-Tolerant Quantum Computer. *Quantum*, 5:392, February 2021.
- [46] Y. He, S. K. Gorman, D. Keith, L. Kranz, J. G. Keizer, and M. Y. Simmons. A two-qubit gate between phosphorus donor electrons in silicon. *Nature*, 571(7765):371–375, Jul 2019.
- [47] Daniel Loss and David P. DiVincenzo. Quantum computation with quantum dots. *Phys. Rev. A*, 57:120–126, Jan 1998.
- [48] Hannes Bernien, Sylvain Schwartz, Alexander Keesling, Harry Levine, Ahmed Omran, Hannes Pichler, Soonwon Choi, Alexander S. Zibrov, Manuel Endres, Markus Greiner, Vladan Vuletić, and Mikhail D. Lukin. Probing many-body dynamics on a 51-atom quantum simulator. *Nature*, 551(7682):579–584, Nov 2017.
- [49] David P. DiVincenzo. The physical implementation of quantum computation. *Fortschritte der Physik*, 48(9-11):771–783, 2000.
- [50] Mark R. Hoffmann and Jack Simons. A unitary multiconfigurational coupled-cluster method: Theory and applications. *The Journal of Chemical Physics*, 88(2):993–1002, 1988.
- [51] T. P. Orlando, J. E. Mooij, Lin Tian, Caspar H. van der Wal, L. S. Levitov, Seth Lloyd, and J. J. Mazo. Superconducting persistent-current qubit. *Phys. Rev. B*, 60:15398–15413, Dec 1999.

- [52] J. Q. You and Franco Nori. Superconducting circuits and quantum information. *Physics Today*, 58(11):42–47, 2005.
- [53] Vladimir E. Manucharyan, Jens Koch, Leonid I. Glazman, and Michel H. Devoret. Fluxonium: Single cooper-pair circuit free of charge offsets. *Science*, 326(5949):113–116, 2009.
- [54] A. A. Houck, Jens Koch, M. H. Devoret, S. M. Girvin, and R. J. Schoelkopf. Life after charge noise: recent results with transmon qubits. *Quantum Information Processing*, 8(2):105–115, Jun 2009.
- [55] R. Barends, J. Kelly, A. Megrant, D. Sank, E. Jeffrey, Y. Chen, Y. Yin, B. Chiaro, J. Mutus, C. Neill, P. O’Malley, P. Roushan, J. Wenner, T. C. White, A. N. Cleland, and John M. Martinis. Coherent josephson qubit suitable for scalable quantum integrated circuits. *Phys. Rev. Lett.*, 111:080502, Aug 2013.
- [56] M. Metcalfe, E. Boaknin, V. Manucharyan, R. Vijay, I. Siddiqi, C. Rigetti, L. Frunzio, R. J. Schoelkopf, and M. H. Devoret. Measuring the decoherence of a quantronium qubit with the cavity bifurcation amplifier. *Phys. Rev. B*, 76:174516, Nov 2007.
- [57] Petar Jurcevic, Ali Javadi-Abhari, Lev S Bishop, Isaac Lauer, Daniela F Bogorin, Markus Brink, Lauren Capelluto, Oktay Günlük, Toshinari Itoko, Naoki Kanazawa, Abhinav Kandala, George A Keefe, Kevin Krsulich, William Landers, Eric P Lewandowski, Douglas T McClure, Giacomo Nannicini, Adinath Narasgond, Hasan M Nayfeh, Emily Pritchett, Mary Beth Rothwell, Srikanth Srinivasan, Neereja Sundaresan, Cindy Wang, Ken X Wei, Christopher J Wood, Jeng-Bang Yau, Eric J Zhang, Oliver E Dial, Jerry M Chow, and Jay M Gambetta. Demonstration of quantum volume 64 on a superconducting quantum computing system. *Quantum Science and Technology*, 6(2):025020, mar 2021.
- [58] P Krantz, M. Kjaergaard, F. Yan, T. P. Orlando, S. Gustavsson, and W. D. Oliver. A quantum engineer’s guide to superconducting qubits. *Applied Physics Reviews*, 6(2):021318, 2019.
- [59] Alexandre Blais, Arne L. Grimsmo, S. M. Girvin, and Andreas Wallraff. Circuit quantum electrodynamics. *Rev. Mod. Phys.*, 93:025005, May 2021.
- [60] David C. McKay, Christopher J. Wood, Sarah Sheldon, Jerry M. Chow, and Jay M. Gambetta. Efficient z gates for quantum computing. *Phys. Rev. A*, 96:022330, Aug 2017.
- [61] Petr Siyushev, Milos Nesladek, Emilie Bourgeois, Michal Gulka, Jaroslav Hruby, Takashi Yamamoto, Michael Trupke, Tokuyuki Teraji, Junichi Isoya, and Fedor Jelezko. Photoelectrical imaging and coherent spin-state readout of single nitrogen-vacancy centers in diamond. *Science*, 363(6428):728–731, 2019.
- [62] Gary Wolfowicz, F. Joseph Heremans, Christopher P. Anderson, Shun Kanai, Hosung Seo, Adam Gali, Giulia Galli, and David D. Awschalom. Quantum guidelines for solid-state spin defects. *Nature Reviews Materials*, 6(10):906–925, Oct 2021.

- [63] Gopalakrishnan Balasubramanian, Philipp Neumann, Daniel Twitchen, Matthew Markham, Roman Kolesov, Norikazu Mizuochi, Junichi Isoya, Jocelyn Achard, Johannes Beck, Julia Tissler, Vincent Jacques, Philip R. Hemmer, Fedor Jelezko, and Jörg Wrachtrup. Ultralong spin coherence time in isotopically engineered diamond. *Nature Materials*, 8(5):383–387, May 2009.
- [64] Adam Gali, Maria Fyta, and Efthimios Kaxiras. Ab initio supercell calculations on nitrogen-vacancy center in diamond: Electronic structure and hyperfine tensors. *Phys. Rev. B*, 77:155206, Apr 2008.
- [65] G. Davies, M. F. Hamer, and William Charles Price. Optical studies of the 1.945 eV vibronic band in diamond. *Proceedings of the Royal Society of London. A. Mathematical and Physical Sciences*, 348(1653):285–298, 1976.
- [66] J. P. Goss, R. Jones, S. J. Breuer, P. R. Briddon, and S. Öberg. The twelve-line 1.682 eV luminescence center in diamond and the vacancy-silicon complex. *Phys. Rev. Lett.*, 77:3041–3044, Sep 1996.
- [67] Adam Gali, Erik Janzén, Péter Deák, Georg Kresse, and Efthimios Kaxiras. Theory of spin-conserving excitation of the $n - V^-$ center in diamond. *Phys. Rev. Lett.*, 103:186404, Oct 2009.
- [68] Paul Delaney, James C. Greer, and J. Andreas Larsson. Spin-polarization mechanisms of the nitrogen-vacancy center in diamond. *Nano Letters*, 10(2):610–614, Feb 2010.
- [69] Yuchen Ma, Michael Rohlfing, and Adam Gali. Excited states of the negatively charged nitrogen-vacancy color center in diamond. *Phys. Rev. B*, 81:041204, Jan 2010.
- [70] F. Jelezko and J. Wrachtrup. Single defect centres in diamond: A review. *physica status solidi (a)*, 203(13):3207–3225, 2006.
- [71] M. Steiner, P. Neumann, J. Beck, F. Jelezko, and J. Wrachtrup. Universal enhancement of the optical readout fidelity of single electron spins at nitrogen-vacancy centers in diamond. *Phys. Rev. B*, 81:035205, Jan 2010.
- [72] J. R. Maze, J. M. Taylor, and M. D. Lukin. Electron spin decoherence of single nitrogen-vacancy defects in diamond. *Phys. Rev. B*, 78:094303, Sep 2008.
- [73] L. Jiang, M. V. Gurudev Dutt, E. Togan, L. Childress, P. Cappellaro, J. M. Taylor, and M. D. Lukin. Coherence of an optically illuminated single nuclear spin qubit. *Phys. Rev. Lett.*, 100:073001, Feb 2008.
- [74] M. V. Gurudev Dutt, L. Childress, L. Jiang, E. Togan, J. Maze, F. Jelezko, A. S. Zibrov, P. R. Hemmer, and M. D. Lukin. Quantum register based on individual electronic and nuclear spin qubits in diamond. *Science*, 316(5829):1312–1316, 2007.

- [75] L. Childress, M. V. Gurudev Dutt, J. M. Taylor, A. S. Zibrov, F. Jelezko, J. Wrachtrup, P. R. Hemmer, and M. D. Lukin. Coherent dynamics of coupled electron and nuclear spin qubits in diamond. *Science*, 314(5797):281–285, 2006.
- [76] F. Jelezko, T. Gaebel, I. Popa, M. Domhan, A. Gruber, and J. Wrachtrup. Observation of coherent oscillation of a single nuclear spin and realization of a two-qubit conditional quantum gate. *Phys. Rev. Lett.*, 93:130501, Sep 2004.
- [77] J R Weber, W F Koehl, J B Varley, A Janotti, B B Buckley, C G Van de Walle, and D D Awschalom. Quantum computing with defects. *Proc Natl Acad Sci U S A*, 107(19):8513–8518, April 2010.
- [78] H. J. von Bardeleben, J. L. Cantin, E. Rauls, and U. Gerstmann. Identification and magneto-optical properties of the nv center in 4h – SiC. *Phys. Rev. B*, 92:064104, Aug 2015.
- [79] Y. Tu, Z. Tang, X. G. Zhao, Y. Chen, Z. Q. Zhu, J. H. Chu, and J. C. Fang. A paramagnetic neutral valon center in wurtzite aln for spin qubit application. *Applied Physics Letters*, 103(7):072103, 2013.
- [80] Hosung Seo, Marco Govoni, and Giulia Galli. Design of defect spins in piezoelectric aluminum nitride for solid-state hybrid quantum technologies. *Scientific Reports*, 6(1):20803, Feb 2016.
- [81] Yong Zhang, Wen Liu, and Hanben Niu. Native defect properties and p -type doping efficiency in group-ii-a doped wurtzite aln. *Phys. Rev. B*, 77:035201, Jan 2008.
- [82] Hosung Seo, He Ma, Marco Govoni, and Giulia Galli. Designing defect-based qubit candidates in wide-gap binary semiconductors for solid-state quantum technologies. *Phys. Rev. Materials*, 1:075002, Dec 2017.
- [83] Mehran Kianinia, Simon White, Johannes E. Fröch, Carlo Bradac, and Igor Aharonovich. Generation of spin defects in hexagonal boron nitride. *ACS Photonics*, 7(8):2147–2152, Aug 2020.
- [84] Noah Mendelson, Dipankar Chugh, Jeffrey R. Reimers, Tin S. Cheng, Andreas Gottscholl, Hu Long, Christopher J. Mellor, Alex Zettl, Vladimir Dyakonov, Peter H. Beton, Sergei V. Novikov, Chennupati Jagadish, Hark Hoe Tan, Michael J. Ford, Milos Toth, Carlo Bradac, and Igor Aharonovich. Identifying carbon as the source of visible single-photon emission from hexagonal boron nitride. *Nature Materials*, Nov 2020.
- [85] Romain Bourrellier, Sophie Meuret, Anna Tararan, Odile Stéphan, Mathieu Kociak, Luiz H. G. Tizei, and Alberto Zobelli. Bright uv single photon emission at point defects in h-bn. *Nano Letters*, 16(7):4317–4321, Jul 2016.
- [86] Luc Museur, Eduard Feldbach, and Andrei Kanaev. Defect-related photoluminescence of hexagonal boron nitride. *Phys. Rev. B*, 78:155204, Oct 2008.

-
- [87] Meng Ye, Hosung Seo, and Giulia Galli. Spin coherence in two-dimensional materials. *npj Computational Materials*, 5(1):44, Apr 2019.
- [88] K Huang and A Rhys. Theory of light absorption and non-radiative transitions in f-centres. *Proc. R. Soc. Lond. A*, 204:406–423, Dec 1950.
- [89] Audrius Alkauskas, Bob B Buckley, David D Awschalom, and Chris G Van de Walle. 16(7):073026, jul 2014.
- [90] Viktor Ivády, Gergely Barcza, Gergő Thiering, Song Li, Hanen Hamdi, Jyh-Pin Chou, Örs Legeza, and Adam Galli. Ab initio theory of the negatively charged boron vacancy qubit in hexagonal boron nitride. *npj Computational Materials*, 6(1):41, Apr 2020.
- [91] Stefano Barison, Filippo Vicentini, and Giuseppe Carleo. An efficient quantum algorithm for the time evolution of parameterized circuits. *Quantum*, 5:512, Jul 2021.
- [92] Thomas H. Keil. Shapes of impurity absorption bands in solids. *Phys. Rev.*, 140:A601–A617, Oct 1965.
- [93] Melvin Lax. The franckâcondon principle and its application to crystals. *The Journal of Chemical Physics*, 20(11):1752–1760, 1952.
- [94] Jeffrey R. Reimers, Jun Shen, Mehran Kianinia, Carlo Bradac, Igor Aharonovich, Michael J. Ford, and Piotr Piecuch. Photoluminescence, photophysics, and photochemistry of the V_B^- defect in hexagonal boron nitride. *Phys. Rev. B*, 102:144105, Oct 2020.
- [95] Yu Jin, Marco Govoni, Gary Wolfowicz, Sean E Sullivan, F Joseph Heremans, David D Awschalom, and Giulia Galli. Photoluminescence spectra of point defects in semiconductors: Validation of first-principles calculations. *Physical Review Materials*, 5(8):084603, 2021.
- [96] Lorenzo Sponza, Hakim Amara, Fran çois Ducastelle, Annick Loiseau, and Claudio Attaccalite. Exciton interference in hexagonal boron nitride. *Phys. Rev. B*, 97:075121, Feb 2018.
- [97] Lorenzo Sponza, Hakim Amara, Claudio Attaccalite, Sylvain Latil, Thomas Galvani, Fulvio Paleari, Ludger Wirtz, and Fran çois Ducastelle. Direct and indirect excitons in boron nitride polymorphs: A story of atomic configuration and electronic correlation. *Phys. Rev. B*, 98:125206, Sep 2018.
- [98] Fulvio Paleari, Henrique P. C. Miranda, Alejandro Molina-Sánchez, and Ludger Wirtz. Exciton-phonon coupling in the ultraviolet absorption and emission spectra of bulk hexagonal boron nitride. *Phys. Rev. Lett.*, 122:187401, May 2019.
- [99] Léonard Schué, Lorenzo Sponza, Alexandre Plaud, Hakima Bensalah, Kenji Watanabe, Takashi Taniguchi, Fran çois Ducastelle, Annick Loiseau, and Julien Barjon. Bright luminescence from indirect and strongly bound excitons in h-bn. *Phys. Rev. Lett.*, 122:067401, Feb 2019.

Bibliography

- [100] M.J. [van Setten], M. Giantomassi, E. Bousquet, M.J. Verstraete, D.R. Hamann, X. Gonze, and G.-M. Rignanese. The pseudodojo: Training and grading a 85 element optimized norm-conserving pseudopotential table. *Computer Physics Communications*, 226:39 – 54, 2018.
- [101] Dorothea Golze, Marc Dvorak, and Patrick Rinke. The gw compendium: A practical guide to theoretical photoemission spectroscopy. *Frontiers in Chemistry*, 7:377, 2019.
- [102] Andrea Marini, Conor Hogan, Myrta GrACening, and Daniele Varsano. yambo: An ab initio tool for excited state calculations. *Computer Physics Communications*, 180(8):1392 – 1403, 2009.
- [103] Davide Sangalli, Andrea Ferretti, Henrique Miranda, Claudio Attaccalite, Ivan Marri, Elena Cannuccia, P Melo, Margherita Marsili, Fulvio Paleari, Antimo Marrazzo, et al. Many-body perturbation theory calculations using the yambo code. *Journal of Physics: Condensed Matter*, 31(32):325902, 2019.
- [104] G. Cassabois, P. Valvin, and B. Gil. Hexagonal boron nitride is an indirect bandgap semiconductor. *Nature Photonics*, 10(4):262–266, Apr 2016.
- [105] Carlo A. Rozzi, Daniele Varsano, Andrea Marini, Eberhard K. U. Gross, and Angel Rubio. Exact coulomb cutoff technique for supercell calculations. *Phys. Rev. B*, 73:205119, May 2006.
- [106] C. Attaccalite, M. Bockstedte, A. Marini, A. Rubio, and L. Wirtz. Coupling of excitons and defect states in boron-nitride nanostructures. *Phys. Rev. B*, 83:144115, Apr 2011.
- [107] G. Makov and M. C. Payne. Periodic boundary conditions in ab initio calculations. *Phys. Rev. B*, 51:4014–4022, Feb 1995.
- [108] Christoph Freysoldt, Jörg Neugebauer, and Chris G. Van de Walle. Fully ab initio finite-size corrections for charged-defect supercell calculations. *Phys. Rev. Lett.*, 102:016402, Jan 2009.
- [109] Francesco Libbi, Pedro Miguel MC de Melo, Zeila Zanolli, Matthieu Jean Verstraete, and Nicola Marzari. Phonon-assisted luminescence in defect centers from many-body perturbation theory. *Physical Review Letters*, 128(16):167401, 2022.
- [110] Marios Zacharias, Christopher E Patrick, and Feliciano Giustino. Stochastic approach to phonon-assisted optical absorption. *Physical review letters*, 115(17):177401, 2015.
- [111] Marios Zacharias and Feliciano Giustino. One-shot calculation of temperature-dependent optical spectra and phonon-induced band-gap renormalization. *Physical Review B*, 94(7):075125, 2016.

-
- [112] Yongliang Chen, Thinh Ngoc Tran, Ngoc My Hanh Duong, Chi Li, Milos Toth, Carlo Bradac, Igor Aharonovich, Alexander Solntsev, and Toan Trong Tran. Optical thermometry with quantum emitters in hexagonal boron nitride. *ACS Applied Materials & Interfaces*, 12(22):25464–25470, Jun 2020.
- [113] A Togo and I Tanaka. First principles phonon calculations in materials science. *Scr. Mater.*, 108:1–5, Nov 2015.
- [114] Christopher E Patrick and Feliciano Giustino. Unified theory of electron–phonon renormalization and phonon-assisted optical absorption. *Journal of Physics: Condensed Matter*, 26(36):365503, aug 2014.
- [115] Feliciano Giustino. Electron-phonon interactions from first principles. *Rev. Mod. Phys.*, 89:015003, Feb 2017.
- [116] Stefano Baroni, Stefano de Gironcoli, Andrea Dal Corso, and Paolo Giannozzi. Phonons and related crystal properties from density-functional perturbation theory. *Rev. Mod. Phys.*, 73:515–562, Jul 2001.
- [117] Pui K. Lam, Michel M. Dacorogna, and Marvin L. Cohen. Self-consistent calculation of electron-phonon couplings. *Phys. Rev. B*, 34:5065–5069, Oct 1986.
- [118] K. Kunc and Richard M. Martin. Ab initio force constants of gaas: A new approach to calculation of phonons and dielectric properties. *Phys. Rev. Lett.*, 48:406–409, Feb 1982.
- [119] Warren E Pickett. Pseudopotential methods in condensed matter applications. *Computer Physics Reports*, 9(3):115–197, 1989.
- [120] DR Hamann, M Schlüter, and C Chiang. Norm-conserving pseudopotentials. *Physical Review Letters*, 43(20):1494, 1979.
- [121] DR Hamann. Optimized norm-conserving vanderbilt pseudopotentials. *Physical Review B*, 88(8):085117, 2013.
- [122] David Vanderbilt. Soft self-consistent pseudopotentials in a generalized eigenvalue formalism. *Physical review B*, 41(11):7892, 1990.
- [123] Francesco Libbi, Jacopo Rizzo, Francesco Tacchino, Nicola Marzari, and Ivano Tavernelli. Effective calculation of the green’s function in the time domain on near-term quantum processors. *arXiv preprint arXiv:2203.12372*, 2022.
- [124] Antoine Georges, Gabriel Kotliar, Werner Krauth, and Marcelo J. Rozenberg. Dynamical mean-field theory of strongly correlated fermion systems and the limit of infinite dimensions. *Rev. Mod. Phys.*, 68:13–125, Jan 1996.
- [125] Thomas E. Baker. Lanczos recursion on a quantum computer for the green’s function and ground state. *Phys. Rev. A*, 103:032404, Mar 2021.

Bibliography

- [126] Dave Wecker, Matthew B. Hastings, Nathan Wiebe, Bryan K. Clark, Chetan Nayak, and Matthias Troyer. Solving strongly correlated electron models on a quantum computer. *Phys. Rev. A*, 92:062318, Dec 2015.
- [127] Alessandro Roggero and Joseph Carlson. Dynamic linear response quantum algorithm. *Phys. Rev. C*, 100:034610, Sep 2019.
- [128] Taichi Kosugi and Yu-ichiro Matsushita. Construction of green's functions on a quantum computer: Quasiparticle spectra of molecules. *Phys. Rev. A*, 101:012330, Jan 2020.
- [129] Bela Bauer, Dave Wecker, Andrew J. Millis, Matthew B. Hastings, and Matthias Troyer. Hybrid quantum-classical approach to correlated materials. *Phys. Rev. X*, 6:031045, Sep 2016.
- [130] J. M. Kreula, S. R. Clark, and D. Jaksch. Non-linear quantum-classical scheme to simulate non-equilibrium strongly correlated fermionic many-body dynamics. *Scientific Reports*, 6(1):32940, Sep 2016.
- [131] A. Chiesa, F. Tacchino, M. Grossi, P. Santini, I. Tavernelli, D. Gerace, and S. Carretta. Quantum hardware simulating four-dimensional inelastic neutron scattering. *Nature Physics*, 15(5):455–459, May 2019.
- [132] Suguru Endo, Iori Kurata, and Yuya O. Nakagawa. Calculation of the green's function on near-term quantum computers. *Phys. Rev. Research*, 2:033281, Aug 2020.
- [133] Ken M. Nakanishi, Kosuke Mitarai, and Keisuke Fujii. Subspace-search variational quantum eigensolver for excited states. *Phys. Rev. Research*, 1:033062, Oct 2019.
- [134] Jacopo Rizzo, Francesco Libbi, Francesco Tacchino, Pauline J. Ollitrault, Nicola Marzari, and Ivano Tavernelli. One-particle green's functions from the quantum equation of motion algorithm, 2022.
- [135] Pauline J. Ollitrault, Abhinav Kandala, Chun-Fu Chen, Panagiotis Kl. Barkoutsos, Antonio Mezzacapo, Marco Pistoia, Sarah Sheldon, Stefan Woerner, Jay M. Gambetta, and Ivano Tavernelli. Quantum equation of motion for computing molecular excitation energies on a noisy quantum processor. *Phys. Rev. Research*, 2:043140, Oct 2020.
- [136] Xiao Yuan, Suguru Endo, Qi Zhao, Ying Li, and Simon C. Benjamin. Theory of variational quantum simulation. *Quantum*, 3:191, October 2019.
- [137] Dave Wecker, Matthew B. Hastings, and Matthias Troyer. Progress towards practical quantum variational algorithms. *Phys. Rev. A*, 92:042303, Oct 2015.
- [138] Jan-Michael Reiner, Frank Wilhelm-Mauch, Gerd Schön, and Michael Marthaler. Finding the ground state of the hubbard model by variational methods on a quantum computer with gate errors. 4(3):035005, may 2019.

-
- [139] Lucas Hackl, Tommaso Guaita, Tao Shi, Jutho Haegeman, Eugene Demler, and J. Ignacio Cirac. Geometry of variational methods: dynamics of closed quantum systems. *SciPost Phys.*, 9:48, 2020.
- [140] Michael Kolodrubetz, Dries Sels, Pankaj Mehta, and Anatoli Polkovnikov. Geometry and non-adiabatic response in quantum and classical systems. *Physics Reports*, 697:1–87, 2017. Geometry and non-adiabatic response in quantum and classical systems.
- [141] Marin Bukov, Dries Sels, and Anatoli Polkovnikov. Geometric speed limit of accessible many-body state preparation. *Phys. Rev. X*, 9:011034, Feb 2019.
- [142] Yuxuan Du, Min-Hsiu Hsieh, Tongliang Liu, and Dacheng Tao. Expressive power of parametrized quantum circuits. *Phys. Rev. Research*, 2:033125, Jul 2020.
- [143] Francesco Tacchino, Alessandro Chiesa, Stefano Carretta, and Dario Gerace. Quantum computers as universal quantum simulators: State-of-the-art and perspectives. *Advanced Quantum Technologies*, 3(3):1900052, 2020.
- [144] MD SAJID ANIS, Héctor Abraham, AduOfiei, Rochisha Agarwal, Gabriele Agliardi, and Merav Aharoni et. al. Qiskit: An open-source framework for quantum computing, 2021.
- [145] Sergey B. Bravyi and Alexei Yu. Kitaev. Fermionic quantum computation. *Annals of Physics*, 298(1):210–226, 2002.
- [146] Andrew Tranter, Peter J. Love, Florian Mintert, and Peter V. Coveney. A comparison of the bravyi–kitaev and jordan–wigner transformations for the quantum simulation of quantum chemistry. *Journal of Chemical Theory and Computation*, 14(11):5617–5630, 2018.
- [147] Paul D. Nation, Hwajung Kang, Neereja Sundaresan, and Jay M. Gambetta. Scalable mitigation of measurement errors on quantum computers. *PRX Quantum*, 2:040326, Nov 2021.
- [148] C. Neill et al. Accurately computing electronic properties of a quantum ring. *Nature*, 594(7864):508–512, June 2021.
- [149] Michael Tinkham. *Group theory and quantum mechanics*. Courier Corporation, 2003.



Curriculum vitae



Francesco Libbi

Mechanical engineer

Contacts

 Avenue de la Dole 3
 1005 Lausanne
 Switzerland
 +41 783412335
 francesco.libbi@epfl.ch

Languages

Italian

English

French

Interests

- ▶ Reading
- ▶ Sports
- ▶ Music

About me

During my career I explored many fields of science. After studying mechanical engineering, I devoted myself to quantum physics, researching in thermal transport, quantum information/computing and first-principles simulation of the optical properties of low dimensional materials.

Education

PhD Program in Materials Science and Engineering (EDMX)

4/2018 - today

École Polytechnique Fédérale de Lausanne, Switzerland
 Theory and Simulation of materials (THEOS)
 Supervision of Prof. Nicola Marzari

During my PhD, I addressed both aspects of the newly born *quantum technologies*, namely hardware and software. From the hardware point of view, I used state-of-the art techniques to predict the optical properties of qubits. On the software side, I designed efficient quantum algorithms for the calculation of the Green's functions on a current quantum computer.

MSc in Mechanical Engineering

9/2015 - 12/2017

Politecnico di Torino, Turin, Italy
 Final GPA: 30.0/30
 Final grade: 110/110 cum laude

Thesis: "Thermal conductivity in graphene and carbon nanotubes: the Relaxons picture".
 Carried out at EPFL.

BSc in Mechanical Engineering

9/2012 - 7/2015

Università Politecnica delle Marche, Ancona, Italy
 Final GPA: 29.7
 Final grade: 110/110 cum laude

Thesis: "Design of a marine propeller aided by CFD and structural analysis".

Awards

Winner of the EPFLInnovators fellowship.

2018

EPFL, Lausanne

The EPFLInnovators program is aimed at developing the innovation potential and the complementary business skills of selected PhD candidates.

Winner of *Maker-Competitions@Polito*

2016

Turin, Italy

The internal team competition in Politecnico di Torino consisted in designing and building an efficient desalinator with a very limited budget.

Experiences

Secondment, IBM Research

4/2021 - 12/2021

Zurich, Switzerland

On the research of new quantum algorithms for the solution of quantum chemistry problems on the current superconducting processors.

Organizer of the 1st edition of QCHS

6/2021

EPFL, Lausanne, Switzerland

With more than 600 applications, the Quantum Computing Hard- and Software Summer School was a successful event meant to teach the principles of quantum computing to a broad plethora of scientists.

Innosuisse Business Concept certificate

9/2021 - 12/2021

EPFL, Lausanne, Switzerland

The Innosuisse Business Concept training provides the practical tools and knowledge to transform ideas into strong business projects and eventually run a startup.

Publications

Photoluminescence and optical properties

- Libbi, F. & Melo, P. & Zanolli, Z. & Verstraete, M. J. & Marzari, N. "Phonon-assisted luminescence in defect centers from many-body perturbation theory", *Phys. Rev. Lett.* **128**, 167401 (2022).

Quantum computing

- Libbi, F. & Rizzo, J. & Tacchino, F. & Tavernelli, I. & Marzari, N. (2020). "Effective calculation of the Green's function in the time domain on near-term quantum processors". *arXiv:2203.12372* (2022).
- Rizzo, J. & Libbi, F. & Tacchino, & Ollitrault, P. & F. & Tavernelli, I. & Marzari, N. (2020). "One-particle Green's functions from the quantum equation of motion algorithm". *arXiv:2201.01826* (2022).

Thermal transport

- Libbi, F. & Bonini, N. & Marzari N. (2020). "Thermomechanical properties of honeycomb lattices from internal-coordinates potentials: the case of graphene and hexagonal boron nitride", *2D Mater.* **8** 015026 (2020).

Refereing

- Nanoletters.
- SciPost.